THESE

Laboratoire D'Optique Atmosphérique

En vue de l'obtention du grade de

DOCTEUR DE L'UNIVERSITE DE LILLE

*Ecole Doctorale des Sciences de la Matière, du Rayonnement
et de l'Environnement*

Discipline

Science de la Terre et de l'Univers, espace Terre, Enveloppes Fluides

Par

PERLA ALALAM

ÉTUDE DES AÉROSOLS À PARTIR DE MESURES EN LABORATOIRE ET IASI: APPLICATION AUX DÉSERTS D'ASIE DE L'EST

AEROSOL STUDY USING LABORATORY AND IASI MEASUREMENTS: APPLICATION TO EAST ASIAN DESERTS

Soutenance complétée, le 8 Décembre 2022 à 14:00

Président du Jury	**D. Petitprez**	Professeur	PC2A, Université de Lille
Rapporteur	**P. Coheur**	Professeur	Université libre de Bruxelles, Belgique
Rapportrice	**S. Vandenbussche**	Directrice de Recherche	Institut Royal d'Aéronomie Spatiale de Belgique
Examinateur	**O. Dubovik**	Directeur de Recherche	LOA, Université de Lille
Examinatrice	**V. Capelle**	Ingénieure de Recherche	ARA, Ecole Polytechnique, Palaiseau
Examinateur	**P. Sellitto**	Maître de Conférences	LISA, Institut Pierre Simon Laplace
Invité	**A. Al Choueiry**	Professeur	Université Libanaise, Beirut, Liban
Directeur	**H. Herbin**	Professeur	Université de Lille

TABLE OF CONTENT

TABLE OF FIGURES

7

TABLE OF TABLES

ACKNOWLEDGEMENT

ACRONYMS

AERONET: AErosol RObotic NETwork

AOD: Aerosol Optical Depth

APS: Aerodynamic Particle Sizer

BGA: Bruggeman's Approximation

CALIOP: Cloud-Aerosol Lidar with Orthogonal Polarization

CALIPSO: Cloud Aerosol Lidar and Infrared Pathfinder Satellite Observations

CCD: Charge-Coupled Device

CDE: Continuous Distribution of Ellipsoid

CPC: Condensation Particle Counter

CRI: Complex Refractive Index

EUMETSAT: EUropean organization for the Exploitation of METeorological SATellites

ERBE: Earth Radiation Budget Satellite

FTIR: Fourier Transform InfraRed

HITRAN: High-resolution TRANsmission molecular absorption database

IASI: Infrared Atmospheric Sounder Interferometer

IR: InfraRed

LBL: Line-By-Line

LC: Linear Combination

LIDAR: Light Detection and Ranging

LOA: Laboratoire d'Optique Atmosphérique

LSE: Land Surface Emissivity

MODIS: MODerate resolution Imaging Spectroradiometer

MetOp: Meteorological Operational

NOAA: National Oceanic and Atmospheric Administration

OEM: Optimal Estimation Method

PCA: Principal Component Analysis

PC2A: PhysicoChimie des Processus de Combustion et de l'Atmosphère

RMS: Root Mean Square

RTE: Radiative Transfer Equation

SD: Size Distribution

SEVIRI: Spinning Enhanced Visible and InfraRed Imager

SEM: Scanning Electron Microscopy

SMPS: Scanning Mobility Particle Sizer

TEM: Transmission Electronic Microscopy

UV: UltraViolet

VMA: Volume Mixing Approximation

VMR: Volume Mixing Ratio

XRD: X-Ray Diffraction

INTRODUCTION

Atmospheric science has recently developed into a major field of study with far-reaching scientific and social attention. Topics such as atmospheric composition were not deemed sufficiently until the last 35 years and now represent major branches of the discipline. Aerosols are solid or liquid particles emitted and transported at different layers in the atmosphere, having interactions with gaseous molecules, solid particles and liquid droplets. They can originate from natural sources i.e., deserts and volcanos and even oceans, or from human sources mainly related to industrial activities. They play an important role in the radiative balance of the Earth, as they have the ability to absorb and scatter solar and terrestrial (or thermal infrared) radiation.

Particularly, mineral dust presents one of the most abundant Particulate Matter (PM) originating from natural sources in the atmosphere *(Washington and Todd, 2005)*, since it is the product of wind erosion of the land surface in arid and semi-arid regions *(Duniway et al., 2019)*. Due to its essential impact on the climate system, more attention has been attributed to mineral dust, which plays a fundamental role in air quality *(Querol et al., 2019a)*. Moreover, climate change and desertification amplify global dust emissions in the atmosphere *(Safriel, 2007)*. Dust can directly perturb the radiative flux by interacting with solar and thermal radiation through absorption and scattering processes *(Bi et al., 2017)*. It can also indirectly affect clouds, ice formation, and nucleation *(Kanji et al., 2019)*. Climate alteration depends on the physico-chemical properties of atmospheric dust since the forcing effect is associated with dust mineralogical composition *(Michel et al., 2003)*.

Satellite remote sensing instruments present a promising tool to observe Earth's atmosphere and are characterized by reliable observations. However, many challenges cause constraints to measure and quantify aerosol properties from space, including the lack of optical properties and the surface emissivity signal effect on satellite observations. For instance, East Asia can produce up to 800 Tg y^{-1} of mineral dust *(An et al., 2018)*, which is uplifted near the surface in the troposphere above the continent *(Chen et al., 2017)*,

where the Land Surface Emissivity (LSE) has spectral variability that affects remote sensing detection *(Masiello et al., 2014)*. This presents a primary error source on the aerosol quantification, as it impacts clear sky and dust layer observation above the land *(Ackerman, 1997)*. Another particularity of this region, is the diversity in its mineralogical composition; the dust is rich in silicates and carbonates, and depends on dust sources *(Young Jeong, 2020)*.

In this work, we will use the Infrared Atmospheric Sounding Interferometer (IASI), a high spectral resolution instrument having different advantages in the infrared: continuous spectrum, low radiometric noise, global coverage above lands/oceans, and day/night observations. We apply our work on East Asian dust storms in order to attain the following objectives:

1- Cross the LSE challenge typically faced above lands in this region and correct available LSE datasets from literature to optimize the IASI observations.
2- Use new aerosol optical properties from East Asia measured in the laboratory to establish the link with the chemical properties.
3- Investigate the capability of IASI observations, with the complexity of dust mineralogy in this region, to provide the mineral dust composition using these new optical properties found in the laboratory.

We introduce in **Chapter I** the different notions used in this work: the microphysical, chemical, and optical properties of mineral dust, remote sensing detections, and the East Asian deserts. In **Chapter II**, the IASI instrument is presented. We also discuss the false IASI dust observation caused by the LSE and the impact related to the use of a mean monthly emissivity atlas that can over represent or under represent the IASI radiances. Then, we introduce a new LSE correction method to improve the LSE dataset; a new diagram scheme is illustrated with the correction equations. Next, we determine an equivalent optical thickness spectrum derived from IASI radiances, and we use it to compare spectra before and after the LSE method. In **Chapter III**, we present new experimental optical properties (i.e., the extinction coefficient spectra) measured using Thermal Infrared (TIR) data for Gobi dust and pure minerals (quartz, illite, and calcite). An effective extinction coefficient is simulated using a linear combination of the pure mineral extinctions spectra to reproduce the Gobi dust spectrum and IASI dust observation. Then,

laboratory measurements are compared to the IASI optical thickness, showing the same molecular features. Finally, we couple the IASI optical thickness with a linear combination of pure mineral spectra to compute the mineralogical dust mass weights. We apply the method to a dust storm that occurred between 3–7 May, 2017, using IASI observations based on METOP-A. Finally, we summarize the work by comparing the results with METOP B and a second dust event between 14–22 March 2021. Lastly, we use the same optical properties in a new radiative transfer algorithm (ARAHMIS) developed at the Laboratoire d'Optique Atmosphérique to simulate the forward model of IASI spectra to be used in future work to retrieve the micro-physical properties.

CHAPTER I. ATMOSPHERIC MINERAL DUST

This chapter introduces the context of the thesis by defining the climate system and the atmospheric constituents: gases, aerosols, and hydrometeors. Then, the mineral dust cycle and its impact on the Earth's atmosphere and ecosystems are discussed. Next, aerosol's physical and chemical properties are defined with a complete description of various parameters, i.e., the size distribution and the chemical composition. The aerosol-radiation interaction is also presented by the dust optical parameters (e.g., refractive index, extinction coefficient), giving information about the aerosol physico-chemical properties. The chapter also includes a definition of remote sensing detection that uses electromagnetic radiation to provide dust information. Furthermore, the main description of active and passive, in-situ, ground-based, and satellite instruments is given. Finally, the geography of deserts in East Asia is designated, and the challenges faced in this region are explained.

1.1 ATMOSPHERIC STRUCTURE AND COMPONENTS

The Earth's climate system compromises several components including the atmosphere, surfaces, and marine and terrestrial ecosystems. One of its most critical components is the atmosphere, as it can have an important impact on the climate. The atmosphere is a gaseous envelope that surrounds the Earth and is held by its gravity. Pressure and air density decrease exponentially with height, while the temperature varies linearly with height, inducing stratification into layers (**Figure 1**).

One can distinguish several atmospheric layers; the *troposphere* extends from the surface, and the temperature decreases with the altitude to the layer top limit. Earth's surface radiation influences the lower limit termed the *boundary layer* can extend from 0 to 2 km, in which dust entrainment happens. The top limit is called *the tropopause,* whose altitude depends on the latitude and weather conditions between 8 and 18 km. Air masses are mostly condensed in this layer, where most weathering occurs i.e. cold and warm winds, these airmasses don't mix together, they create a boundary called *front* resulting natural dust emissions, mixing with emissions caused by human activities. The *stratosphere* extends from the tropopause to an altitude of about 50 km. It plays a protective role for living organisms from harmful ultraviolet solar radiation, as it contains ozone (O_3) in large quantities. The *mesosphere* spreads from the stratopause up to 80 to 90 km altitude. It protects the Earth from meteorites as high heat collisions with gases evaporate from them having a minimal temperature layer. The *thermosphere* beyond 90 km has highly energetic radiation from the sun that can dissociate the air molecules and ionizes atoms *(Schlatter, 2010)*. The solar wind interacts with the Earth's geomagnetic field creating the *magnetosphere*. The latter, stores the solar wind energy and dissipates it in geomagnetic storms that accelerate ions which drive large electrical currents diverted down into the *ionosphere*.

The atmosphere is formed by 99% of dry air that includes molecular nitrogen (N_2) and oxygen (O_2), and trace gases, in addition to water vapor (H_2O). Greenhouse gases absorb infrared radiation and re-emit energy in all directions. When the temperature of emitted radiation towards the Earth's surface is higher than the temperature of radiation emitted towards the space, the *greenhouse effect* occurs warming Earth's atmosphere. The intensity of this effect depends on the gases' concentration, their absorption capacity

and their resistance time in the atmosphere. The most absorbent element is water vapor, followed carbon dioxide (CO_2), methane (CH_4), ozone (O_3), nitrous oxide (N_2O), and hydrofluorocarbons (gases consisting of fluorine, chlorine, or bromine), such as chlorofluorocarbons (CFCs) and hydrofluorocarbons (HCFCs), which have a destructive effect on the ozone layer. In addition, reactive gases, including volatile organic compounds VOC, nitrogen (NO_x, NH_3), and sulfur (SO_2 and H_2S) components can be present in the atmosphere.
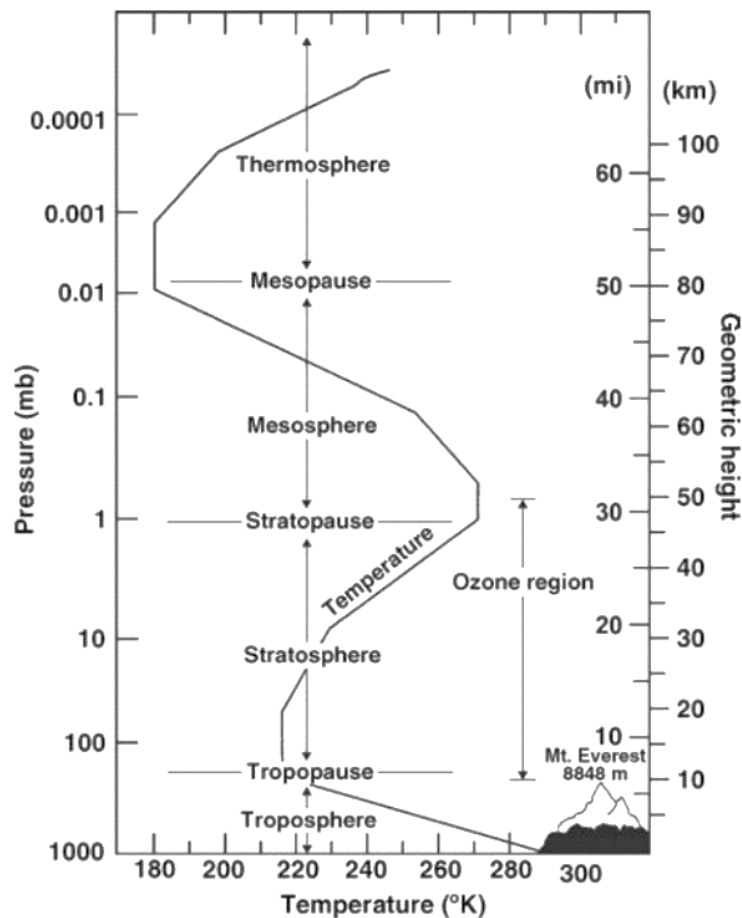
Figure 1 Vertical temperature structure of the atmosphere extending from the surface of the Earth to approximately 110-km altitude as given in the US Standard Atmosphere (1976). The principal layers defined by this temperature structure and the interfaces between them are labeled. As indicated, ozone is found principally in the stratosphere. Two vertical coordinates are given: pressure on the left in millibars (1 mb = 100 Pascal) and geometric altitude on the right (km) *(Schlatter, 2010)*.

The atmosphere is also composed of suspended liquid or solid matter: aerosols and hydrometeors. The term 'aerosols' refers to suspensions of liquid, solid, or mixed particles with highly variable chemical composition and size distribution *(Putaud et al., 2010)*.

Hydrometeors are considered a separate field from aerosols, forming solid or liquid particles composed mostly of water. In parallel to gases, aerosols (e.g., mineral dust, sulphate, nitrate, organic carbon) and hydrometeors mainly scatter solar radiation and have a cooling effect on the climate system, while strongly absorbing aerosols (e.g., black carbon) have a warming effect described by the *parasol effect*. The Radiative Forcing (RF) is the scientific terminology adopted by the IPCC to describe the influence of atmospheric components that block infrared radiation in Earth's radiation budge. Emitted components from 1750 to 2011 are shown in **Figure 2**. The overall RF is positive for gases, while aerosols and clouds have a negative RF. Nevertheless, the uncertainty bar for aerosols RF estimation is large with respect to the estimated itself. This uncertainty comes from the lack of knowledge of the aerosols' microphysical properties and especially chemical properties.
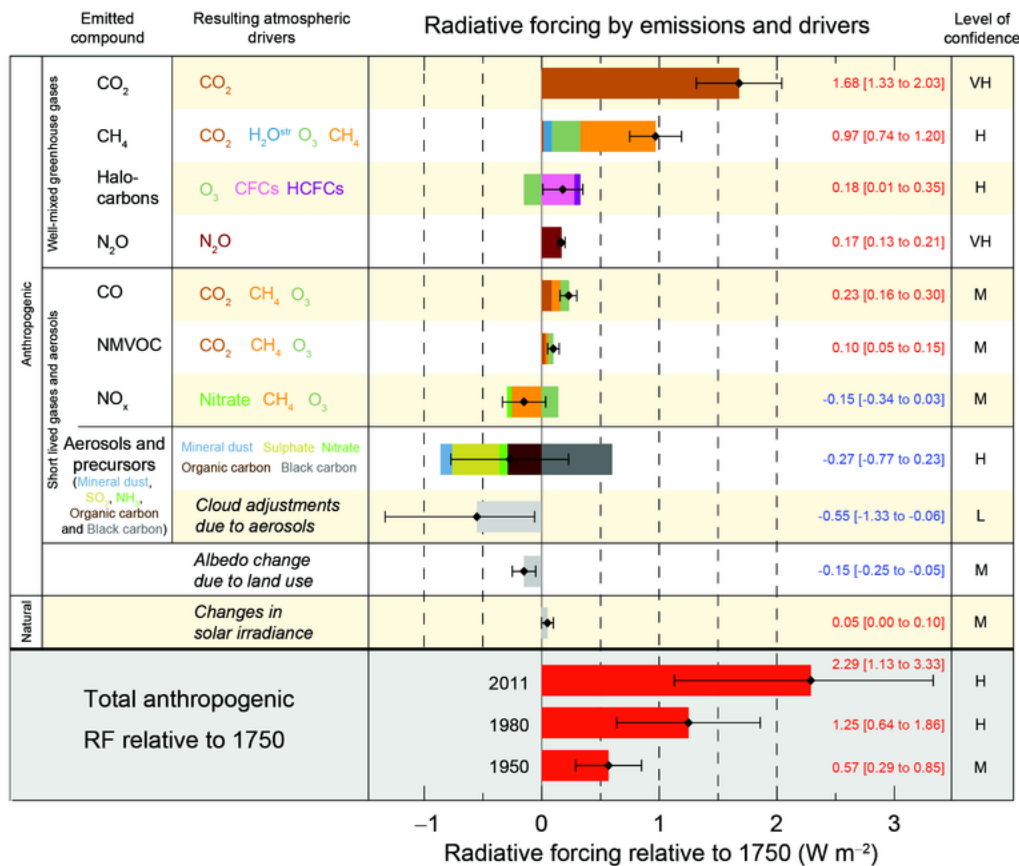
Figure 2 The radiative forcing estimates from 1750 to 2011, and aggregated uncertainties (horizontal bars) for the main drivers of climate change (*https://www.ipcc.ch*).

Therefore, we are particularly interested in atmospheric aerosols. They are variable in space and time depending on the emission source and type. We can distinguish aerosols entrained from natural sources (volcanic ash, sea salt, and mineral dust from deserts) and anthropogenic aerosols (industrial dust, soot, and organic carbon). Mineral dust is the most abundant in mass by emitted natural particulate matter in the atmosphere (1000–3000 Tg per Year) *(Boucher, 2015)*. Mineral dust is the product of wind erosion of the soil composed of different minerals in arid and semi-arid regions. It undergoes a specific cycle (emission, transportation, and deposition), significantly impacting the climate system and air quality *(Querol et al., 2019b)*. Moreover, climate change and desertification amplify the global dust emission in the atmosphere *(Safriel, 2007)*. Therefore, special attention must be attributed to mineral dust physico-chemical properties to better understand their impact on the atmosphere, climate and ecosystem.

In this work, we focus on atmospheric mineral dust, for which, in the next section, we will describe the process of the dust cycle, detail its impact, and define its microphysical and chemical properties.

1.2 DUST CYCLE AND IMPACT

The mineral dust cycle has three main elements: emission, transport, and deposition (**Figure 3**). First, mineral dust is entrained in the atmosphere from the ground surface, and this process is controlled by wind speed, the nature of the soil, and surface obstacles faced during the formation process. The threshold required to entrain dust depends on the particle size distribution, the sorting characteristics of the particle, the surface cohesion, and the surface roughness. Dust storms are common events in arid and semi-arid regions including deserts. The latter are characterized by a low vegetation cover, frequent repetition of soil, and atmospheric droughts (i.e., low humidity and high wind velocity).

Once emitted in the atmosphere, dust is transported by turbulent flow structures of the air carrying the particles without contact with the surface. Aerosol lifetime varies from a few days in the lower troposphere up to several months in the stratosphere, depending on mineral dust size distribution and level (**Figure 4**). The transport direction depends on the direction and intensity of the wind fronts. Mineral dust can be

transported in the atmosphere at long distances for many days. For instance, in April 2001, the 'Perfect Dust Storm' event was blown by the Siberian winds from North-West China and traveled across the Pacific Ocean to the North Atlantic Ocean (**Figure 5**). The dust cloud reduced visibility while passing through the cities and mixed with pollutant particles in the air, i.e., carbon monoxide. These pollutants were then deposited as they cross the ocean. The global radiation budget and hydrological cycle are generally susceptible to long-range transport and aging processes that can impact the dust's physical properties by altering the particle's morphology, size, and scattering properties. Airborne mineral dust can have a direct impact on the radiative budget through absorption and scattering processes. This impact strongly depends on the mineral dust properties, which dictate the fractions of light dust absorbs or reflects as a function of wavelength. On the other hand, it can have an indirect impact on the radiative balance by interacting with clouds through nucleation. For example, calcium carbonate ($CaCO_3$) can interact with HNO_3 in the presence of water, leading to calcium nitrate droplets that can cause severe human health risks (**Figure 6**).
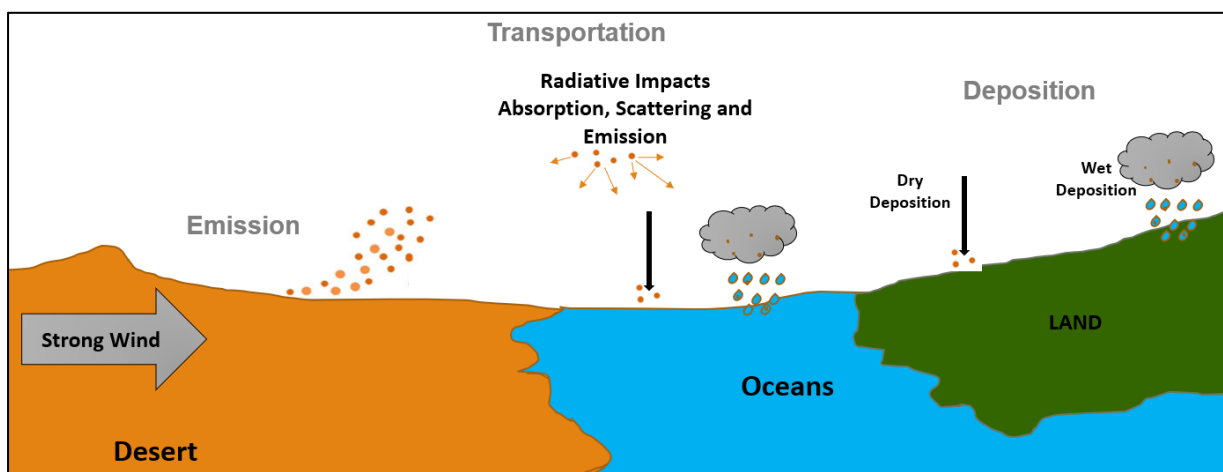
Figure 3 Desert dust cycle: emission, transport and deposition.
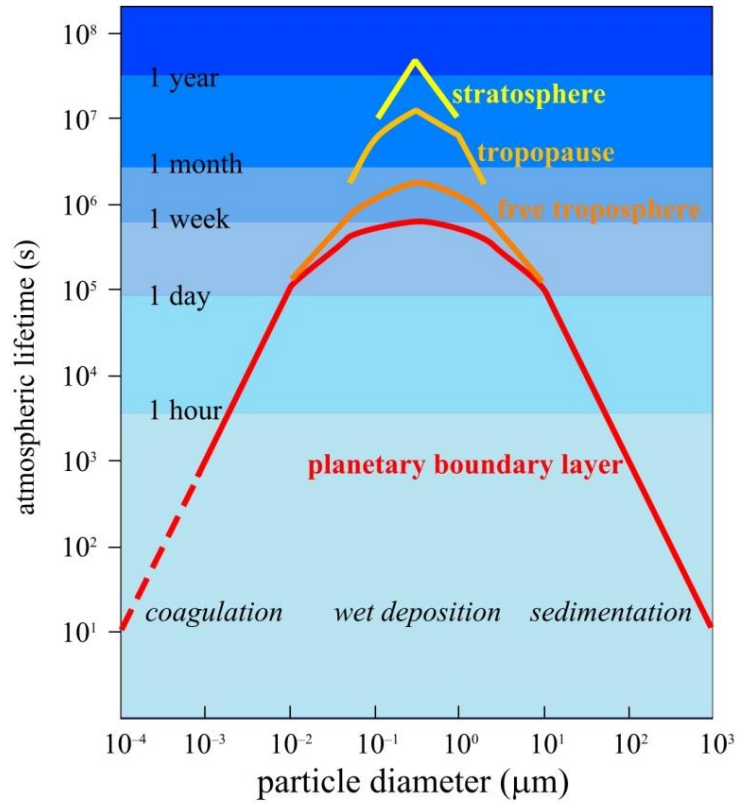
Figure 4 Atmospheric lifetimes of different size particles at different levels of the Atmosphere *(Jaenicke, 1980)*.
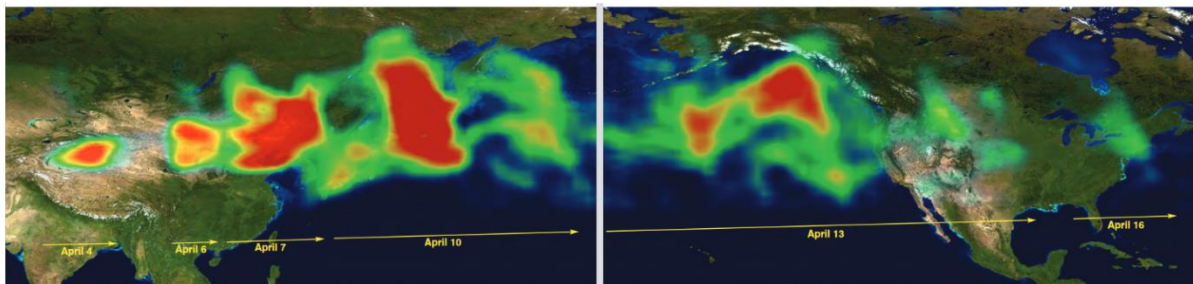
Figure 5 TOMS detection shows transported mineral dust from China to the North Atlantic Ocean 2001 *(https://nasa.gov)*.
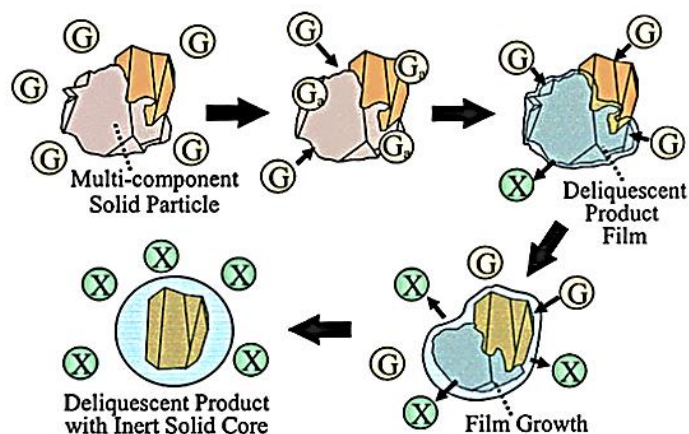
Figure 6 Pictorial representation of changes in a composite mineral dust particle as it is processed in the atmosphere *(Usher et al., 2003)*.

Finally, dust can be deposited by dry deposition through the gravitational settling and impaction of the Earth's surface by turbulence on the Earth's surface or by wet deposition, i.e., scavenging through precipitation in the water or ice phase. When deposited, dust plays an important role in trace element biogeochemistry and ocean productivity. Iron, phosphorus, and nitrogen are the nutrients that control the functionality of marine and terrestrial ecosystems. They are considered an essential fertilizers source for fauna and flora. In addition, depending on dust load concentration in the atmosphere, nitrate particles can interact with calcite particles to form calcium nitrate, a source of nitrogen when finally deposited *(Fan et al., 2004)*. **Figure 7** shows the average dust flux deposition per year.
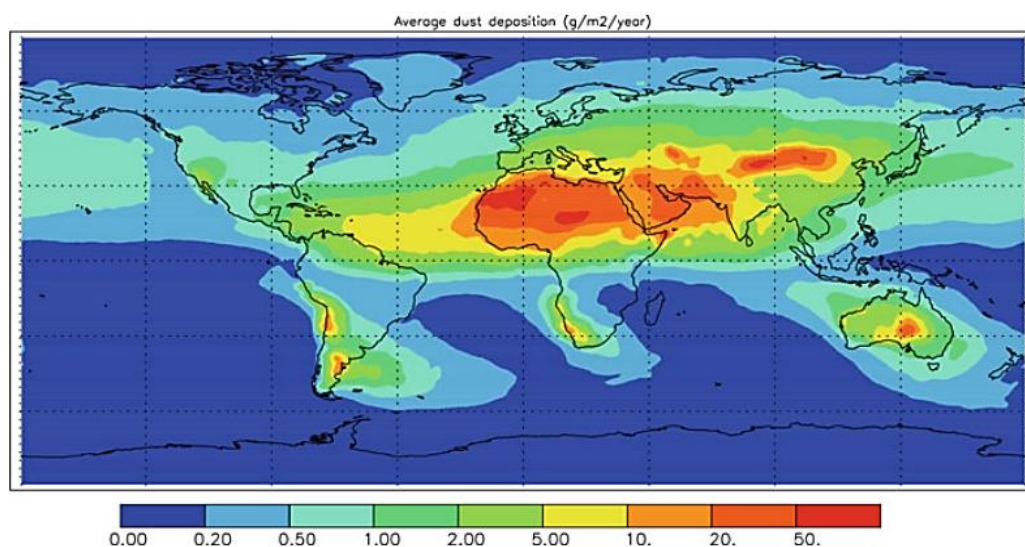
Figure 7 Global annual average of dust deposition flux in g/m^2/year *(Jickells et al., 2005)*.

Finally, the mineral dust cycle affects on regional or global scales the continental and marine ecosystems, the Earth's climate and air quality, human health and activity, fauna, and flora. Therefore, it is important to understand the dust's physical and chemical properties, which we introduce in the next section.

1.3 MICROPHYSICAL AND CHEMICAL PROPERTIES

The aerosols' properties are extremely variable in space and time due to the heterogeneity in aerosol sources and their relatively short residence time in the atmosphere. Hence, one is usually interested in characterizing a population of aerosols rather than individual particles *(Boucher, 2015)*. The most important characteristics of an aerosol population are the size distribution, number of concentrations, and chemical composition.

1.3.1 Size Distribution

The size distribution (SD) is an important parameter in understanding the different impacts of mineral dust. The aerosol size affects the particle entrainment, suspension, changes with the aging processes and therefore impacts the radiative budget. In this section, we define the particle size distribution equations. Then, we classify the SD based on the aeolian processes by describing the particle mode based on their SD. Finally, we mention some possible techniques for measuring the SD.

An aerosol population is characterized by its SD. Experimental observations show that the aerosol size is fairly distributed, according to a lognormal function (**Figure 8**) *(Limpert et al., 2001)*. The distribution can be in volume, surface, or number size distribution.
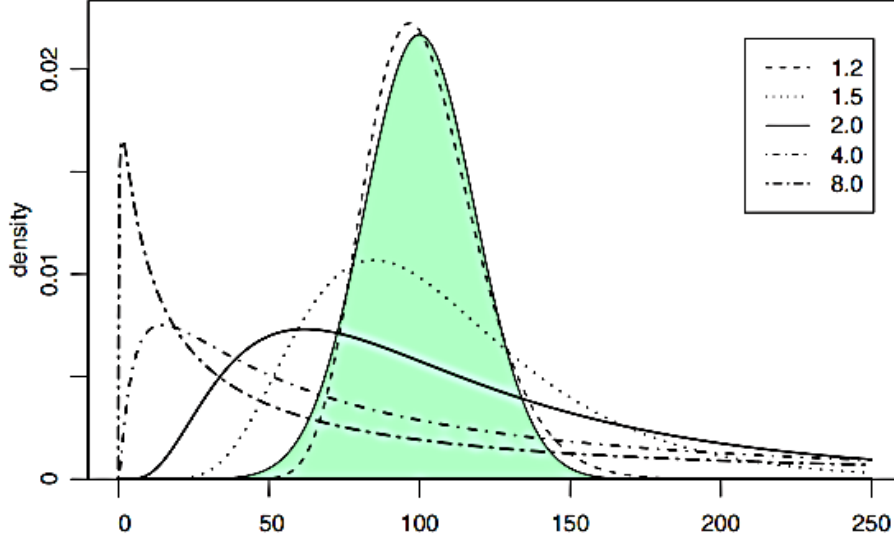
Figure 8 Density functions of selected log-normal distributions compared with a normal distribution. Log-normal distributions $n\ (r_g, \sigma_g)$ as function of the number of particles are shown for five values of multiplicative standard deviation σ_g *(Limpert et al., 2001).*

The function describes the number of aerosols per unit volume $n(r)$ between the radii r and $r + dr$ and it is given by:

$$n(r) = \frac{N_0}{r ln \sigma_g \sqrt{2\pi}} e^{-\frac{1}{2}\left(\frac{ln(r/r_g)}{2 ln^2 \sigma_g}\right)} \ \textbf{(1)}$$

where N_0 is the total number of concentration aerosols (in particles.m^{-3}), r_g the mean geometric radius, σ_g the geometric standard deviation and $ln\sigma_g$ is the dimensionless standard deviation of $ln(r/r_g)$.

The entrainment of mineral dust depends on the particle size distribution. In aeolian transport, we can identify three types of soils each depending on the particle size: clay, silt and sand *(Shao et al., 2011). Clays* are particles with diameter between 0.01 and 2 μm and follow the suspension process by the wind, they can be transported at long distances in the atmosphere before deposition. Particles with diameter less than 0.01 μm is limited by the adhesive and cohesive forces which tend to form larger particles or aggregates. *Silt* particles have a diameter between 2 and 60 μm and undergo the saltation process where particles are ejected from the surface for relatively small time before being deposited back to the surface. This process is considered as a prior condition for the initiation of

dust storms. *Sand* particles have a diameter between 60 and 2000 µm, move very slowly in a soil mass following the creep process. Clay and silt are considered dust-like particles and particularly atmospheric dust presents particles with less than 10 µm.

Aerosols can be classified based on their mode: the radius ensemble for which $n(r)$ presents a maximum *(Boucher, 2015)*. We can distinguish the *nucleation mode* (particles < 20 nm), the fine *mode* (for clay particles) and the *coarse mode* (for silt particles). Fine mode dominates the aerosol number distribution, while the coarse mode dominates the aerosol volume distribution. **Figure 9** summarizes soil types based on aeolian processes and modes associated with the SD.
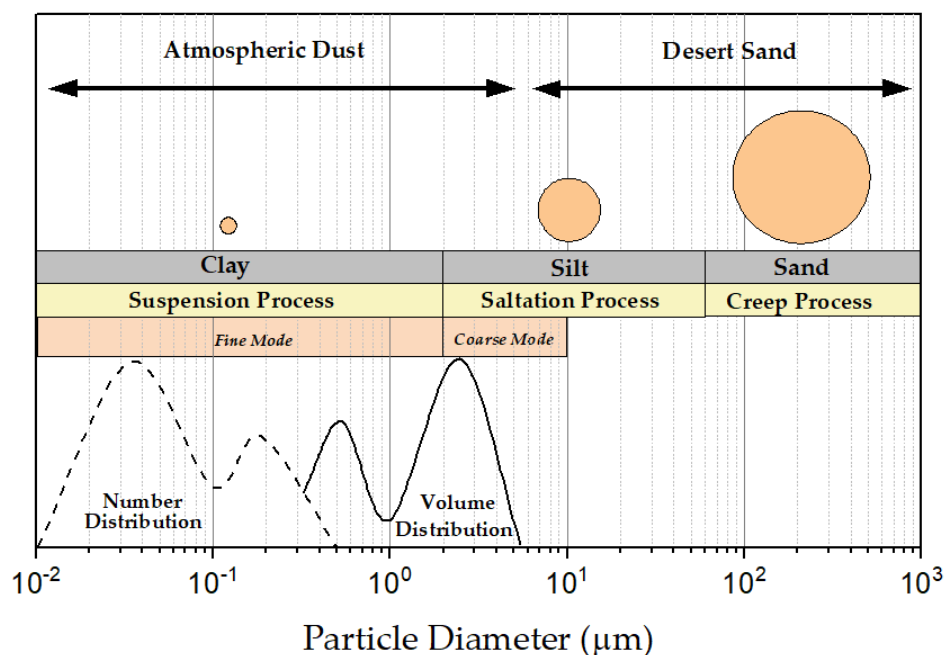
Figure 9 Schematic of different soil types clay, silt and sand, their size distribution and their aeolian processes.

Different techniques are used to determine the SD and the concentration of aerosols. For instance, the Scanning Mobility Particle Sizer (SMPS) measures the SD of aerosols whose electrical mobility diameter determines their size with a Differential Mobility Analyzer (DMA) and counting particles using a Condensation Particle Counter (CPC). Another example is the aerodynamic particle sizer (APS) that measures the *aerodynamic particle diamete*r based on particle time of flight and the *optical diameter* based on scattered light intensity. Typically, both methods are used simultaneously to give a total SD

for aerosol fine mode *(Möhler et al., 2008)*. In this study, experimental dust measurements were performed with SMPS and APS: the first counts the particle diameters between 20 nm-600 nm and the second counts the particle diameters between 500 nm-20 μm *(Deschutter, 2022)*. Furthermore, Scanning Electron Microscopy (SEM) can estimate the particles' diameter and mineral composition *(Falkovich et al., 2001)*. However, the result of this method represents the SD based on a portion of the sample of hundreds of individual particles. In contrast, the first two methods typically measure about thousands of particles.

1.3.2 Chemical Composition

Aerosol chemical composition is key element in understanding aerosol processes and their impact on the atmosphere. The radiative forcing is highly associated with dust mineralogical composition changes in the atmosphere *(Michel et al., 2003)*. In this section, we will elaborate on the mineralogical composition of mineral dust and its mixture state. Moreover, we will describe the vibrational modes in the infrared (IR) that can be used to characterize the composition of dust samples using different techniques.

Mineralogical Composition

Mineral dust is composed of minerals, especially silicates and carbonates, in crystalline or amorphous form. One of the major mineral families is the phyllosilicates group (e.g., illite, kaolinite, and smectite) which are abundant in dust samples *(Journet et al., 2014)*. Members of the tectosilicates group, i.e., quartz and feldspars, form 75% of the Earth's crust and are found in different desert dust samples from the globe as shown in **Figure 10**. The carbonates family contains calcite and dolomite, considered tracers of Saharan and East Asian dust *(Formenti et al., 2011)*. These minerals are detectable in the thermal infrared, where different vibrational modes are present.
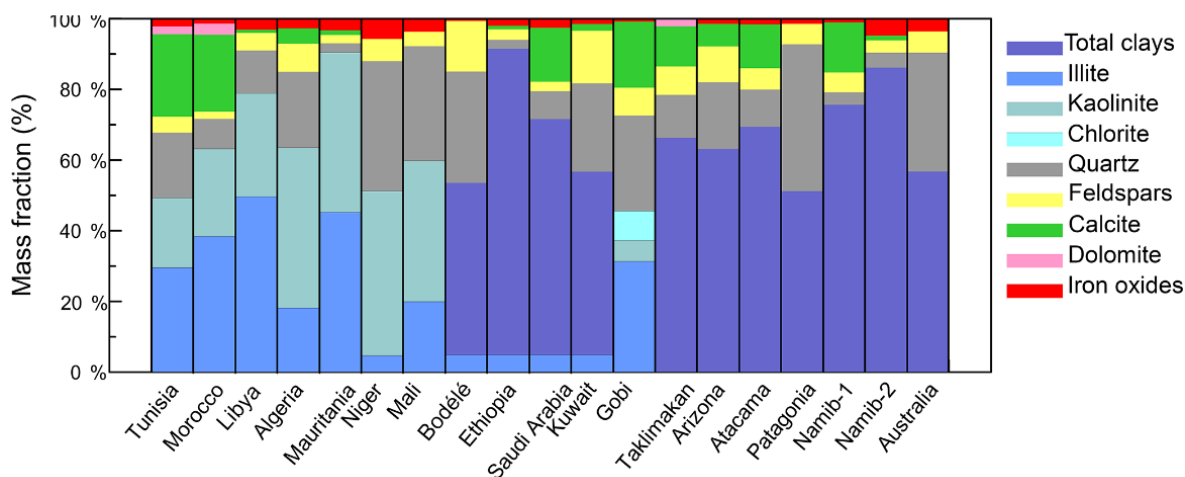
Figure 10 Mineralogy of 19 different aerosol samples from the world *(Di Biagio et al., 2017)*.

The vibrational frequencies of a mineral molecule are correlated with the atoms' bond environment and strength: the stronger the bond, the higher the energy required to stretch. For example, quartz molecules have a structure wherein all of the four oxygens of SiO_4^{4-} tetrahedra are shared with other tetrahedra. Si - O bonds are strong covalent bonds, interlocking the structure as shown in **Figure 11**. The tectosilicate minerals family tends to have a high hardness. On the other hand, for illite, members of the phyllosilicate's family O^{2-} and OH^- group anions are present. The main cations substitutions of Si are Mg^{2+}, Al^{3+}, Fe^{2+}, and Fe^{3+} forming infinite sheets from which the name *sheet silicates (Fang et al., 2018)*.

Tectosilicates   **Phyllosilicates**
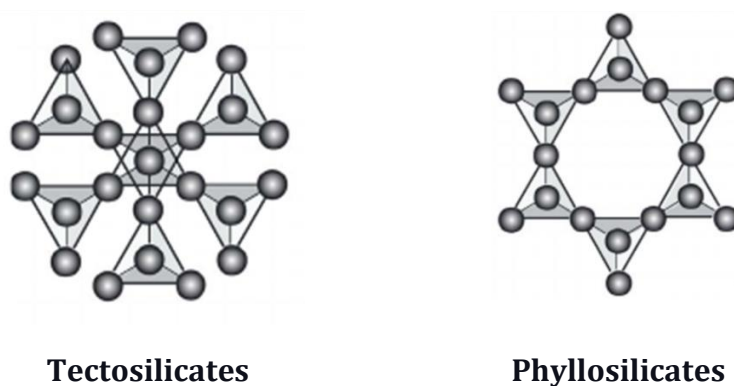
Figure 11 Crystal structure of tectosilicates and phyllosilicates *(Fang et al., 2018)*.

Minerals are formed of polyatomic molecules having molecular motion at a given frequency, a function of atomic coordinates called *vibrational modes*. Polyatomic molecules can be visualized from a number of point masses united by springs. If such a system receives energy, it will undertake a complex vibrational movement (stretching, deformation, swinging, wagging, twisting). The fundamental vibrational modes are shown in **Figure 12** with an example of Si-O-Si (quartz) symmetrical stretching mode.
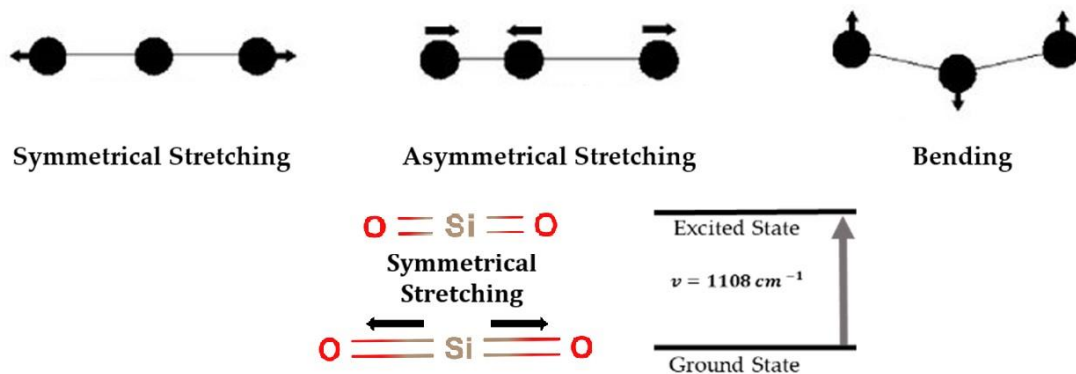
Figure 12 Fundamental vibrational modes with quartz molecular structure in the ground state and excited state at 1108 cm^{-1} having a symmetrical stretching.

Dust composition can be determined either for individual particles or a bulk sample. For individual-particle analysis, the SEM has been used for decades to obtain dust particles' chemical elements, shape, and size distribution. This analysis allows a better understanding of the external and internal mixing of mineral dust. The method was used to exploit the quartz and illite/quartz ratio contents and link them to the particle size distribution *(Shao et al., 2007)*.

A bulk sample is predominately analyzed to obtain the mineralogical composition with X-Ray Diffractometry (XRD). This technique is limited to determining a sample's crystalline compounds while neglecting non-crystalline minerals, which may constitute a significant fraction in some dust samples. XRD was previously used in geochemical tracing methods to link dust mineralogy and sources depending on the geology *(Chen and Li, 2011)*. In East Asia, this analysis showed that the calcite content decreases from West to East, and conversely, the feldspar content increases *(Shen et al., 2009)*.

Vibrational spectroscopy is another method that measures the vibrational energy levels associated with the chemical bonds in certain structural fragments of a dust sample. Fourier Transform InfraRed (FTIR) spectrometry is among the most popular techniques. The measured extinction coefficient spectrum of dust exhibits mineralogical fingerprints showing chemical information *(Di Biagio et al., 2014a)*. In-situ spectrometers are typically employed, while satellite sensors are used to map the Earth's surface soil mineralogy, i.e., the Advanced Spaceborne Thermal Emission and Reflection Radiometer (ASTER) *(Rajendran and Nasir, 2019)*. Until today, the absence of the adequate optical properties (i.e., complex refractive indices) restricts dust parameter retrievals from satellite observations. For example, the quartz optical properties used in dust retrieval date from 1969 *(Peterson et al., 1969)*. As well as the limitations encountered using satellite remote sensing i.e., the land surface signal with its high spectral variability altering the spectral detections.

Mixture State

The knowledge of the mixture types of an aerosol population is important to understand its properties, particularly the chemical interactions involved during the dust cycle.

Aerosols can be grouped based on their mixture state; we typically distinguish between external and internal mixtures. In external mixing, each particle of the population can be differentiated with its proper chemical or mineral composition, e.g., quartz, calcite, and illite. In this type of mixture, we can use different SD for each aerosol type. In internal mixing, each particle of the population can inhomogeneous. In this case, the population is characterized by a single SD.

The two mixtures defined above describe ideal models, and the reality falls in between. Therefore, a real aerosol population is a function of the SD in addition to the mixture type, which can vary in degrees. The different types of aerosol mixtures are represented in **Figure 13**.
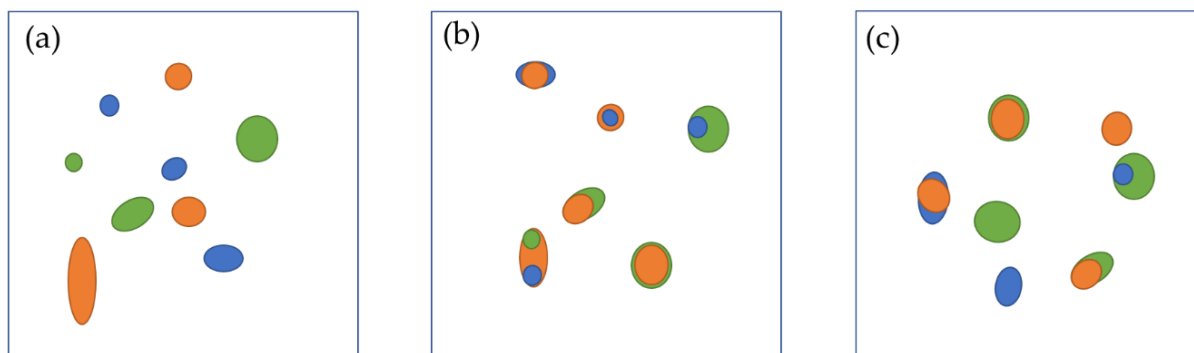
Figure 13 Schematic of mixture state of aerosols. (a) external mixture, (b) perfect internal mixture, (c) realistic mixture.

Electron microscopy techniques can be used to provide information on the mixture state of individual particles i.e., Transmission Electronic Microscopy (TEM) and SEM *(Deboudt et al., 2010),* which are also used to identify the particle shape.

Sokolik and Toon, 1999 based their study on external mixture and used a liner combination method to obtain an effective extinction coefficient. In addition, they modeled the radiative effect by considering internal mixtures using the *Effective Medium Theory*. By its name, the theory allows to obtain an effective dielectric constant or complex refractive indices of aggregate of minerals forming a particle. The most used theories are the *Volume Mixing Approximation* (VMA) and *Bruggeman's Approximation* (BGA).

1.3.3 Particle shape

The shape of mineral dust particles is highly variable. We can find nearly pristine crystals, aggregates/agglomerates, rounded, thin flakes, and even spherical particles. Like the SD, the shape can modify the particle's surface area interacting with the radiation. However, it was previously proved that the shape factor is not directly linked to the SD *(Knippertz and Stuut, 2014)*. An example in **Figure 14** of SEM images shows Saharan dust samples with different shapes.
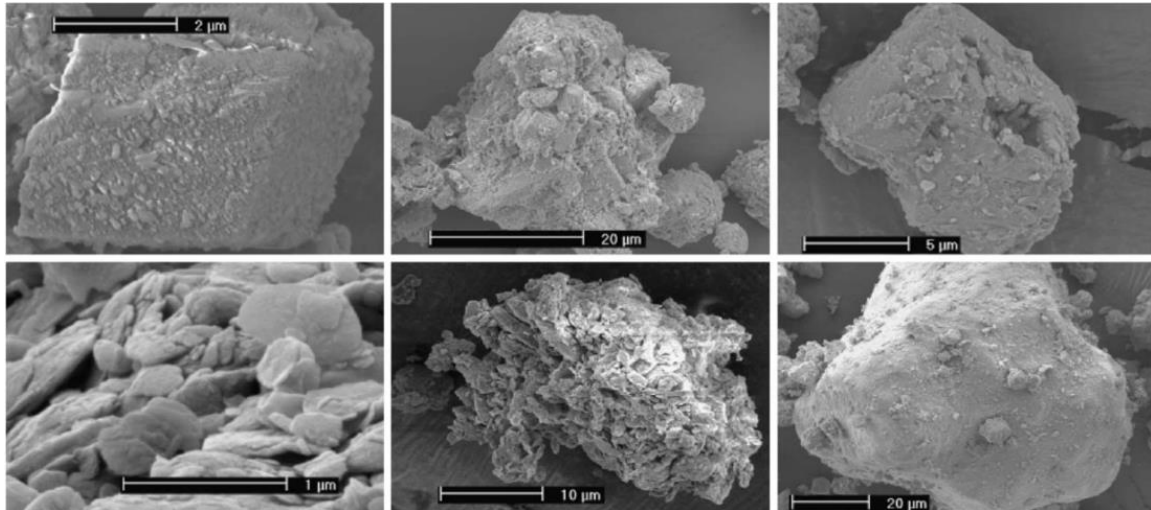
Figure 14 Electron-microscope images of sample mineral dust particles encountered in a soil sample collected in northern Sahara *(Nousiainen, 2009)*.

1.4 OPTICAL PROPERTIES

How the material interacts with radiation is specific for each component, therefore understanding the absorption and emission processes makes it possible to identify these components and quantify their parameters. When measured, the radiation feedback interacting with aerosols through absorption, scattering and emission, defines the optical properties of aerosols. In this section, we will describe the radiation-matter interaction, the measured radiation parameters and the optical constants i.e. the efficiency factor, the extinction coefficient of a single particle then for a layer of particles and the parameters that affect this extinction i.e. the complex refractive indices.

1.4.1 Radiation-Matter Interaction

Particles can interact with solar and terrestrial radiation through absorption and scattering in different directions. The scattering can be elastic: the photon keeps its energy and changes angle with total reflection, with zero transmission and no absorption. On the other hand, scattering can also be inelastic: the photon gives part of its kinetic energy to the vibrational modes of the atom, and changes angle only with partial reflection and refraction, with a non-zero transmission, and no absorption as there is not enough energy for the atom's electron to move to a higher state of energy. In addition, the

process can include absorption and re-emission which depend on the wavenumber of radiation and the properties of the material. First, the photon gives its energy to the atom, and the absorbing electron moves to a higher energy level. Then, the electron will return to its initial state by re-emission of radiation. Particularly, thermal emission reflects the kinetic energy of random movements of atoms and molecules in matter. For example, greenhouse gas emissions contribute through thermal emissions in the temperature forcing and changes in the climate system. **Figure 15** illustrates the different processes of radiation-matter interaction.
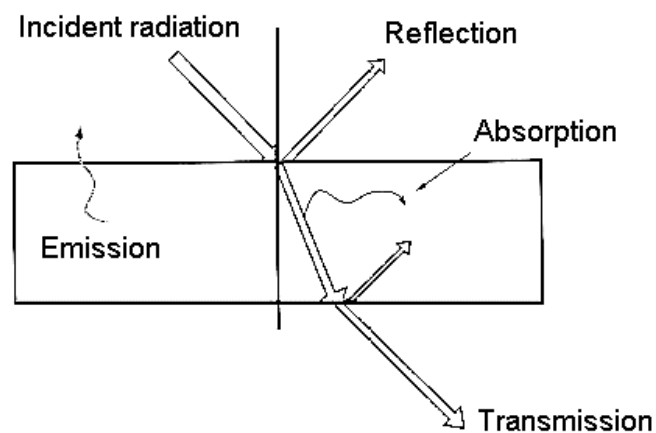
Figure 15 Reflection, transmission absorption and emission of radiation *(Hyll, 2012)*.

1.4.2 Radiative Transfer Equation

The radiation beam that passes through a particle is attenuated by the absorption and scattering processes. These interactions depend on different parameters: the wavenumber of incident radiation beam, the size and shape of the particle, and its natural ability to absorb or scatter energy. **Figure 16** illustrates the aerosol-radiation mechanisms in the case of a spherical homogeneous particle.
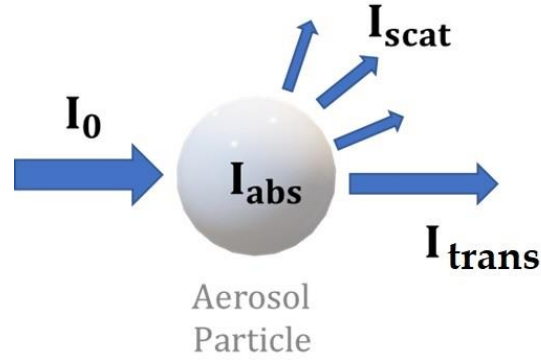
Figure 16 Interaction between a radiation beam with a homogeneous aerosol particle with a spherical shape. I_0: incident intensity, I_{abs}: absorbed intensity, I_{scat}: scattered intensity, I_{trans}: total transmitted intensity.

The extinction irradiance I_{ext} (in W/m²) can be expressed as the sum of scattering and absorption processes, and it is written as follows:

$$I_{ext} = I_{abs} + I_{scat} \quad \textbf{(2)}$$

where I_{abs} and I_{scat} are the irradiances of absorbed and scattered radiation respectively.

In reality, dust is entrained in the atmosphere and transported, forming a layer of particles. When the distance between the particles is larger than the SD of the layer population, we can assume that total scattered intensity is the sum of the scattered intensities of each particle, termed the *single scattering approximation*. The latter can be applied if the population of particles is diluted having the mean free path is much larger than the wavelength. In this case, the multiple scattering in which each particle of the ensemble interacts differently can be neglected. Therefore, we conduct this study on non-opaque observations and assume only single scattering interactions. Nevertheless, it is important to define the optical properties of a layer of the aerosol population in the atmosphere.

Solar and terrestrial radiation interact with aerosol particles and gaseous components that make up Earth's atmosphere by absorption or scattering. The *Radiative Transfer Equation* (RTE) describes the propagation of the radiation in the atmospheric medium taking into account the processes of extinction and thermal emission. It is an equation of

transport of the spectral radiance $R(v)$ (in $W.m^2.sr.(m^{-1})^{-1}$), which expresses the conservation of the radiative energy of an incident radiation in an elementary optical path of thickness ds (**Figure 17**).
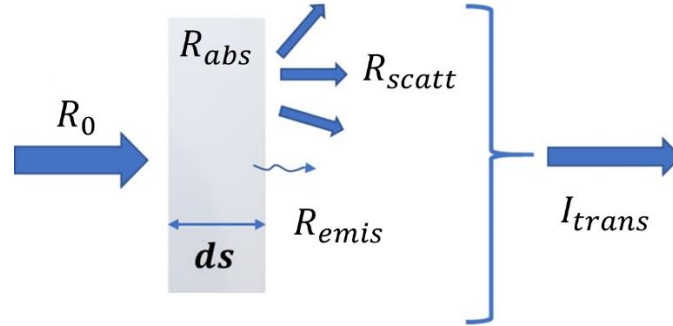
Figure 17 The spectral radiance of a radiation beam passing though an elementary optical path ds. R_0: incident spectral radiance , R_{abs}: absorbed spectral radiance , R_{scat}: scattered spectral radiance , R_{emis}: emission spectral radiance, R_{trans}: total transmitted spectral radiance.

The variation of the spectral radiance along the elementary path ds is written as:

$$dR(v,s) = -R(v,s)\, k_{ext}(v,s)ds + B(v,T)\, k_{ext}(v,s)ds \text{ (3)}$$

The first term of the equation expresses the attenuation of the radiance, which is proportional to the total extinction coefficient k_{ext} constituting the sum of the atmospheric components' extinctions (gases, aerosols and clouds). The second term represents the increase of the radiance due to the thermal emission along the path.

In the case of spherical particles, the extinction coefficient $k_{ext}^{aerosol}(v)$ of a layer of aerosols is described by *Mie Theory* as follows:

$$k_{ext}^{aerosol}(v) = \int \pi r_g{}^2 Q_{ext}(r,v,m)n(r)dr \text{ (4)}$$

with $Q_{ext}(r,v,m)$ is the particle extinction efficiency, m is the complex refractive index, $n(r)$ is the lognormal size distribution.

The efficiency factor expresses the efficiency of the attenuated radiation from a geometric cross-section of a medium. It is expressed as the ratio of the effective cross-section to the

geometric cross-section. For spherical particles of diameter D, having a geometric cross-section of πD^2, the extinction efficiency Q_{ext} can be written as:

$$Q_{ext} = \frac{4\sigma_{ext}}{\pi D^2} \textbf{ (5)}$$

where the *extinction cross-section* σ_{ext} (in m^2) describes the radiation attenuated in all directions by the particle. It can also be written as the sum of the absorption and scattering cross-sections and is calculated by integrating the elementary effective cross-section $\sigma(\theta, \phi)$ over 4π steradians of an elementary solid angle $d\Omega$, and it is given as follows:

$$\sigma_{ext} = \int_{4\pi} \sigma(\theta, \phi) d\Omega \textbf{ (6)}$$

The second term of the **Equation (3)** describes the emitted radiation by the crossed optical path. Due to molecular collisions in the atmosphere, the primary emission comes from thermal emissions. Hence, the atmospheric molecules act like a *blackbody*, a hypothetical body that absorbs all incident radiation on it and reflects none. As a result, the radiation is re-emitted with perfect efficiency, which only varies with temperature variation. It is described by *Planck's Law*: a blackbody radiation $B(v, T)$ (in W. m^2. sr. (m^{-1})$^{-1}$) is defined as the amount of energy emitted by a blackbody as function of its thermodynamic temperature T (in K) and radiation wavenumber v (in cm^{-1}):

$$B(v, T) = \frac{2\, hc^2 v^3}{\left[exp\left(\frac{hcv}{k_B T}\right) - 1 \right]} \textbf{ (7)}$$

The optical properties of the blackbody are independent of the particular material of which the object is made. At a fixed temperature, the radiance versus wavenumber is called *spectral distribution*: how much in each wavenumber interval is emitted by matter. *Wien Displacement law* states that the emission peak decreases with increasing blackbody's temperature (**Figure 18**), it is given by:

$$\lambda = \frac{b}{T} \textbf{ (8)}$$

where $b = 2.897 \times 10^{-3}$ m. K is the constant of proportionality termed *Wien's displacement constant.*

The atmosphere is affected by solar and terrestrial radiation. The sun emits a rela-
tively constant radiation flux towards the Earth with an approximate surface tempera-
ture of 6000 K. The total power emitted is composed of wavelengths varying from low to
high energy. Terrestrial radiation is generated by thermal infrared emission and has a
surface temperature of around 300 K.
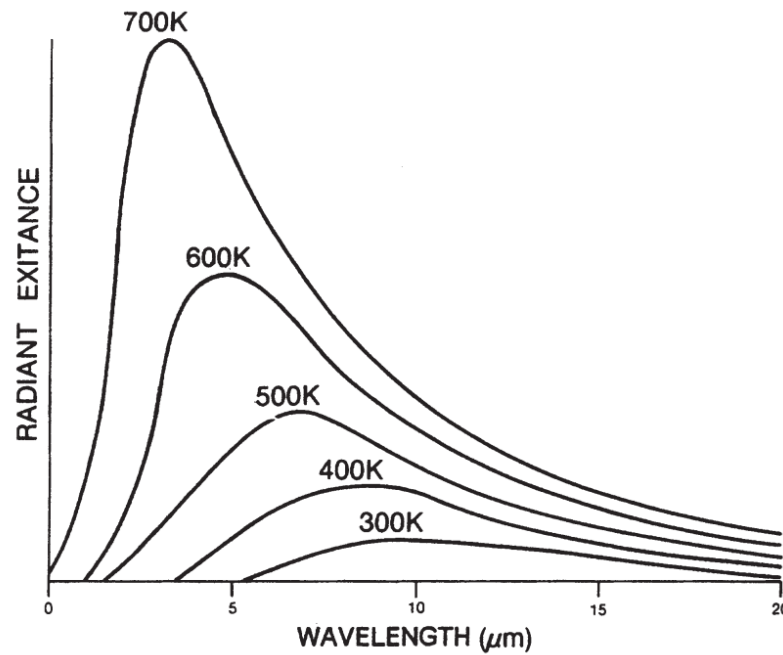
Figure 18 The spectral distribution of a blackbody with temperatres from 300 K to 700 K
(Campbell and Randolph, 2011).

Kirchhoff's Law states that all *Blackbodies* at the same temperature have the same
ratio of emitted radiation to absorbed radiation. Hence, we can define the *spectral emis-
sivity;* a dimensionless parameter that measures the effectiveness of a body as a radiator
with respect to an ideal radiator, and is written as follows:

$$\varepsilon_v = \frac{R(v,T)}{B(v,T)} \textbf{ (9)}$$

For a *blackbody,* the emissivity is 1 since it presents an ideal radiator, while for an ideal
reflector or *white body*, the emissivity is 0. As in nature, there is no ideal radiator or re-
flector, the emissivity lies between 0 and 1, such a body is termed *graybody* e.g., Earth's

surface which has a highly variable emissivity and can pose limitations in aerosol observations.

From **Equation (3)**, we also can define:

$$\tau(v, s) = \int_{s_1}^{s_2} k_{ext}(v, s)ds \ \textbf{(10)}$$

where $\tau(v)$ is the *optical thickness* between s_1 and s_2. It is one of the most used parameters in atmospheric studies since its value contains information about the number of particles and their extinction properties (absorption and scattering) along the path. This parameter does not contain information about emission.

1.4.3 Size parameter

The size parameter x is a unitless parameter that establishes the link between the particle size and the wavenumber of radiation. The effect of the size of a particle on scattering is defined by the size parameter, which is the ratio of its perimeter to the wavelength of the incident light such that:

$$x = \frac{\pi D}{\lambda} \ \textbf{(11)}$$

where r is the radius of the particle and λ is the wavelength of radiation (both expressed in μm).

The size parameter allows us to define three regimes (**Figure 19**):
1- *Geometric Optics Regime* for particles having $x \gg 1$ or $D \gg \lambda$ (D is the diameter of the particle).
2- *Mie Regime* for particles having the same order of the wavelength or $D \approx \lambda$.
3- *Rayleigh Regime* for particles having $x \ll 1$ or $D \ll \lambda$.
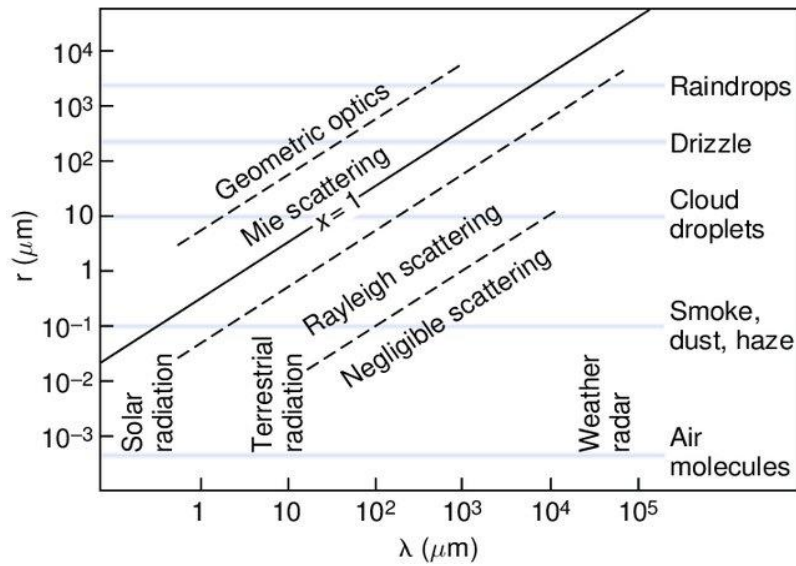
Figure 19 Size parameter x as a function of wavelength λ of the incident radiation and particle radius r *(Wallace and Hobbs, 2006)*.

Figure 20 shows the spectral distribution of extinction in the three scattering regimes for different particle diameters. The extinction is measured experimentally by Fourier Transform Spectrometers in IR, Vis-UV. Particularly, for atmospheric dust (between 10^{-2} and 10 µm), Mie Regime covers the most important for thermal infrared region (between 8 and 15 µm). A code is used in our work to simulate extinction spectra from Mie theory by knowing the size distribution and the complex refractive indices of dust and will be discussed in the next chapter.

Absorption dominates over scattering for sufficiently small absorbing particles ($D \ll \lambda$). If the particle is about the same size ($D \approx \lambda$) as or larger than the wavelength ($D \gg \lambda$), the extinction is due to both scattering and absorption.
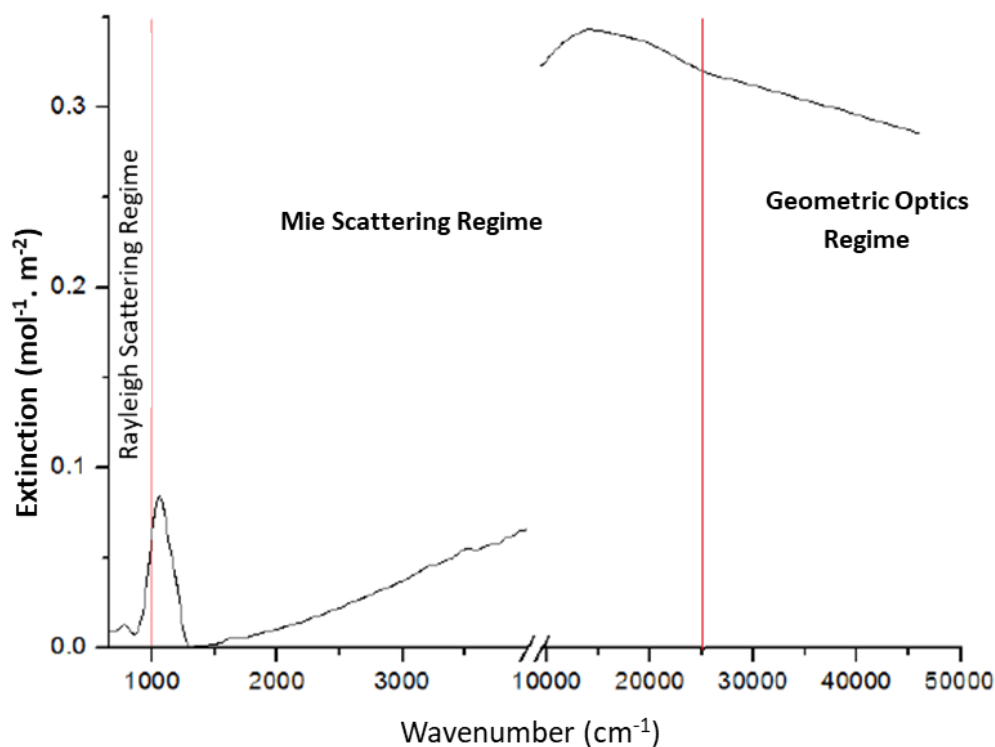
Figure 20 Extinction spectra of the three scattering regimes for a particle of 1 μm *(Deguine, 2018)*.

1.4.4 Particle Shape

In the case of mineral dust, the particles are not spherical and have various shapes. *Kalashnikova and Sokolik, 2004* showed that deviations from spherical behavior are mostly due to the scattering component of extinction since irregularly shaped particles have larger scattering efficiencies than spheres. In addition, particle absorption is much less sensitive to particle shape, therefore sphericity in thermal infrared was considered and Mie theory was applied *Di Biagio et al., 2017*. However, *Legrand et al., 2014* has shown that assuming sphericity gives some degrees of uncertainties in the longwave spectra, especially near the resonant peaks. Therefore, non-spherical theories are applied depending on particle symmetry,, i.e., the T-matrix method and Continuous Distribution of Ellipsoid – CDE *(Reed et al., 2017; Silvester and Ferrari, 1996)*.

1.4.5 Complex Refractive Index

The complex refractive index (CRI) is a fundamental parameter combined with the SD to characterize aerosols using remote sensing. It can be used to determine the link

between aerosols' chemical and optical properties. Many studies used it as a fixed input in inversion processes to solve retrieval problems *(Di Biagio et al., 2014b; Ryder et al., 2019)*.

The refractive index of a medium is a function of the wavenumber of the radiation under consideration. The refractive index characterizes the way the medium interacts with the electromagnetic radiation, giving a macroscopic description of the propagation of radiation in that medium, and it is written as follows:

$$m(v) = n(v) + i\,\kappa(v) \textbf{ (12)}$$

The real part $n(v)$ is the ratio of the speed of light in the medium to that in the vacuum, while the imaginary part $\kappa(v)$ characterizes the absorption of the medium. An example of the CRI for pure Quartz is shown in **Figure 21**.
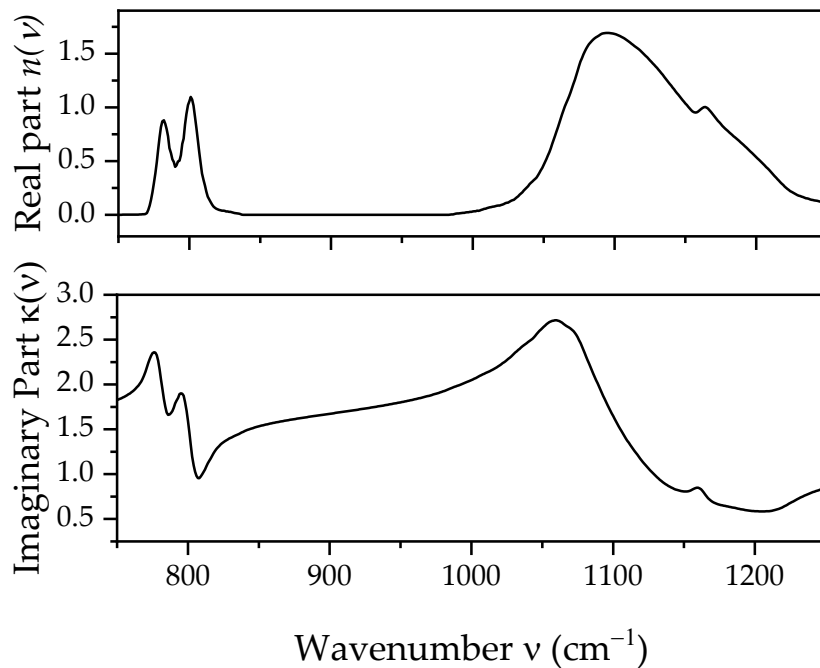
Figure 21 Spectral variation of the real part *n* and imaginary part *κ* of the CRI *(Deschutter, 2022)*.

Different techniques were previously used to retrieve the CRI of pure minerals that can constitute an aggregate of mineral dust, and are described as follows:

1- The *refraction method* is typically applied on a thin film or a prism sample. It measures the real refractive index calculated using a prism's minimum angle of deviation *(Born and Wolf, 1980)*,. The imaginary refractive index is considered insignificant for a non-absorbing medium. However, for absorbing medium, the imaginary part can be determined using the optical path through the light absorption prism by solving Maxwell's equation *(Sasaki, 2022)*.

2- The *reflection method* measures the reflection on aerosol powder films. Both real and imaginary parts can be calculated by substituting the reflectivity using two equations derived from Fresnel equations and Kramers-Kronig relations *(Kitamura et al., 2007)*. This method was used by *Peterson et al., 1969* and *Spitzer and Kleinman, 1961* for Quartz crystal and by *Querry et al., 1978* for clay minerals (i.e., Illite, kaolinite, and Montmorillonite).

3- The *transmission method* measures the transmittance of samples of thin homogeneous films where the reflectivity is negligible. *Egan and Hilgeman, 1979* used this method to calculate the CRI of clay minerals (Illite, Kaolinite…). In this method, the imaginary part is estimated, and the Kramers-Krönig relations are used to obtain the real part. In the case of a heterogeneous sample, the largest errors come from underestimating the scattering effect *(McPheat et al., 2002)*. Another limitation is the thickness of the sample film, which should be reduced to increase the transmittance: its value is very small for imaginary indices greater than 1. Hence, the method modifies the shape, size, and vibrational bounds, reducing a representative sample of atmospheric aerosols *(Felske et al., 2007)*.

4- The *particle's suspension method* overpasses the limitations of the previous method by measuring the transmittance of suspended particles *(Hubert et al., 2017)*. The CRI is then retrieved using an optimal estimation method to retrieve from a simulated spectrum an experimental spectrum by using Mie theory in the case of spherical particles and T-matrix in the case of non-spherical particles.

Different methods can be used to retrieve the CRI, and the studies remain limited in the covered spectral range. In our study, we use the CRI characterized from a Gobi Desert dust sample and individual minerals (quartz, illite and calcite), using mechanical shaking by the particle suspension method. The apparatus is optimized to decrease the volume of the chamber with a maintained aerosol flux during the extinction and size distribution

measurements. First, Mie Theory was used to simulate extinction spectra, and then the optimal estimation method was employed with Kramers-Krönig relations to quantify the CRI at a spectral resolution of 0.5 cm^{-1} *(Deschutter, 2022)*. The experimental setup is described in **Chapter III**.

1.5 MINERAL DUST DETECTION USING REMOTE SENSING

In order to better understand mineral dust properties and their impact, a large panel of methods has been developed during the last thirty years using remote sensing instruments. *Fischer et al., 1976* defined remote sensing as "*the art or science of telling something about an object without touching it.*". Technically, remote sensing instruments are sensors that measure, at a distance, the electromagnetic radiation interacting with an object.

1.5.1 Remote Sensing Process

The process of remote sensing consists of having a *physical object* interacting with the electromagnetic radiation detected by the instrument. The measured parameters are called the *sensor data* which are examined and analyzed by the scientists. From these datasets, *information selection* is performed with respect to the aimed *application* such as geology, meteorology, atmospheric sciences. The process of remote sensing is illustrated in **Figure 22**.

Figure 22 Remote sensing process *(Campbell and Randolph, 2011)*.

1.5.2 Key Concepts of Remote Sensing

Remote sensing instruments are characterized by the following key concepts:

1 – The *spectral differentiation* indicates how to distinguish between two different wavelengths and identifies the instrument's spectral resolution. These sensors can employ panchromatic, multispectral, or hyperspectral resolution measuring the acquired

quantity with multiple band combinations. These combinations differ by the number of channels. A comparison of different spectral resolutions is illustrated in **Figure 23**.
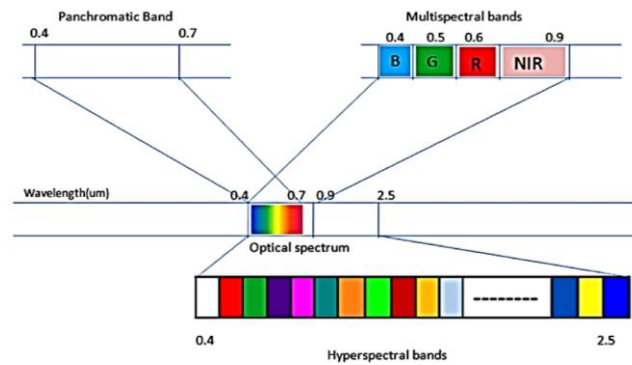
Figure 23 A comparison of sensors in terms of the width of bands *(Baisantry and Khare, 2016)*.

2- The *spatial resolution* describes the smallest area the sensing instrument can separately record as an entity or image. The minimum area (pixel) determines the spatial resolution of the instrument. The spectral and spatial resolutions are inversely proportional, as shown in **Figure 24**. In the design of optical remote sensing systems, owing the limited amount of incident energy, there are critical tradeoffs between the spatial resolution, the spectral resolution and signal-to-noise ratio (SNR). For this, optical systems can provide data with a high spatial resolution but with a small number of spectral bands (i.e., multispectral data from HIMAWARI). On the other hand, with a high spectral resolution and a high SNR, the spatial resolution is reduced. For example, the Infrared Atmospheric Sounding Interferometer IASI having a SNR of 500 with a high spectral resolution of 0.5 cm^{-1} but with a spatial resolution of 12 km.

| (a) | (b) | (c) |
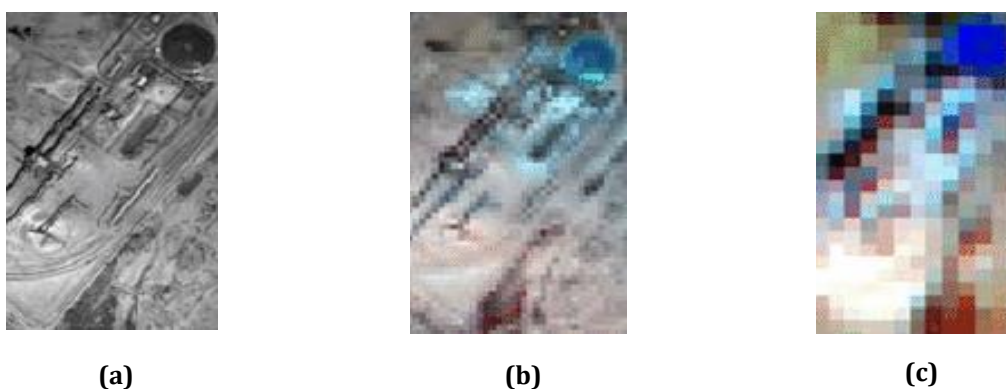
Figure 24 A comparison of spatial resolution between **(a)** panchromatic **(b)** multispectral **(c)** hyperspectral imagery *(Borstad et al., 2004)*.

3- The *spatial coverage* defines if the image coverage is global or local, complete or partial. Particularly, satellite's spatial coverage depends on the scanning, swath and observing cycle of the instrument. The scene can be observed with continuity i.e., the Visible Infrared Imaging Radiometer Suite (VIIRS) or can be sampled partially i.e., the Moderate Resolution Imaging Spectroradiometer (MODIS) as illustrated in **Figure 25**.

| (a) | (b) |
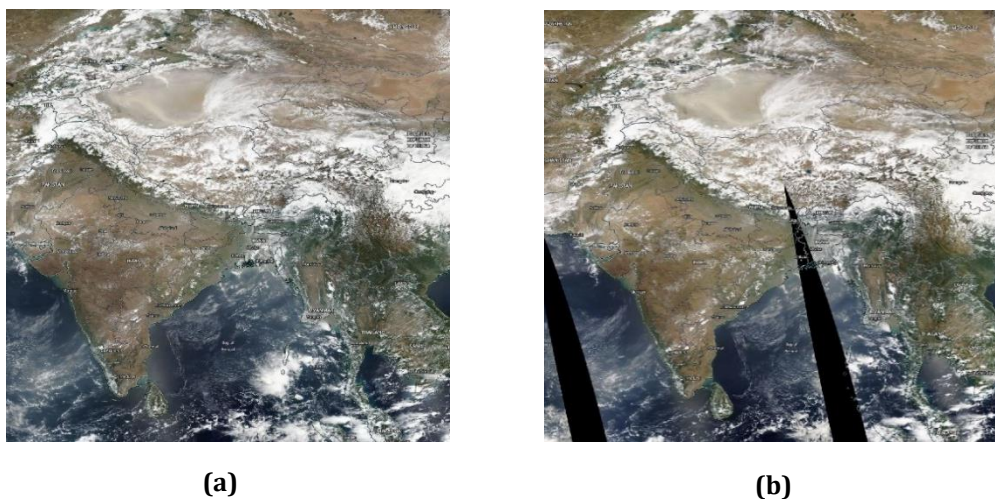
Figure 25 Spatial coverage of Central Asia in 19- 5-2019 **(a)** VIIRS imagery with continuous coverage **(b)** MODIS a sounder sampling with spatial gaps in black (https://worldview.earthdata.nasa.gov).

4- The *temporal resolution* describes the smallest time needed to detect the same region again and the use of information of the same region acquired over time. Although, for most satellites, two adjacent orbits overlap in the imaging swaths, and this overlap increases with increasing latitude, some areas of the Earth tend to be re-imaged more frequently. Also, satellite systems can point their sensors to image the same area between different satellite passes separated by one to five days. Thus, a sensor's actual temporal resolution depends on various factors, including the satellite/sensor capabilities, the swath overlaps, and latitude.

1.5.3 Active and Passive Remote Sensing

We can distinguish between active and passive instruments according to the radiation source used to detect an object. Active instruments use their light source, while passive instruments use natural radiation from the sun and Earth's surface from UV, Visible,

Infrared to Microwave (**Figure 26**). They can be located on the ground, in situ on balloons or aircrafts, and on satellites depending on the objective of measurement.
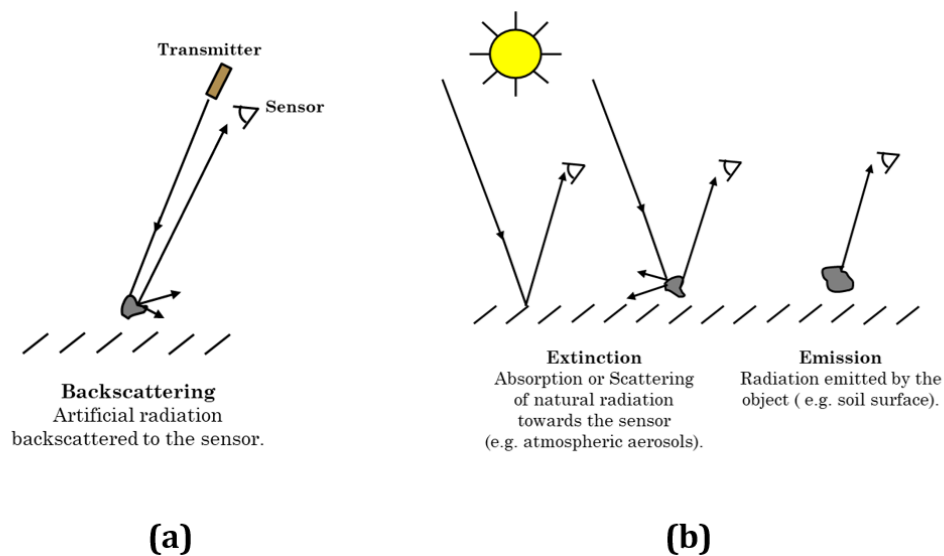
Figure 26 (a) Active sensors and **(b)** passive sensors detecting radiation signals.

Active instruments send a signal to an object and measure its feedback (intensity, time delay, and pulse modulation). The advantage of these sensors is that they can function independently of the sunlight. Radars and lidars are examples of active systems. Lidars can be found on the ground (i.e., EARLINET measuring vertical backscattering profiles of aerosols) or on a satellite, i.e., the Cloud-Aerosol Lidar with Orthogonal Polarization (CALIOP) on the CALIPSO satellite that provides dust altitude and layer thickness information *(Wainker et al., 2013)*. Moreover, radars give meteorological conditions 24h/24h. Knowing wind fronts' strength from radars can indicate the direction of the transported airborne dust.

Passive instruments, measure the terrestrial and solar radiation interacting with the object. Example sensors are photometers (i.e., AErosol Robotic NETwork, AERONET stations), or radio sounders (i.e., ERA5 providing surface temperatures at 10 m). They also can be radiometers that employ panchromatic (e.g., the Spinning Enhanced Visible and InfraRed Imager, SEVIRI) or multispectral (e.g., the Moderate Resolution Imaging Spectroradiometer, MODIS. Moreover, they can be spectrometers with hyperspectral resolution measuring the acquired quantity with multiple band combinations by the principle

of gratings (e.g., the Atmospheric Infrared Sounder, AIRS) or Fourier transform interferometry (e.g., IASI).

Using these instruments, we can directly measure the feedback of electromagnetic radiation when interacting with aerosols. Nevertheless, we can quantify different aerosol parameters. Major active and passive sensors are summarized in **Table.1**. AERONET photometers provide, from ground-based observations, inversion products of aerosol SD.

From satellite remote sensing, the vertical distribution of aerosols in the atmosphere (dust altitude and layer thickness) can be obtained by the spaceborne lidar CALIOP measuring the backscattered radiation *(Wainker et al., 2013)*. Daily observations in TIR from high spectral resolutions instruments also have shown the ability to derive the vertical dust plumes distributions originating from the Sahara. Mean monthly altitudes were previously derived from AIRS *(Pierangelo et al., 2004)* and IASI *(Capelle et al., 2014)*. Furthermore, IASI vertical profiles of concentration were retrieved for the Saharan dust plumes *(Vandenbussche et al., 2013)*.

On the other hand, quantitative estimates of the horizontal distribution of desert dust are done in terms of Aerosol Optical Depth (AOD). The geostationary satellite HIMAWARI 8 RGB *(Wang et al., 2019)* can differentiate natural dust from anthropogenic dust with lower AOD values. MODIS measurements in the near-infrared and visible are used above non-bright surfaces to measure the AODs *(Ginoux et al., 2010)*. In addition, dust AODs can be retrieved from UV to the near infrared using for example Ozone Monitoring Instrument (OMI) *(Torres et al., 2007)*. Recently, spaceborne spectrometers with high spectral resolution were used to retrieve the AODs of horizontal distribution of Saharan dust plumes from AIRS measurements *(Desouza-Machado et al., 2010)* and IASI *(Pierangelo et al., 2005)*. Moreover, AOD-altitude bins derived from IASI were used to detect daily dust emissions events *(Chédin et al., 2020)*. Aerosol retrievals from IASI also allowed to describe the 3D distribution and evolution of dust outbreak over East Asia *(Cuesta et al., 2015)*. In addition, the retrievals allowed the quantification of microphysical properties of the airborne dust from AIRS *(Pierangelo et al., 2005)*, and the coarse dust effective size was derived from IASI on a monthly basis *(Capelle et al., 2014).* IASI have also been used to detect different types of aerosols (i.e., volcanic ash) and retrieve their AODs and microphysical properties (Clarisse et al., 2010; Guermazi et al., 2021). The percentage mass fraction of clays only were previously obtained from IASI using experimental extinction

coefficients (illite, kaolinite and montmorillonite) *(Klüser et al., 2015)*. The latter work opens the perspective to retrieve the dust mineralogical composition from IASI observations which is the goal of this thesis.

Table 1 Different sensors types, functioning, measured and retrieved parameters.

Type	Sensors		Functioning	Measured Parameters	Retrieved Parameters	Example
Active Remote Sensing	Detection and ranging (DAR)	RADAR	Compares the characteristics of the transmitted and returned radio-energy, the timing of pulses, the wavelengths, and the angles	Radiofrequency amplitude, pulse width, angle of arrival, time of arrival, and modulation of pulse		Sentinel-1B
		LIDAR	Assesses the brightness of the backscatter and its angular position, changes in frequency, and the timing of reflected pulses	Backscattering Coefficient	Atmospheric aerosol and cloud Height and Thickness	CALIOP, EarthCare
Passive Remote Sensing	Photometer		Measures the strength of electromagnetic radiation and convert light into an electric current	Spectral Radiance	Aerosol Size distribution and refractive indices,etc	AERONET
	Radiometers	Imaging Radiometers	Scanning capability to provide a two-dimensional array of pixels to produce an image		Total column of Aerosol Optical Depth and type	SEVIRI, HIMAWARI
		Spectro-Radiometers	Measures the intensity of radiation in multiple wavelength bands			MODIS
	Spectrometers	Gratings Spectrometers	Measures the spectral content of incident radiation using the law of interference from the principle of grating diffraction		Aerosol Optical Depth, Altitude, Effective Radius, and Concentration	AIRS, OMI
		Fourier Transform Spectrometers	Based on the interference phenomenon of two electromagnetic waves using the principle of an interferometer			IASI

1.6 EAST ASIAN DESERTS

East Asia is the second-largest mineral dust source in the world after the Sahara, and it can produce up to 800 Tg per year of mineral dust *(An et al., 2018)*. Strong winds lift and transport large amount of mineral dust every year, mostly in winter and spring *(Xie et al., 2019)*.

To better understand the dust storms in this region, one should look at the topography in East Asia with alternating high mountains and basins. A diverse regional structure

with desert surfaces, i.e., the Gobi and Taklamakan, as well as the Horqin Sandy Land between North China and Mongolia. In contrast, more vegetation covers the eastern regions with more urban and populated cities, such as Shandong (**Figure 27**).

The Gobi Desert, Taklimakan Desert, and nearby plateaus are considered the primary dust sources in this region *(Wu et al., 2016)*. These deserts are affected by both the East Asian monsoons and the global westerlies, and a change in either of these systems influences regional climate. Dust masses are transported downwind from Mongolia and China *(Chen et al., 2015)*, crossing the Korean Gulf and Japan *(Mikami et al., 2006)* to the Pacific Ocean until reaching the North American continent *(Guo et al., 2017)*, and sometimes reaching Europe *(Grousset et al., 2003)*. One of the particularities of this region is the diversity in its mineralogical composition; the dust is rich in silicates and carbonates, which are considered as dust source tracer in East Asia *(Young Jeong, 2020)*.
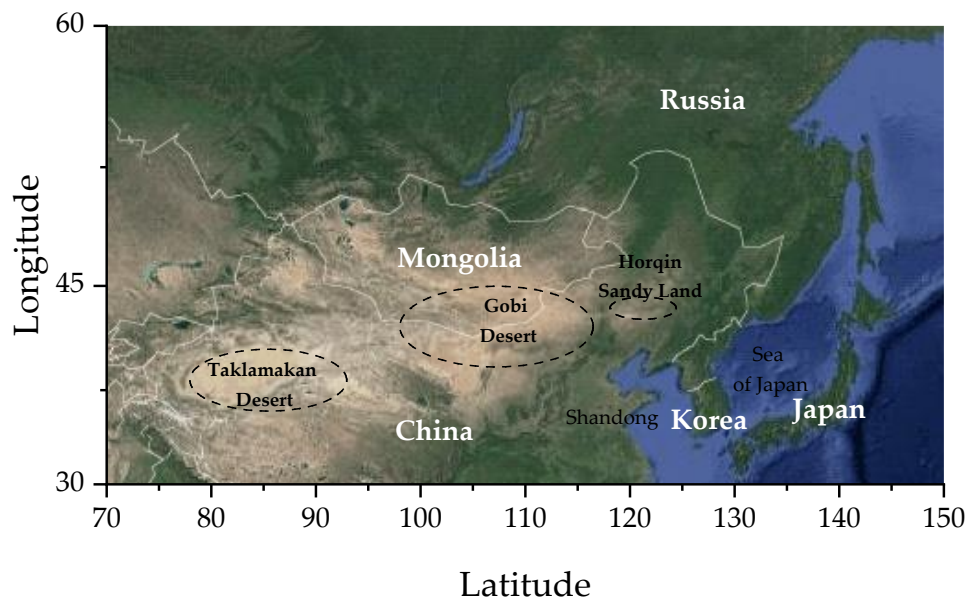
Figure 27 Topography of East Asia.

Satellite remote sensing detection above this region encounters many challenges. In particular, East Asian dust is uplifted near the surface in the low troposphere above the continent *(Chen et al., 2017)*, where the Land Surface Emissivity (LSE) variability in the Infrared affects remote sensing detections *(Masiello et al., 2014)*. This limitation presents a primary error source, as it impacts clear sky and dust layer detection above the land *(Ackerman, 1997)*.

Airborne dust can alter the Earth radiative budget by changing the atmosphere's absorption and scattering properties. In addition to the impact on the Earth's climate and ecosystem, human activity, health and regional visibility. **Figure 28** shows the impact of a desert storm occurred in the beginning of May 2017 on the visibility in Beijing in two days difference.

Figure 28 The central business district in Beijing on the 25 April 2017 (Left) and after a dust storm swept through in the next days. (Credits to *Nicolas Asfouri, Agence France Presse-Getty Image*).

1.7 OBJECTIVE

We introduced in this chapter, mineral dust cycle and its impact on the climate system. To better understand that impact, remote sensing observations proved the ability to quantify the aerosol chemical and microphysical properties from space. However, the retrieval remains challenging due to the variability and diversity of these properties depending on different dust sources and changes occurring during transport. The objective of this work, is to retrieve aerosol chemical properties of East Asian dust plumes from IASI observations in TIR, using new experimental optical properties measured in the laboratory (extinction coefficients of pure minerals).

The thesis aims first, to overpass the challenge of remote sensing observations above land caused by the LSE that alters dust observations in TIR. This parameter will be discussed in **Chapter II**, and a developed method will be described to overcome this

limitation allowing us to characterize and quantify different airborne mineral dust properties.

Second, after LSE optimization, we use new pure minerals extinction spectra and test them to reproduce experimental Gobi dust extinction spectrum, which allow us to calculate the mass fraction of major mineralogical families composing desert dust. Then, we derive the optical thickness from IASI observations to quantify from its spectral features the mineral composition and plot the evolution of the mineralogical composition during dust events. The final aim is to link the composition results to different dust sources in East Asia (**Chapter III**).

CHAPTER II. DUST DETECTION USING IASI

The chapter introduces the high spectral resolution remote sensing instrument used to detect and characterize mineral dust properties, the Infrared Atmospheric Sounding Interferometer (IASI). First, an overview of the sensor's satellite MetOp is provided. Then, we briefly explain its optical architecture and the optical principle employed to measure the IR radiation to describe the IASI characteristics, leading us to define the radiative transfer equation. Second, we elaborate on the different atmospheric constituents detected by the IASI: gases, aerosols, and clouds. We will particularly focus on the mineral dust detections having spectral features in the TIR region and study the emitted dust from East Asian deserts in the low troposphere above land. Finally, as the land surface emissivity (LSE) poses large constraints due to its high variability, we discuss how its signal affects the IASI spectra and we introduce an LSE optimization method to enhance mineral dust detections above land and quantify its chemical and microphysical properties (**Chapter III**).

2.1 INSTRUMENT PRESENTATION

2.1.1 MetOp Satellite

The METeorological OPerational Satellite (MetOp) is a satellite series launched as a low-Earth-orbiting sun-synchronous satellite at an altitude of about 800 km. The series delivers high-resolution sounding and high-resolution imagery in global coverage. IASI is one of eight meteorological instruments on MetOp *(Hilton et al., 2012)*. Developed by CNES and in cooperation with EUMETSAT, three sun-synchronized METOP satellites (A, B, and C) have been launched in the last 15 years with IASI-A, B, and C on board. In the next 20 years, a new generation of IASI-NG will continue the IASI mission with increased resolution and radiometric performance *(Crevoisier et al., 2014)*. **Figure 29** shows the MetOp payload and IASI optical system.
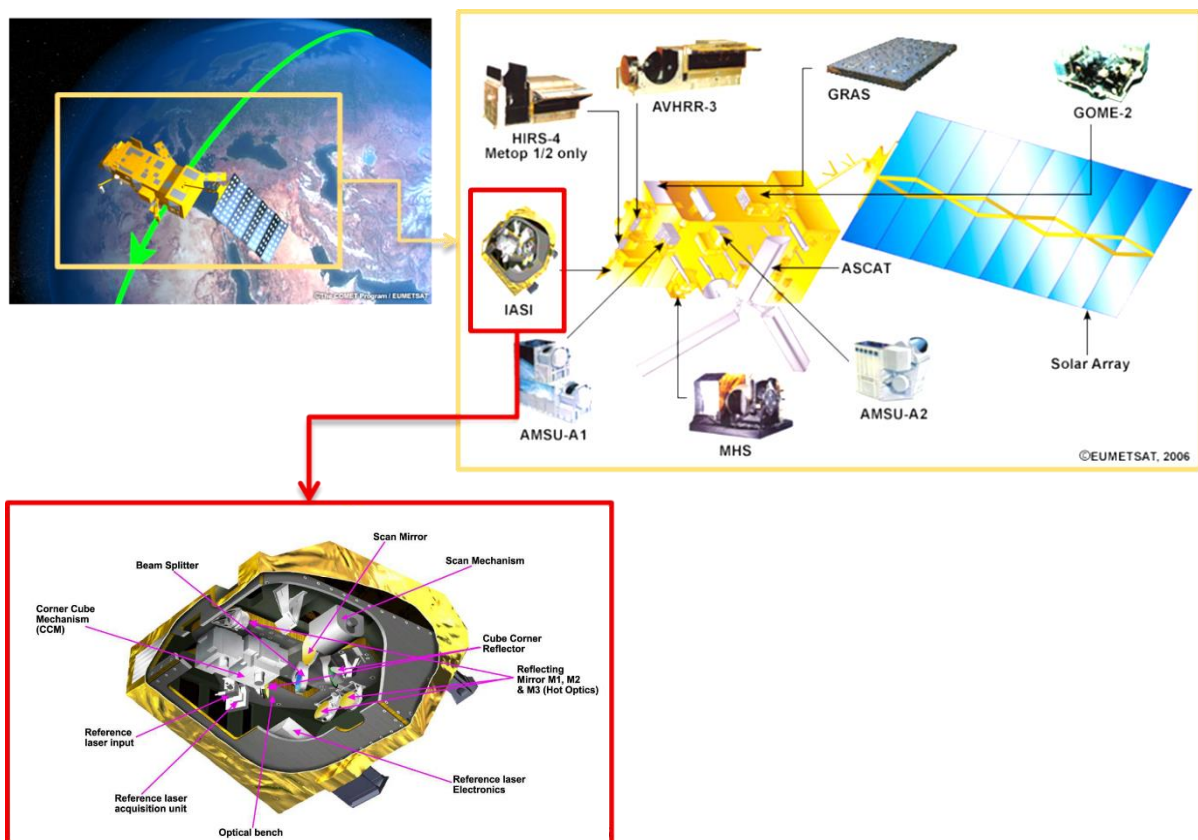
Figure 29 The MetOp satellite and its payload with a closer look on IASI system *(eumetsat.int)*.

MetOp makes 14 orbits around Earth, ensuring global coverage. IASI is on board with daytime and nighttime detections for a temporal resolution of about 12 h. The

satellite scans from a low altitude sun-synchronous orbit, in nadir view - the observation points on the surface Earth that are directly below the satellite trajectory. **Figure 30** illustrates the ground track of IASI/MetOp orbits around the globe.
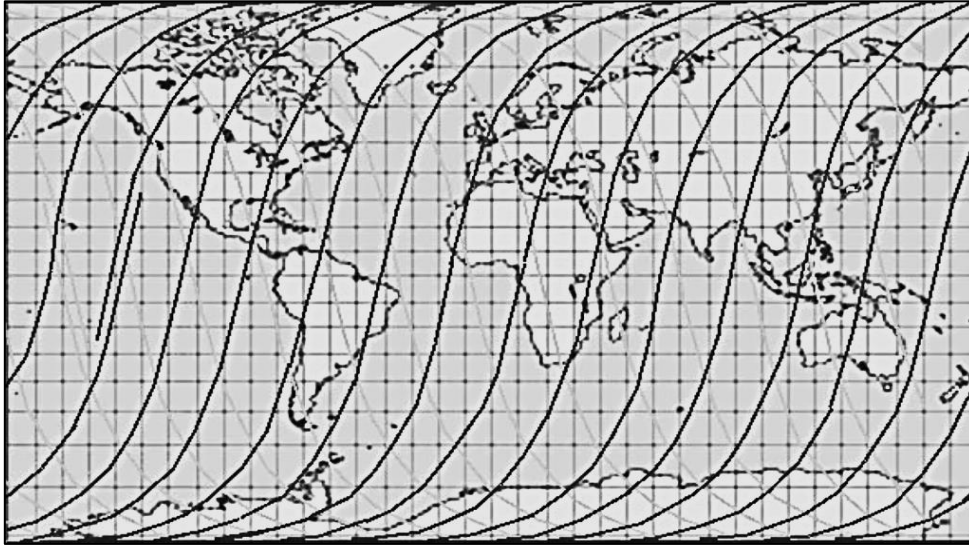
Figure 30 Ground track of MeTop satellite for 24h *(Herbin and Dubuisson, 2015)*.

2.1.2 The Infrared Atmospheric Sounding Interferometry (IASI)

IASI is an Infrared Fourier Transform Spectrometer, based on the Michelson interferometer principle. As shown in **Figure 31**, the radiation beam is scanned by a scan mirror, then is directed by the entrance mirrors M1 and M2 to a semi-reflective beam splitter that splits the incident beam into two waves into two cubes corners, one fixed, and the other moving parallel to the beam, the reflected beams recombine into one wave with an optical path difference then directed to the exit mirrors M3 and M4. These elements form the Interferometer Hot Optics Subassembly IHOS module and are linked to a cold box which transmits the signal to the detectors. In addition, there is the electronic module that guides the cube-corner mechanism and the laser module that controls loop electronics dynamics.
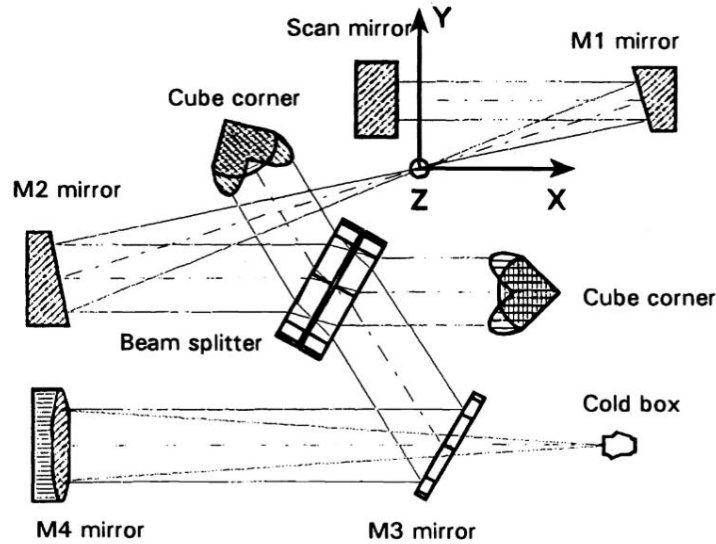
Figure 31 IASI optical functioning *(Cayla and Javelle, 1995)*.

The instrument has a swath of 2200 km with each field of view corresponding to 2 ×2 circular pixels, each with a 12 km diameter footprint in nadir. It observes Earth up to an angle of 48.3° on both sides of the satellite track. **Figure 32** shows the IASI swath scan and the field view with the corresponding pixels.
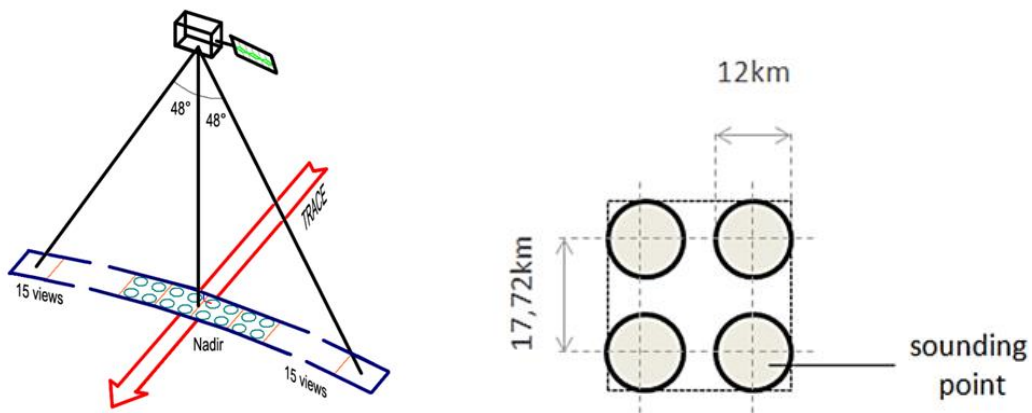
Figure 32 IASI swath angle and field view pixels *(Clerbaux et al., 2009)*.

With a continuous spectral radiance $R(v)$ characterizing the radiation source of a wavenumber v, the two coherent waves lead to an interference and the amplitude of the output wave depends on the optical path difference x, leading to the following interferogram:

$$I(x) = \int_0^\infty R(v)(1 + \cos(2\pi\gamma x))dv \quad \textbf{(13)}$$

The interferogram is the sum of a constant term and the real part of the Direct Fourier Transform of $R(v)$. The first term is not used in spectroscopy but the second term is used to retrieve the spectral radiance by the Inverse Fourier transform, and it is given by:

$$R(v) = \int_0^\infty I(x)cos(2\pi vx)\, dx \quad \textbf{(14)}$$

The interferogram should be sampled at very stable and regular positions of the moving mirror. Using a stable clock is not sufficient as it affects the speed of the moving corner cube. Instead, a reference zero-crossings laser beam triggers the sampling. Hence the interferogram has a finite number of values x limited by the maximum of the optical path difference allowed by the moving corner. The measurement is made with a maximum optical path difference of $x_{max} = 2$ cm. **Figure 32** shows an example of IASI interferogram $I(x)$ (Panel **(a)**), and the spectral radiance using the mathematical Fourier Transform (Panel **(b)**).
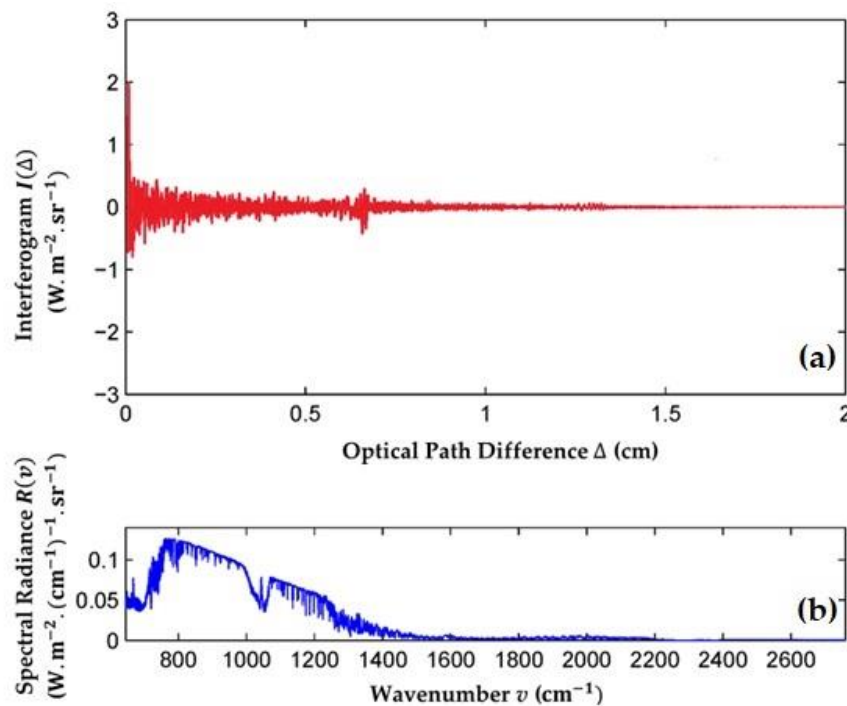
Figure 33 Example of IASI **(a)** interferogram; and **(b)** its spectral radiance using Fourier transform (Reproduced from *Grieco et al., 2010*).

IASI measures the spectrum of infrared radiation emitted by the Earth and the atmosphere. The sensor covers a continuous infrared spectral range between 645 and 2760

cm^{-1} (3.62 and 15.5 μm) and provides 8461 channels with a high spectral resolution of 0.5 cm^{-1} and low radiometric noise *(Blumstein et al., 2004)*. With this feature, IASI can provide day/night detections and ocean/land measurements at a high spectral resolution and a low radiometric noise (**Figure 33**).
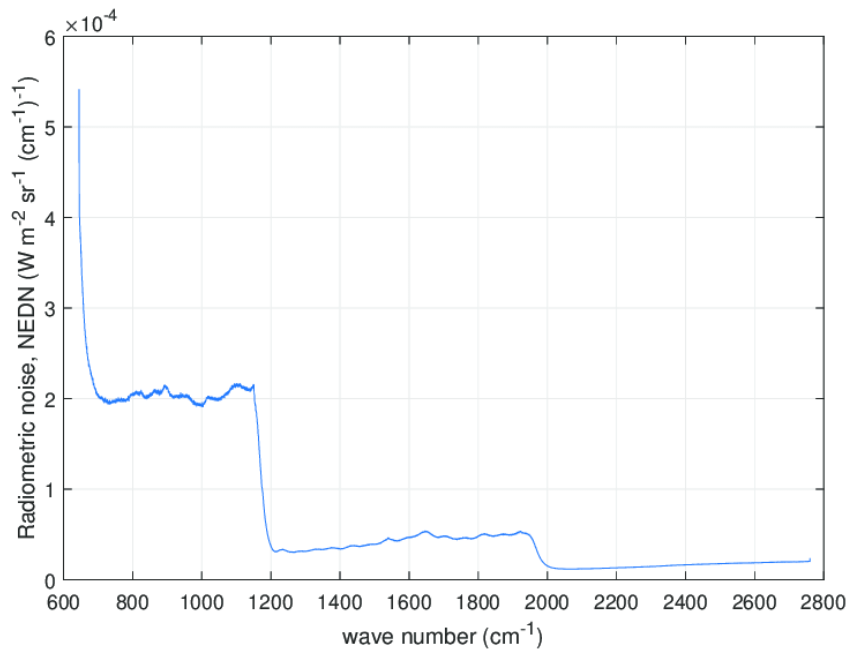
Figure 34 IASI-C radiometric noise averaged over one field of view of four pixels *(Serio et al., 2020)*.

2.1.3 Radiative Transfer Equation

The RTE describes the atmospheric state and the radiative processes absorption, scattering and thermal emission. A realistic representation of the atmosphere is a complex problem since the distribution of atmospheric components and parameters is not homogeneous.

Nevertheless, most radiative transfer codes divide the atmosphere in a finite number of horizontal layers for which homogeneous atmospheric properties can be assumed (*Clarisse et al., 2019; Herbin and Dubuisson, 2015*). Therefore, we will consider that Earth's atmosphere is highly stratified and can be assumed to be divided into horizontal homogeneous layers (**Figure 35**). Each layer has its pressure, temperature, and optical

properties. In addition, each atmospheric column is discretized and considered independent from another columns.
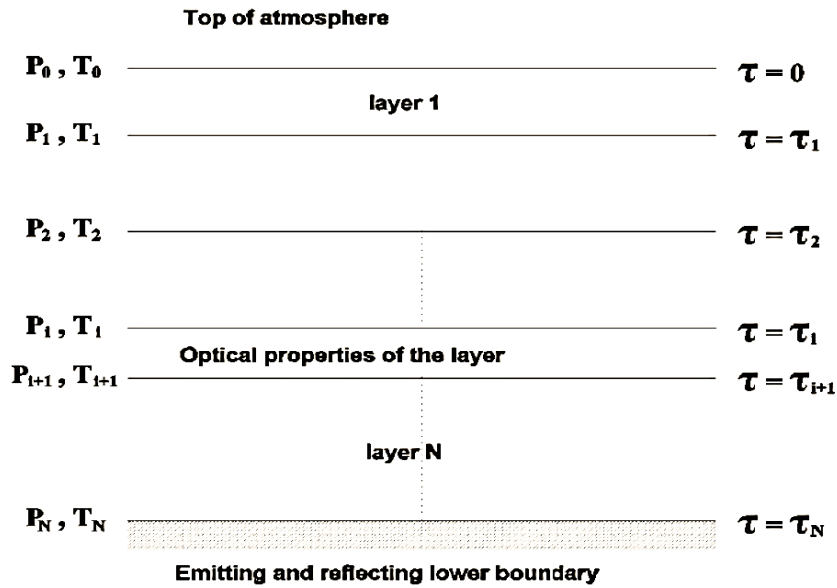
Figure 35 An atmosphere divided homogeneous layers *(Herbin and Dubuisson, 2015).*

We consider that the atmosphere is stratified into plane, parallel and homogeneous layers. The integration of **Equation (3)** from Earth's surface to the top of the atmosphere having an altitude H. For IASI viewing in nadir it is written as follows:

$$R(v) = \varepsilon(v)B(v,T_s)e^{-\int_0^H k(v,h)dh} + \left(1 - \varepsilon(v)\right)(\int_0^H k(v,h)B(v,T) \ e^{-\int_0^h k(v,h')dh'}dh +$$
$$I_s e^{-\int_0^H k(v,h)dh})e^{-\int_0^H k(v,h)dh} + + \int_0^H k(v,h)B(v,T)e^{-\int_h^H k(v,h)dh}dh \quad \textbf{(15)}$$

The first term represents the radiance directly emitted by the surface with a skin temperature T_s having a blackbody emitted radiation $B(v,T_s)$, an emissivity $\varepsilon(v)$, and attenuated by the atmospheric column above the surface having a total extinction $k(v,h)$, which expresses the sum of gaseous $k_{ext}^{gas}(v,h)$, aerosols $k_{ext}^{aerosol}(v,h)$ and clouds $k_{ext}^{cloud}(v,h)$ extinction coefficients, and it is given as follows:

$$k(v,h) = k_{ext}^{gas}(v,h) + k_{ext}^{aerosol}(v,h) + k_{ext}^{cloud}(v,h) \textbf{(16)}$$

The second term expresses the down welling radiance from the sun radiance *Is* and the atmospheric layer at altitude h, describing the radiance contribution emitted from the

atmosphere towards surface, that is back-reflected from it and then reaches the satellite. The third term represents the upwelling radiance directly emitted from the atmosphere along the slant path in the viewing direction, integrated along the whole path (**Figure 36**). Note that the second term only affects the shortest IASI wavelengths.
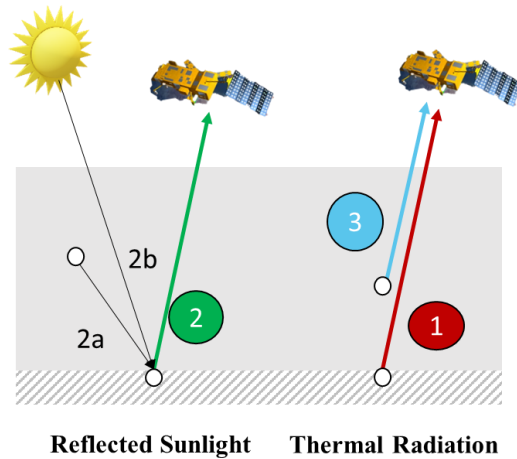
Figure 36 Nadir viewing observation of the radiation coming from the Earth's surface (1), the atmosphere (2a and 3) and the sun (2b).

2.2 ATMOSPHERIC SPECTRAL DETECTION

IASI captures the Earth's blackbody radiation signal in the longwave infrared. The radiation thermal radiation emitted by land/ocean surfaces and the atmosphere, in addition to the reflected sunlight pass through the atmosphere (gases, aerosols, and clouds), resulting in a modification in the signal received by the sensor along the path. A molecule modifies the spectrum at specific wavenumbers due to its rotation-vibration transitions.

The *Brightness Temperature* or *apparent radiation temperature* $T_B(v)$ (in K) is defined as the temperature of a blackbody outputting the same radiance as that measured for its surface at a given wavenumber and calculated from the spectral radiance:

$$T_B(v) = \frac{\frac{hcv}{k_B}}{\ln\left(\frac{2hc^2 v^3}{R(v)}+1\right)} \textbf{ (17)}$$

The primary objective of IASI mission is to provide high spectral resolution measurements that estimate humidity and temperature profiles in numerical weather predictions. However, since its launch it has also provided monitoring atmospheric

constituents, including gases, aerosol and cloud detections that were not initially ex-
pected *(Hilton et al., 2012)*.

Figure 37 shows how IASI brightness temperature spectra are affected by gas mo-
lecular absorptions for a clear sky above the sea; the major difference with a clear sky
above the desert is caused the surface emissivity signal that highly alters the spectral de-
tection. Mineral dust and ice cloud detection examples show different spectral features
depending on the layer's chemical and microphysical properties. First, we shall describe
the absorbing gases that alter the IASI spectra. Then, we will focus on the atmospheric
window where mineral dust is detectable. However, the contribution of the land surface
effect can be important. Therefore, we elaborate on the attributed spectral change by the
surface in the TIR atmospheric window.
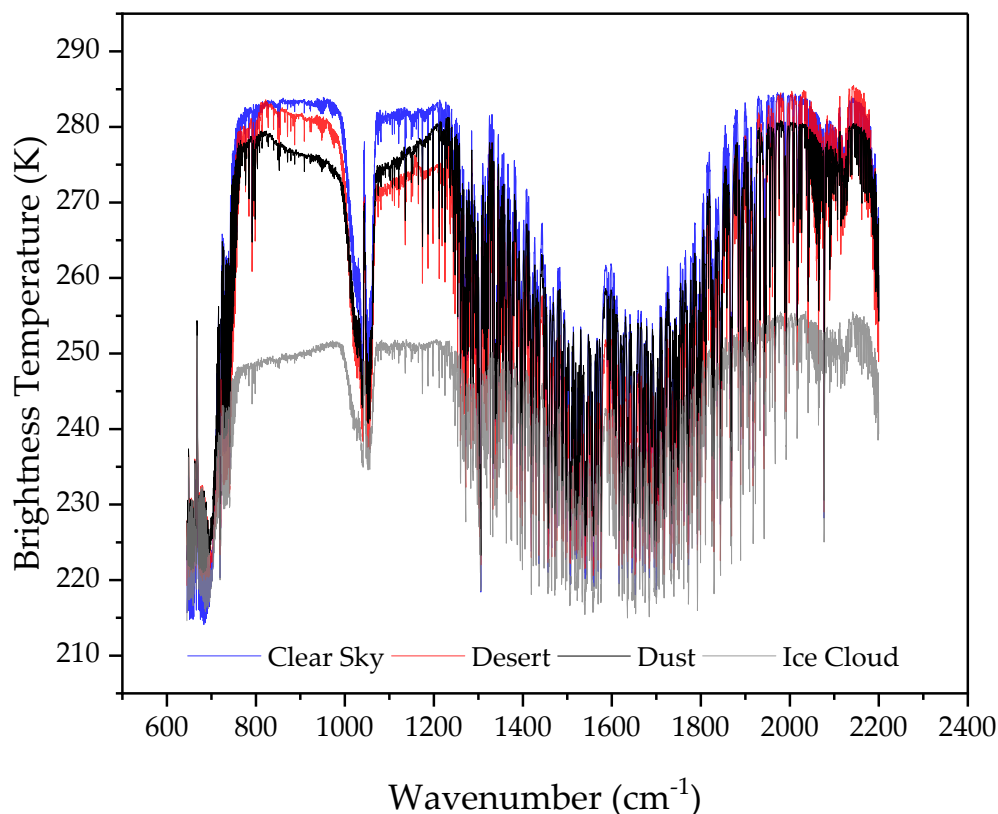
Figure 37 Examples of IASI brightness temperature spectra for a clear sky scene, a scene above
the desert, a scene containing dust and another containing ice cloud. Spectral channels after 2220
cm^{-1} were removed due to solar reflectance term that we disregard in our work.

2.2.1 Atmospheric Gases Detection

Although not IASI's primary objective, it has demonstrated its ability to detect different gas extinctions, according to **Equation (15)** and **(16)**. In the infrared, the gases have negligible scattering coefficient, and the absorption is dominant. Hence, the total gas extinction is equivalent to the gas absorption coefficient ($k_{ext}^{gas} = k_{abs}^{gas}$). Water vapor is the dominant absorber in the IASI spectrum since it constitutes the most abundant gas in the atmosphere *(Herbin et al., 2009)*. Water vapor molecules include $H_2^{16}O$ and different isotopologic species (i.e., $H_2^{18}O$ and HDO). Other strong absorbers are carbon dioxide (CO_2) and nitrous oxide (N_2O), with stable atmospheric concentrations and long lifetimes. The spectrum is also sensitive to Ozone (O_3) signature, methane (CH_4), and carbon monoxide (CO). In addition, the spectrum includes features from the weak absorbers, nitric acid (HNO_3) and chlorofluorocarbons CFC-11 and CFC-12. Other weak absorbers results are seen in concentrated plumes, i.e., sulfur dioxide (SO_2) plumes ejected in volcanic explosions *(Clarisse et al., 2008)* and the detection of emission sources of short-lived trace species, such as ammonia (NH_3), methanol (CH_3OH), and formic acid (HCOOH) has been possible *(Van Damme et al., 2014)*. **Figure 38** shows the main gas species detected by IASI, in total the instrument components are already detected.
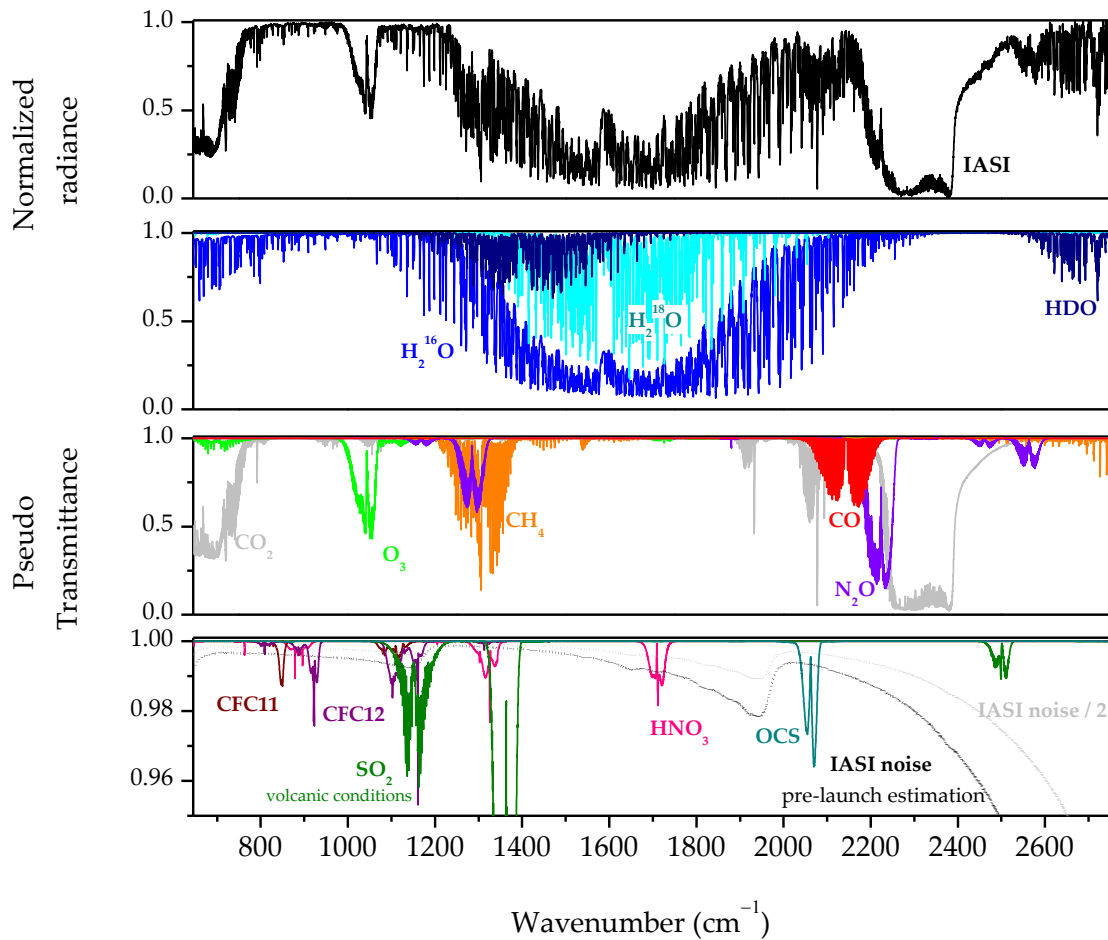
Figure 38 Top panel: radiance atmospheric spectrum (in normalized units) recorded by IASI/MetOp, over West of Australia, on 20 December, 2006. Middle panels: radiative transfer pseudo-transmittance simulations to identify the main absorbing gases (middle panels) and the weaker absorbers compared with the IASI noise (lower panel) *(Clerbaux et al., 2009)*.

2.2.2 Airborne Mineral Dust Detection

In addition to the gas species, the IASI signal can be altered through the aerosol extinction $k_{ext}^{aerosol}(v, h)$ from **Equation (16)**. Due to the high spectral resolution of IASI and its sensitivity to various aerosol spectral signature in TIR, the detection and classification of aerosol types (including volcanic ash, desert dust and biomass burning) within plumes is possible *(Clarisse et al., 2010)*. Particularly, airborne mineral dust is formed by external or internal mixtures of silicates and carbonates minerals, therefore IASI is sensitive to mineral dust spectral signature in the TIR, having absorption features between 750 and 1250 cm⁻¹ where the atmosphere is mostly transparent. The strongest feature is caused

by O-Si-O asymmetrical stretching caused by mineral molecules i.e., illite and quartz *(Madejová et al., 2017)*. Other modes can also be detected in the atmospheric window i.e. the -OH bending in clay minerals *(Madejova and Komadel, 2001)*, and the C-O asymmetrical stretching in carbonates (i.e., calcite, dolomite). However, the C-O symmetrical stretching in carbonates is masked near 1400 cm^{-1} by the water vapor continuum. The IASI spectrum reaches its maximum transmittance at 781.25 and 1235.25 cm^{-1}, by these extremities and the dust absorption feature, a V-shaped brightness temperature spectrum is detected *(Xuan and Sokolik, 2002)*. **Figure 39** shows a forward model simulation of IR spectrum of an empty atmospheres (i.e., empty from gases) with a single layer of Gobi Desert dust ($r_g = 0.25$ μm; $\sigma_g = 2$μm) compared with an IASI Gobi dust observation.
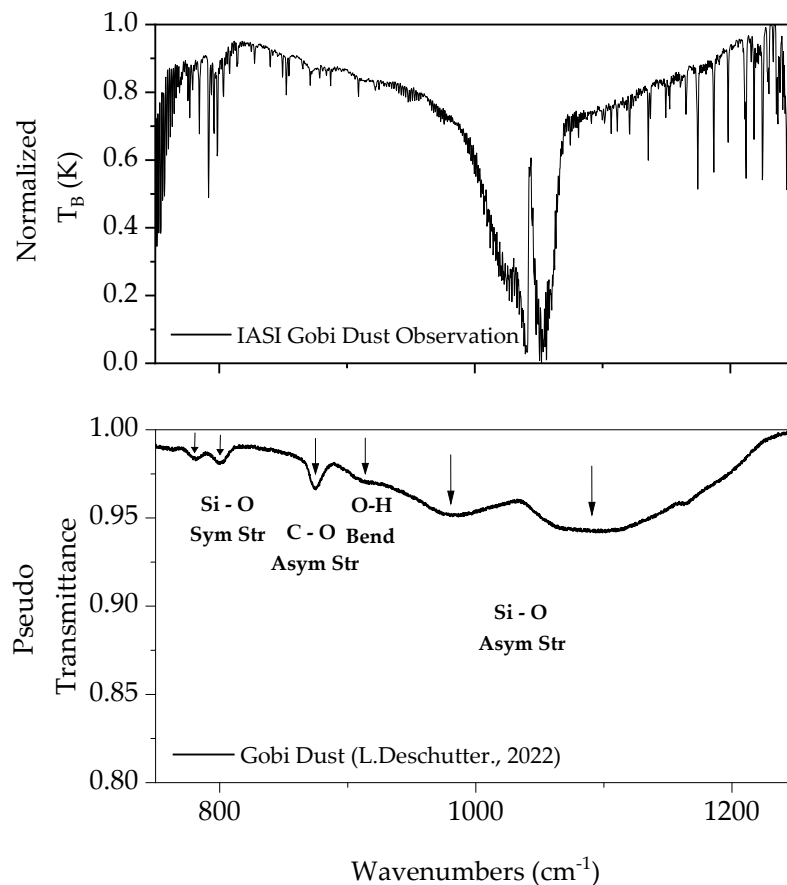
Figure 39 Top panel: brightness temperature detection of Gobi dust. Low panel: forward model simulation of an empty atmospheres with a single layer (2 Km) of Gobi Desert dust ($r_g = 0.25$ μm; $\sigma_g = 2$ μm). Sym Str: symmetrical stretching; Asym Str: asymmetrical stretching; Bend: bending.

2.2.3 Surface Emissivity

One of the most important parameters in the RTE **Equation (15)**, is the surface emissivity $\varepsilon(v)$, since it can significantly affect the detected IASI signal. It depends on the soil composition, diurnal and seasonal variability. **Figure 40** shows the spectral emissivity of four surface types. The desert surface emissivity is highly variable since it is highly rich in Quartz in the thermal infrared, while other types show values close to 1.
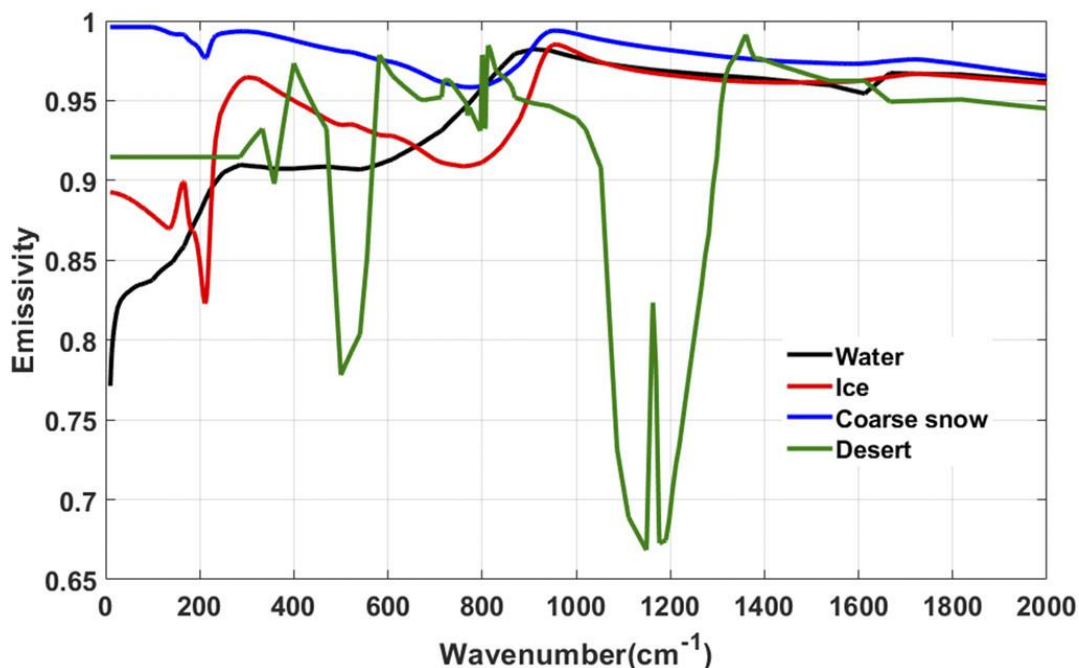
Figure 40 Spectral emissivity of water, ice, coarse snow and desert *(Huang et al., 2018)*.

To test the different surfaces effect, we take two IASI observations from the same scanning track time and date: one of a clear sky above the Sea of Japan and another of a clear sky above the Gobi Desert from the 3 May 2017 shown in **Figure 41**. An observation of a clear sky above the sea with a negligible LSE contribution shows a flat brightness temperature spectrum in the atmospheric windows (780 to 980 cm^{-1} and 1070 to 1210 cm^{-1}). Conversely, a clear sky above the desert spectrum has high LSE spectral variability that is characterized by a peak at 1159 cm^{-1}, with a decrease in its brightness temperature between 1069 and 1250 cm^{-1}. These two features appear due to a high reflectance phenomenon called the *Reststrahlen Effect* arising from and between coherent oscillations of the vibrational optical phonons *(Caldwell et al., 2015; Griffiths and De Haseth,*

2007). In particular, it is confined between Transversal Optical (TO) and Longitudinal Optical (LO) phonon modes of Quartz, most dominant mineral in desert surfaces *(Winta et al., 2018)*. It is triggered by a sudden drop in the real refractive index value. As the real part becomes smaller than the imaginary part, the reflectance increases to a value of 1, which results in a quartz-rich surface decrease in the LSE to values of less than 1 in the Reststrahlen region.
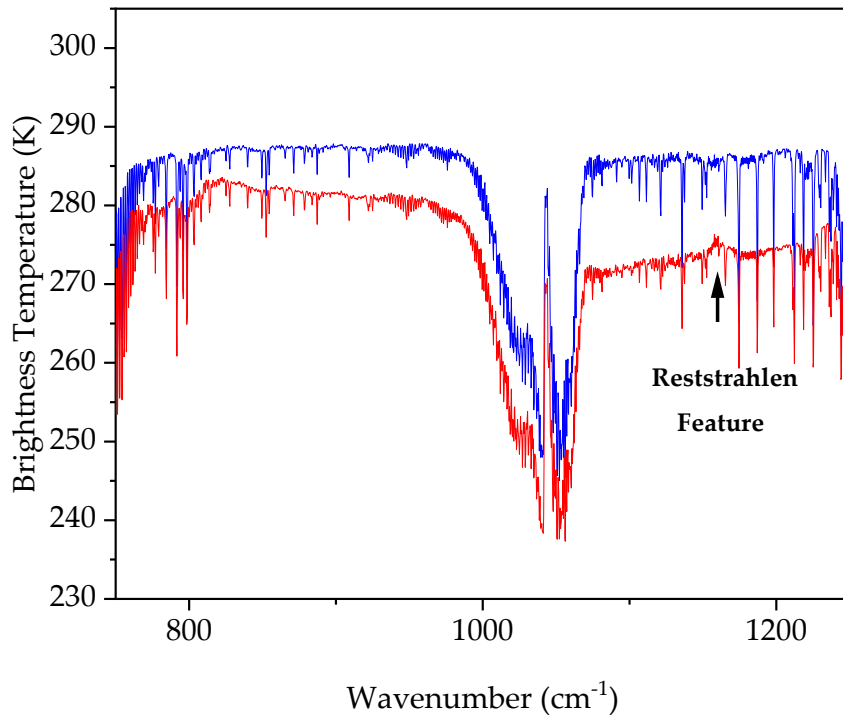
Figure 41 IASI detection example of a clear sky above the Sea of Japan (in blue), and a clear sky above the Gobi Desert (in red) in 3 May 2017. The black arrow indicates the Reststrahlen feature.

2.3 SURFACE IMPACT ON DUST DETECTIONS

We are interested in detecting aerosols from IASI detections from the atmospheric windows where only spectral gas lines are exhibited. However, the LSE signal can affect this spectral region when aerosols are detected above the desert. In this section, we will discuss the impact of the LSE on dust selection during a dust storm and the use of an LSE dataset derived from IASI from the literature to account for its effect. However, its direct use can over represent or under represent the IASI spectrum. Therefore, we introduce a

new LSE optimization methodology that corrects these datasets and optimizes spectral detection.

2.3.1 Dust Selection

We use the 'V-shape' dust criteria to select IASI dust spectra. We do this by computing the difference in the brightness temperature ΔT_B, calculated by subtracting two brightness temperature values T_{B,v_1} and T_{B,v_2} for two wavenumbers v_1 and v_2 respectively, and is written as follows:

$$\Delta T_B = T_{B,v_1} - T_{B,v_2} \text{ (18)}$$

The choice of the channels in equation **(18)**, depends on two factors:

1- Concentration variability: **Figure 42** shows the simulated spectra of an empty atmosphere with a single layer of Gobi Desert dust ($r_g = 0.25$ μm; $\sigma_g = 2$ μm; $L = 2$ Km), showing the Aerosol Optical Depth (AOD) as function of the concentration. As the concentration increases, the 'V-shapes' becomes more inclined and the measurement is more sensitive to the concentration variation in the atmospheric windows.
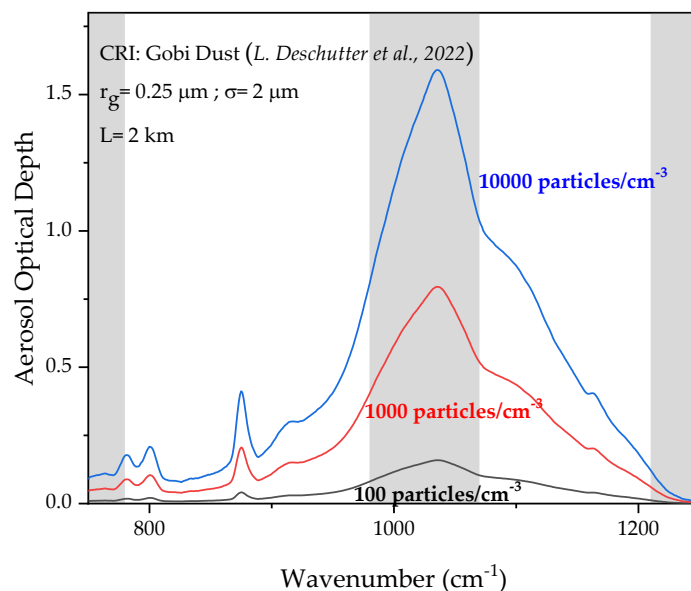
Figure 42 The variation of the AOD as function of the concentration from simulated spectra of an empty atmosphere with a single layer of Gobi Desert dust using a Mie code and Gobi dust CRI. Gray patterns indicate important gases absorption bands from the order of increasing wavenumbers CO_2, O_3, and H_2O.

2- Gases narrow bands: These bands can alter the radiance spectral value depending on the gas's concentration in the atmosphere. We tested empirically hundreds of mineral dust spectra to find the best channels that minimizes the impact of gases on the ΔT_B calculation. In this study, we use two ΔT_B for dust selection: $\Delta T_{B1} = T_{B,811.25} - T_{B,988}$ and $\Delta T_{B2} = T_{B,1191.25} - T_{B,1112}$ (**Figure 43**).
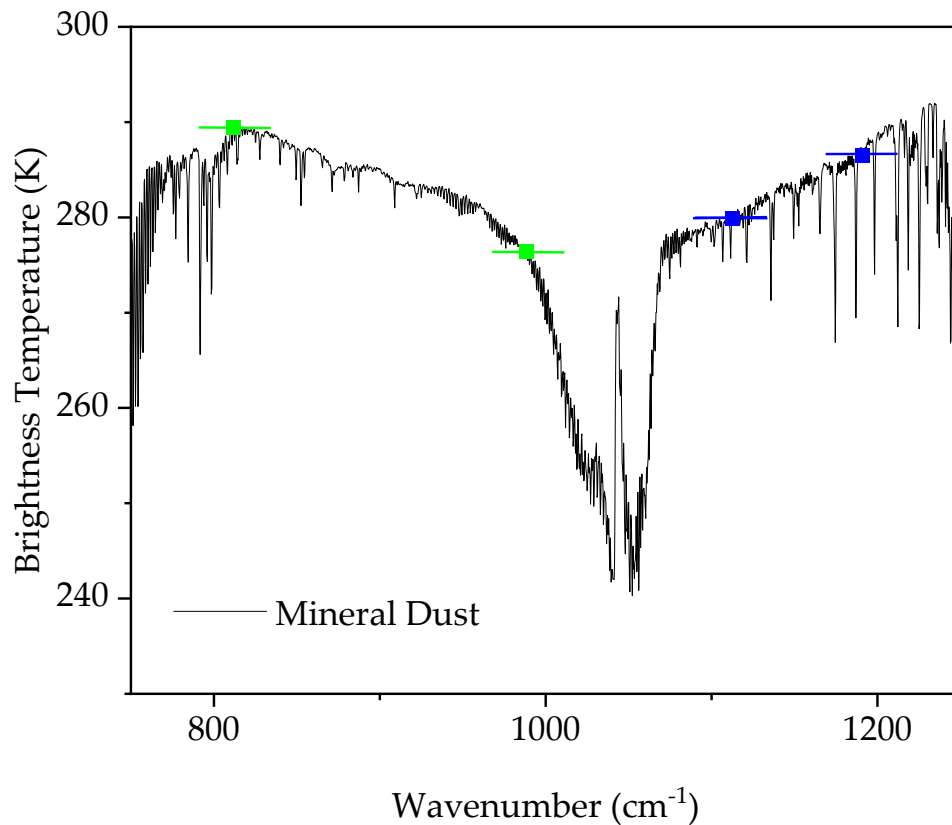
Figure 43 IASI dust example from Gobi Desert in 3 May 2017 showing spectral position of IASI channels for ΔT_{B1} (in green) and ΔT_{B2} (in blue) computations used in this study to select dust spectra.

Dust selection can be erroneous without properly accounting for the LSE in the RTE equation: the mineral dust 'V-shape' can be more likely to be inclined due to the surface signal, especially in the band where the Reststrahlen region is present (between 1069 and 1250 cm$^{-1)}$. **Figure 44a** shows the IASI dust selection (ΔT_{B1} and ΔT_{B2}) during a Gobi dust storm on the 4 May 2017 at 3:00 UTC; however, to visualize and study the surface effect, only ΔT_{B2} is illustrated. False dust detections are identified by a dashed black circle

where MODIS shows over the same region a negligible daily average AOD (**Figure 44b**). The false detection and selection from the IASI spectra are related to the LSE constraints.
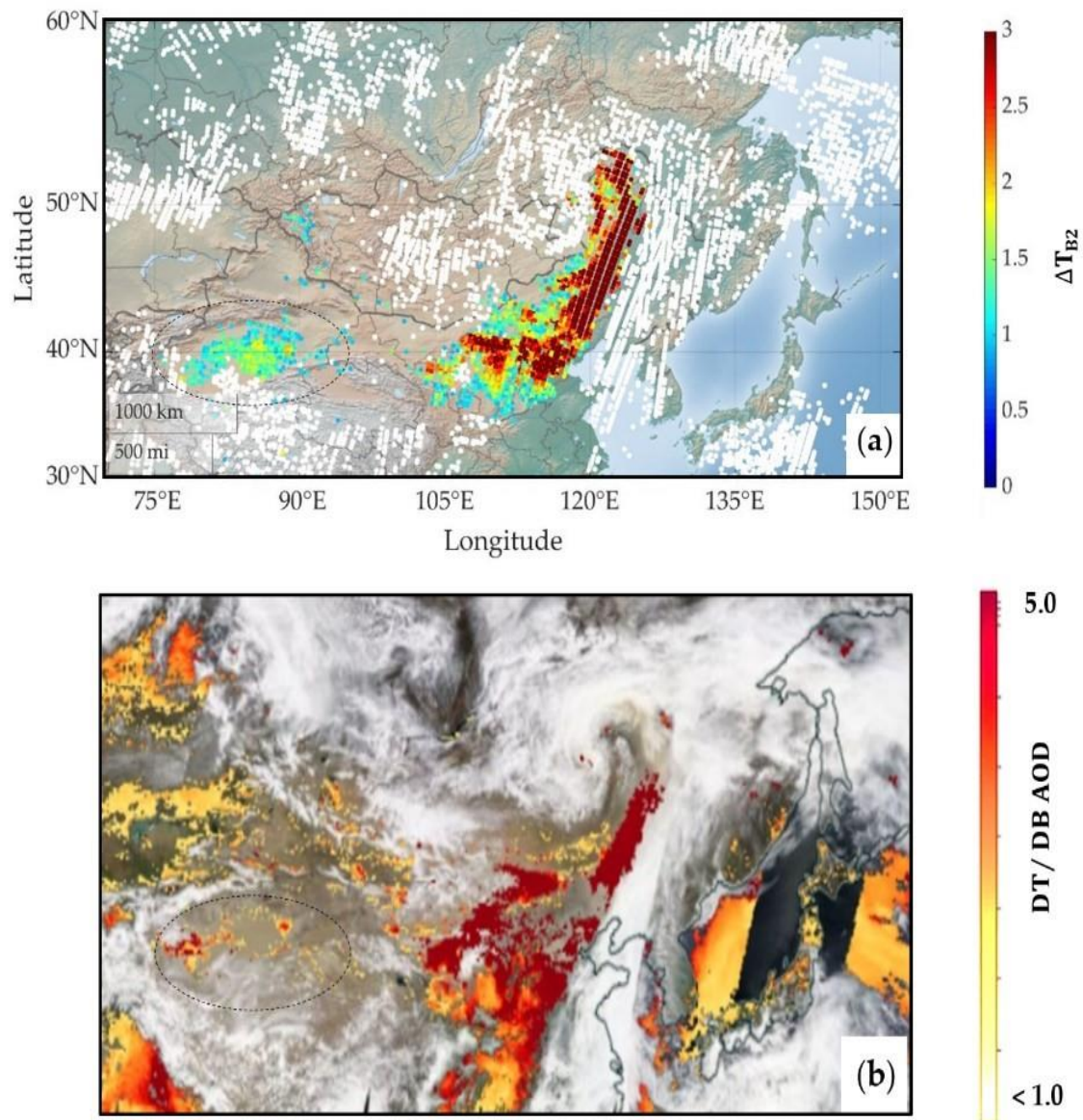
Figure 44 (a) Difference in the brightness temperature ΔT_{B2} of the IASI dust selection during the dust storm on 4 May 2017 by day; **(b)** merged dark target/deep blue aerosol optical depth from MODIS/Terra on 4 May 2017 (https://worldview.earthdata.nasa.gov, last accessed on 1 December 2021). The dashed black circle region presents the false aerosol detection region.

To solve the problem of the emissivity signal, many studies have used for their aerosols and gases retrievals, an IASI mean monthly emissivity dataset provided by *D. Zhou et al. (2014)* with 0.25° × 0.25° latitude–longitude grids (Bauduin et al., 2017; Clarisse et al., 2019; Piontek et al., 2021). The climatology is produced with an algorithm that retrieves the surface emissivity products from the IASI by comparing and validating them

with independent in situ and satellite measurements *(Zhou et al., 2009, 2011, 2012)*. **Figure 45** shows the example of four types of surfaces in East Asia: the Gobi and Taklamakan Deserts, vegetation in the eastern regions, and urban and populated cities in Shandong. The LSE spectral variability is low at the Sea of Japan and Shandong *(Zhou et al., 2014)*. Notably, the surface composition is rich in quartz in the Taklamakan and Gobi Deserts, showing high LSE spectral variability between 1069 and 1250 cm^{-1}, with a characteristic peak at 1159 cm^{-1}, which is identical to the spectral desert detection from the IASI illustrated in **Figure 41**.
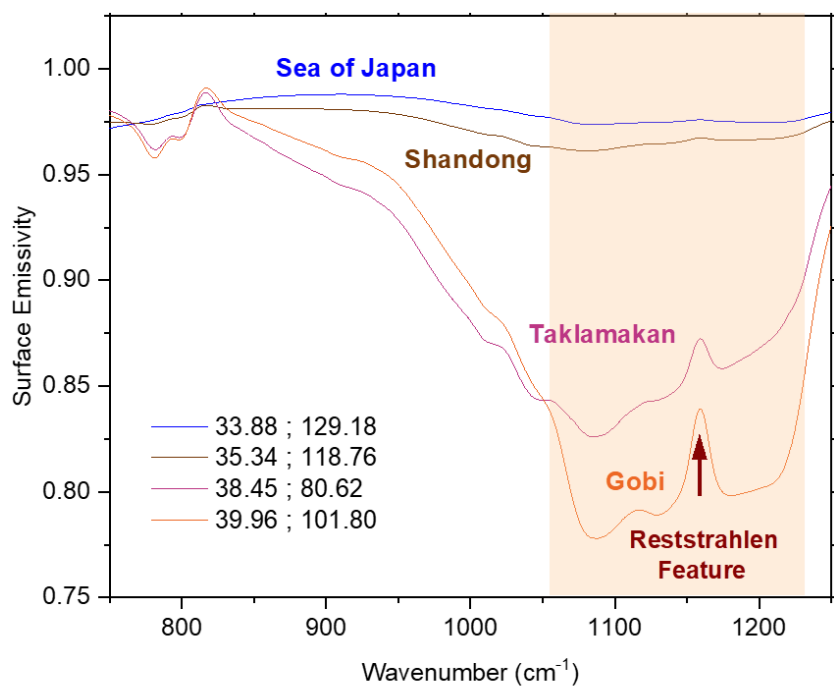
Figure 45 Mean monthly surface emissivity of four different surfaces of (latitude ; longitude) during the month of May *(Zhou et al., 2014)*.The shaded orange box indicates the Reststrahlen region.

The direct use of these fixed climatology can underestimate or overestimate the spectral observation due to the LSE variability caused by diurnal and seasonal cycles, satellite viewing angles, or surface-type variation *(Huang et al., 2016)*. An example is provided in **Figure 46**, the IASI spectral radiance in green of a scene above desert is directly divided by the corresponding climatology LSE pixel. It gives an excessive correction of a desert spectrum, where the brightness temperature in green is strongly altered after applying the correction at 1059 cm^{-1}, with its neighboring gap displayed, and the brightness temperature between 1069 and 1250 cm^{-1} highly exceeds that of a flat clear sky detection. This result indicates that the direct use of the climatology can alter the spectral radiance

signature and falsify the atmospheric information in question. Hence, the optimization of the LSE climatology is crucial to finding an optimal aerosol quantification. As a result, establishing the surface contribution and removing it from satellite observations remain challenging.
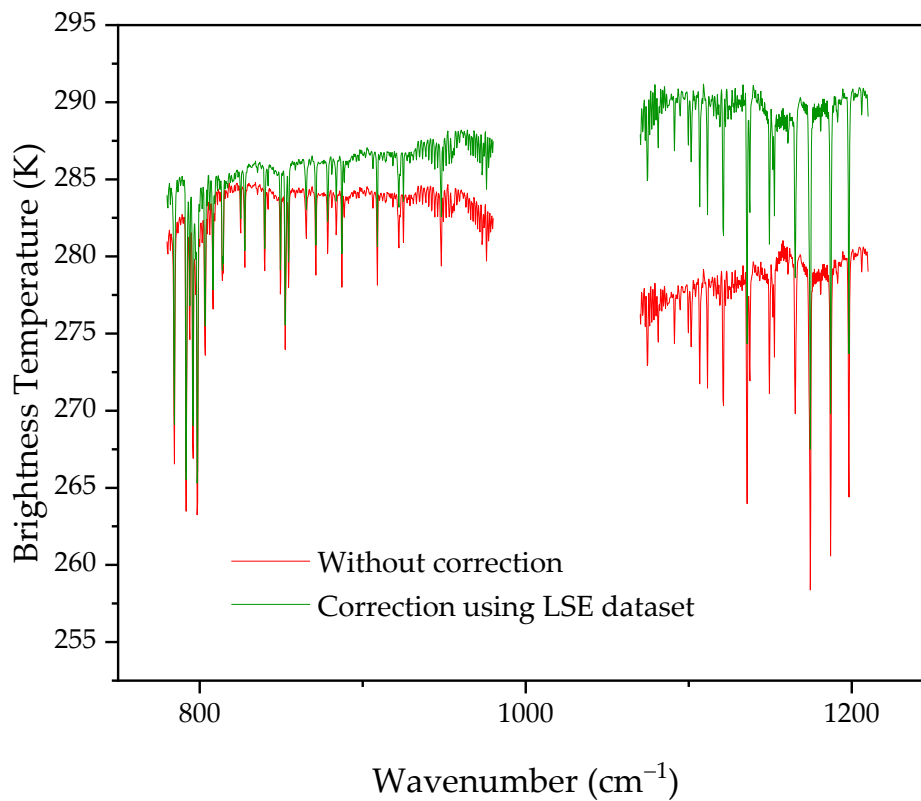
Figure 46 Brightness temperature Gobi Desert spectrum example from 3 May 2017 before and after the LSE correction using a monthly average emissivity value *(D. Zhou et al., 2014)*. For simplicity, the carbon dioxide, ozone, and water vapor wide bands are removed from the IASI spectra in the rest of the of the chapter.

2.3.2 The LSE Optimization Method

In a first step, IASI pixels are classified into different types (clear sky, aerosols and cloud), we consider only pixel that have 90 % of homogeneity in detection. Then, the pixels are filtered using a principal component analysis (PCA) code developed in Laboratoire d'Optique Atmosphérique (LOA) *(Herbin, 2017)*. An example is shown in **Figure 47a** for IASI detection, where clouds (in gray) mixed with the dust plume and separated the detection into four different parts. IASI detection and selection are consistent with the RGB image in **Figure 47b** showing geostationary HIMAWARI 8 RGB imagery, where

thin high clouds (in olive color) mix with the plume dividing it into four different aerosol sections (in pink). The IASI map with a Mercator projection shows homogeneous cloud and aerosol selection with the same morphology but with a different projection than the HIMAWARI 8 imagery having a polar projection. The inverted 'L-shape' cloud selection from the IASI map has the same shape in the imagery but is elongated. This comparison indicates the consistency of the IASI cloud and the dust selections.
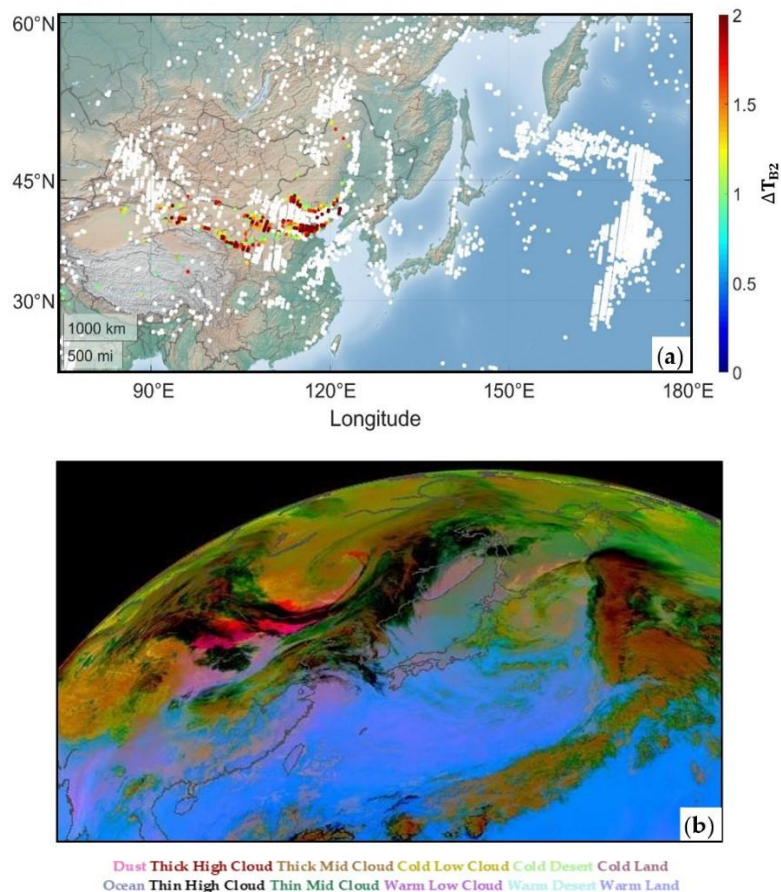
Figure 47 (a) IASI dust and cloud selection on 15 March 2021; **(b)** RGB Dust False-like SEVIRI from HIMAWARI (www.icare.univ-lille.fr, last accessed on 1 December 2021).

The intensity of the Reststrahlen feature is proportional to the particle size *(Simms et al., 2009)*. Based on this, the Reststrahlen feature can be used as a surface effect indicator; it is highly displayed on desert surface detections compared to airborne dust. After classification, to optimize the LSE effect on IASI radiances, a new methodology was developed by calculating the Reststrahlen relative value $X_{m(v)}$ of a spectrum $m(v)$ for both the IASI spectral radiance and the mean monthly emissivity value at the same pixel (Note

that this value does not correspond to the CRI parameter defined in **Chapter I**). The method expresses the relative value between the observed spectrum with the Reststrahlen effect $m_{w/}(v_R)$ at the Reststrahlen wavenumber v_R = 1159 cm^{-1} and the expected value of the observation spectrum without the Reststrahlen effect $m_{w/o}(v_R)$, and it is written as follows:

$$X_{m(v_R)} = \frac{m_{w/}(v_R) - m_{w/o}(v_R)}{m_{w/o}(v_R)} \textbf{ (19)}$$

where $m_{w/o}(v_R)$ is computed by solving a linear function of the form $y = ax + b$ calculated in the neighboring Reststrahlen feature with choosing channels not affected by the narrow gas bands (**Figure 48**).
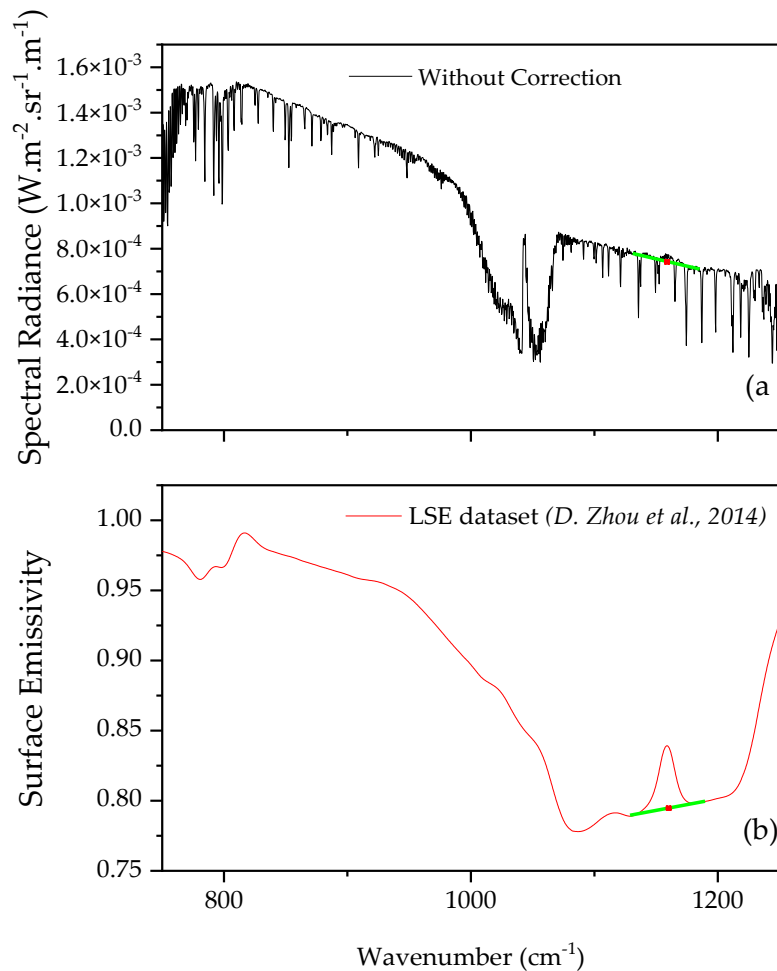
Figure 48 Example of an IASI **(a):** spectral radiance and; **(b)** its corresponding surface emissivity from *D. Zhou et al., 2014* with the calculated linear equation in the neighboring of v_R (in green) and the value of $m_{w/o}(v_R)$ for each spectrum (red point).

Then, we define the emissivity correction factor C as follows:

$$C = \frac{X_{R(v_R)}}{X_{\varepsilon(v_R)}} \ (20)$$

with C being the ratio between the Reststrahlen relative value for the spectral radiance detection $X_{R(v_R)}$ and the Reststrahlen relative value for the mean monthly emissivity spectrum $X_{\varepsilon(v_R)}$ for the same detected grid, both calculated by **Equation** (**19**).

The corrected surface emissivity $\varepsilon_C(v)$ is estimated from the mean monthly surface emissivity $\bar{\varepsilon}(v)$ and the correction factor C, and it is written as follows:

$$\varepsilon_C(v) = 1 + C(\bar{\varepsilon}(v) - 1) \quad (21)$$

The correction in **Equation** (**21**) is calculated when a significant Reststrahlen effect is present. For this, a minimum condition is applied to the $m_{w/}(v_R) - m_{w/o}(v_R)$ value of both the radiance and emissivity spectra. A limit case occurs when the surface is masked and no emissivity correction is taken into consideration, the detections can be concentrated dust layers and opaque clouds. The correction factor C is 0; hence, the corrected surface emissivity ε_C is 1. The saturated spectra are characterized by having a CO_2 a higher brightness temperature peak at 668 cm^{-1} than the brightness temperature O_3 peak at 1044 cm^{-1} (**Figure 49**). On the other hand, when the LSE variability is small, the Reststrahlen wavenumber $\bar{\varepsilon}(v_R)$ approaches 1. In this case, the correction factor C equals 1, and the literature dataset is directly used ($\varepsilon_C(v) = \bar{\varepsilon}(v)$). Finally, if there is a minimal sensitivity from the IASI radiance and the climatology $\bar{\varepsilon}(v_R)$ on the Reststrahlen characteristic, the correction factor C is also 0.

After solving **Equation (21)** to obtain the corrected emissivity $\varepsilon_C(v)$, the corrected spectral radiance $R_c(v)$ is calculated dividing the observed spectral radiance $R(v)$ by corrected emissivity $\varepsilon_C(v)$. The dust spectra are then selected by converting the radiance to the brightness temperature $T_{Bc}(v)$ following **Equation (17)**, then conditions were applied on ΔT_{B1} and ΔT_{B2} as discussed in **Section 2.3.1**. **Figure 50** illustrates the flowchart of the optimization method described.
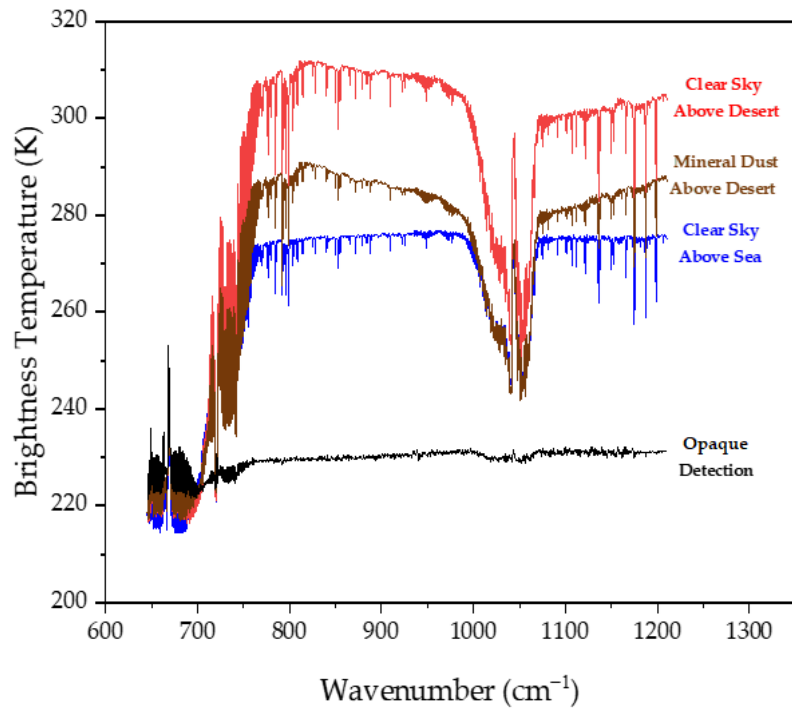
Figure 49 IASI spectral examples showing a CO_2 peak at 668 cm^{-1} higher than the O_3 peak at 1044 cm^{-1} exceptionally for an opaque detection.
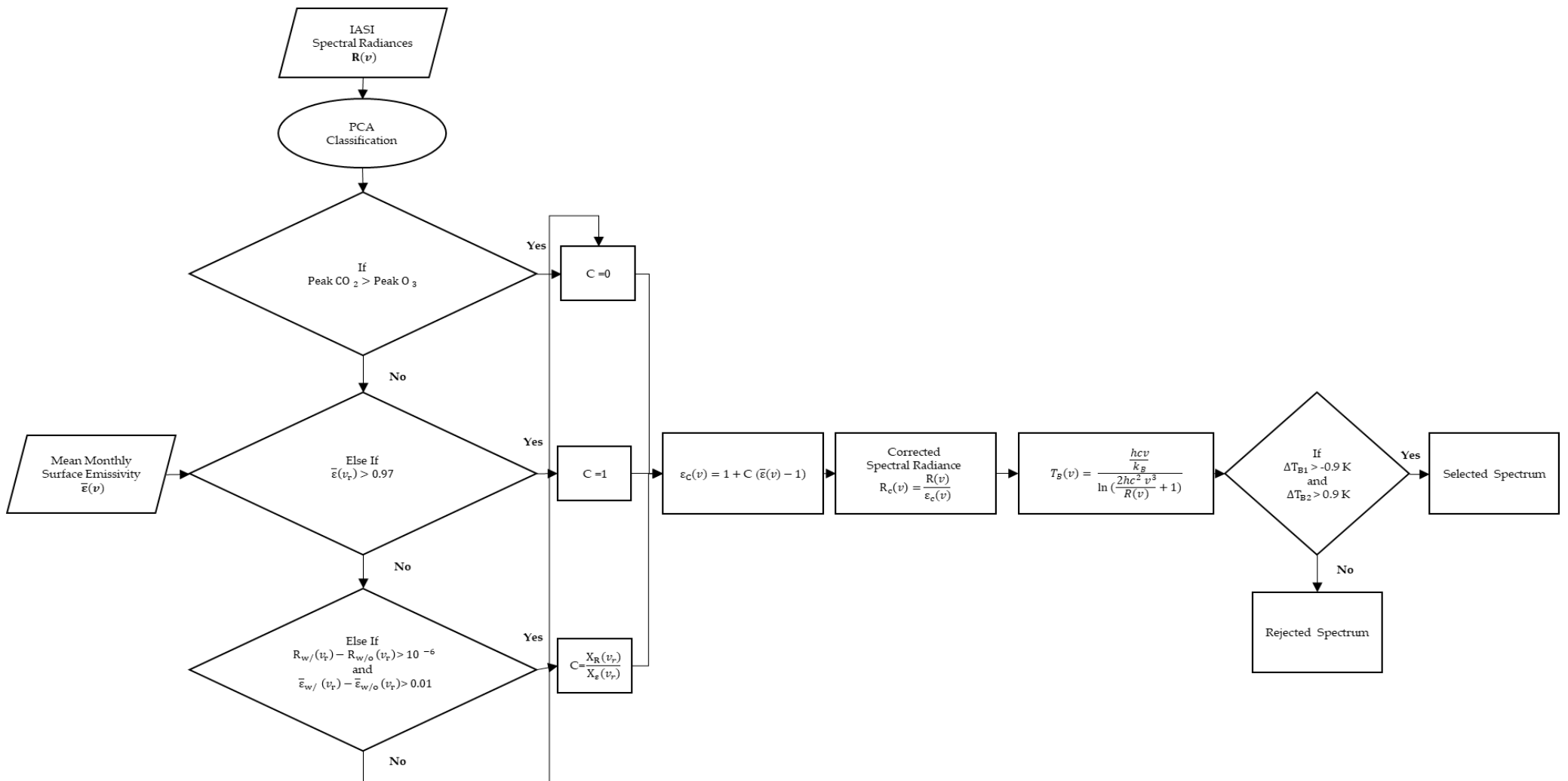
Figure 50 LSE correction scheme diagram.

The correction method is for illustration applied to two IASI observations shown in **Figure 51**, detections of a clear sky above the desert (in red) and a mineral dust (in gray). By applying the LSE method, the effects dominated by the Reststrahlen phenomenon where removed from the first spectrum (corrected spectrum in green) as if a clear sky above the sea (in blue) was detected after the correction. The peak at 1059 cm⁻¹ was minimized and the lower shift between 1069 and 1250 cm⁻¹ was flattened. In contrast, the modification of the second spectrum (in black) was minimal, maintaining the dust spectrum and its 'V-shape' signature. In both cases, only the base line and the Reststrahlen feature were altered and the gases narrow bands remain unchanged.
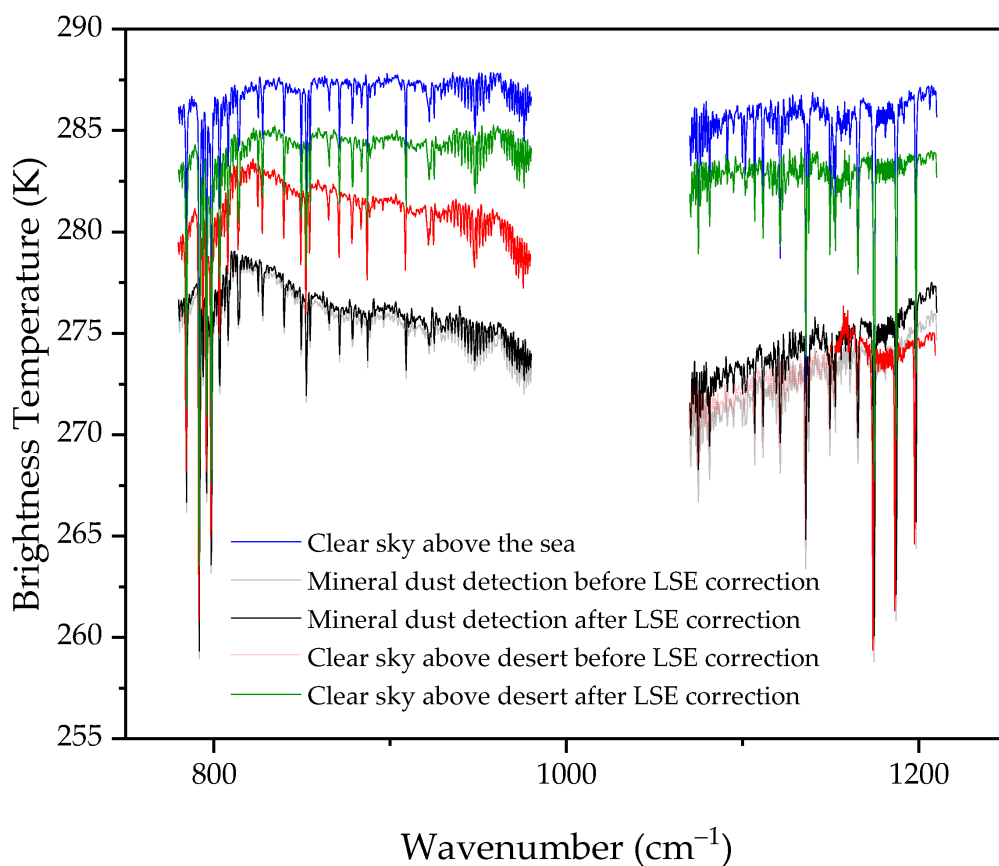
Figure 51 IASI spectral detection example for a clear sky above the sea compared to a clear sky above the desert and mineral dust detection from the 3 May 2017 dust event before and after LSE optimization.

Results indicate that the LSE method corrects the IASI spectra and differentiates between surface and mineral dust detections. In the first case, it removes the surface signal and in the second case it corrects the spectrum without removing dust features. To better understand the LSE method's effect, we derive the IASI optical thickness from the spectral

radiance. This parameter gives us information about the dust layer extinction, layer thickness, and dust microphysical properties.

Infrared retrievals neglect atmospheric effects and aerosol scattering *(Ackerman, 1997)*. In addition, if the aerosol layer is optically thin, the surface emission term is the primary contributor to the measured radiance and the radiative transfer equation of the **Equation (15)** can be approximated as:

$$R(v) = \varepsilon(v)B(v,T)e^{-\int_0^H k(v,h)dh} \textbf{ (22)}$$

where the spectrum $R(v)$ is a function of the surface emissivity $\varepsilon(v)$, the surface temperature T_s described by the Planck function $B(v,T)$, and the total extinction k_v of the altitude of the top atmosphere H, containing gases, aerosols, and clouds.

Consider a homogeneous and stratified dust layer of thickness L. Hence, we can apply Lambert–Beer's law. For an incident spectral radiance $R_0(v)$ at wavenumber v, the attenuated amount of $R_{obs}(v)$ passing through a dust layer of thickness L has an extinction coefficient $k_{ext}^{aerosol}(v)$ resulting from the absorption and scattering (**Figure 52**), and **Equation (22)** can be written as follows:

$$R_{obs}(v) = R_0(v)e^{-k_{ext}^{aerosol}(v)L} \textbf{ (23)}$$

The incident spectral radiance $R_0(v)$ represents a clear sky spectrum above the sea where $R_0(v) \geq R_{obs}(v)$. The same clear sky spectrum is used as a reference to IASI observations studied. This spectrum is selected from the first date of a dust event with the nearest sea location to the dust source, and fixed during the following dates of the storm. The purpose is to obtain a relative optical thickness to disregard the variation in the temperature from observation to another.
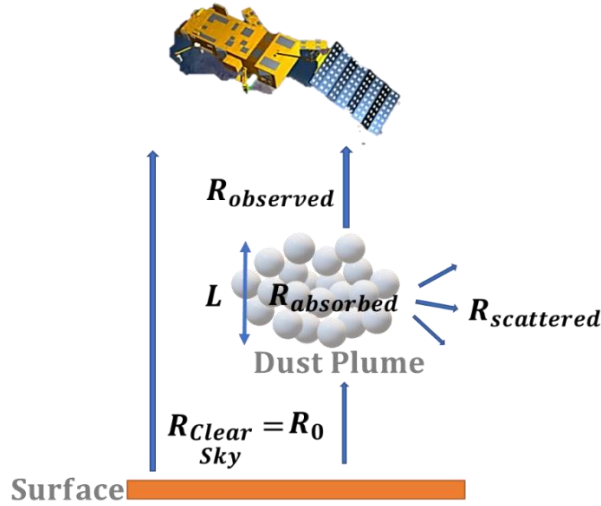
Figure 52 Lambert-Beer's law application on a dust plume detected by IASI/MetOp

From IASI radiances, we can calculate an equivalent optical thickness $\tau(v)$ *(Klüser et al., 2015)*. It is obtained by the natural logarithm of the ratio of a clear sky spectral radiance $R_0(v)$ and a spectral radiance observation $R_{obs}(v)$:

$$\tau(v) = ln\left(\frac{R_0(v)}{R_{obs}(v)}\right) \textbf{(24)}$$

This ratio becomes independent from the Planck function $B(v, T)$ by subtracting it in the calculation, and unconstrained by the surface emissivity after applying the LSE optimization method discussed above. What remains in the equation is the aerosol extinction multiplied by the layer thickness L with an error ϵ_τ, which includes noise and the remaining residue of gas present in the spectrum. Thus, **Equation (24)** is written as follows:

$$\tau(v) = ln\left(\frac{e^{-k_{ext}^{gases}(v).H}}{e^{-k_{ext}^{gases}(v).H - k_{ext}^{aerosol}(v).L}}\right) = k_{ext}^{aerosol}(v)L + \epsilon_\tau \textbf{ (25)}$$

Equation (25) was applied to the example spectra shown in **Figure 53**. Before the LSE correction of the clear sky detection above the desert, an apparent optical thickness has an extinction coefficient caused by a land surface, e.g., a sand surface contaminated by the Reststrahlen effect (**Figure 53a**). After the LSE correction, the apparent optical thickness approaches zero with no aerosol features. This indicates that the spectral signal

comes entirely from the land surface. However, a minor optimization affected the optical thickness of the mineral dust detection above the desert (**Figure 53b**) with an aerosol extinction signal remaining. This result verifies that the LSE optimization method corrected only land surface signals without removing the aerosol fingerprints that present crucial data to quantify the aerosol physico-chemical properties.
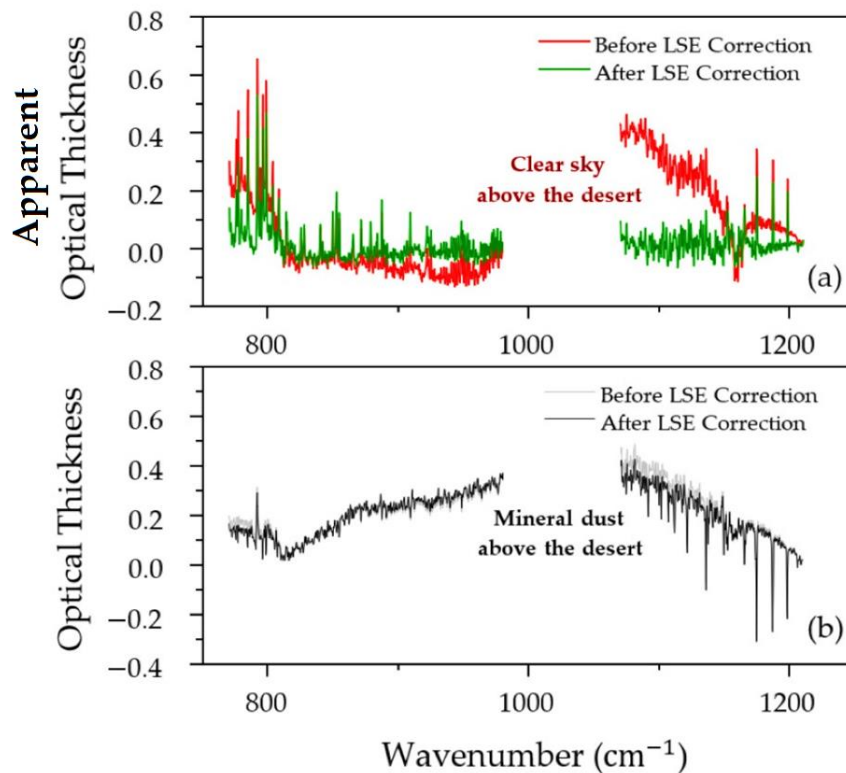
Figure 53 Example of **(a)** the apparent optical thickness spectrum of a clear sky above the desert and **(b)** the equivalent optical thickness of mineral dust above the Gobi Desert from the 3 May 2017 dust event before and after LSE correction.

The methodology was also tested on more extreme cases using to the same detection example of the 2017 dust storm on 4 May previously presented in **Figure 44a,** before LSE correction. The result is plotted in **Figure 54a,** after LSE correction. The erroneous detection above the Taklamakan desert is eliminated and a minor change can be seen in the dust plume that originated from the Gobi Desert. The dust detection after LSE optimization and is compared to CALIOP-attenuated backscattering at 532 nm in **Figure 54b**. A

thick aerosol layer was detected in the low troposphere between 1 and 3 km. Hence, the optimized LSE correction and dust detection haven't removed dust signal. Therefore, by using the new LSE method, dust selection was tested for all situations considering cloud detection.
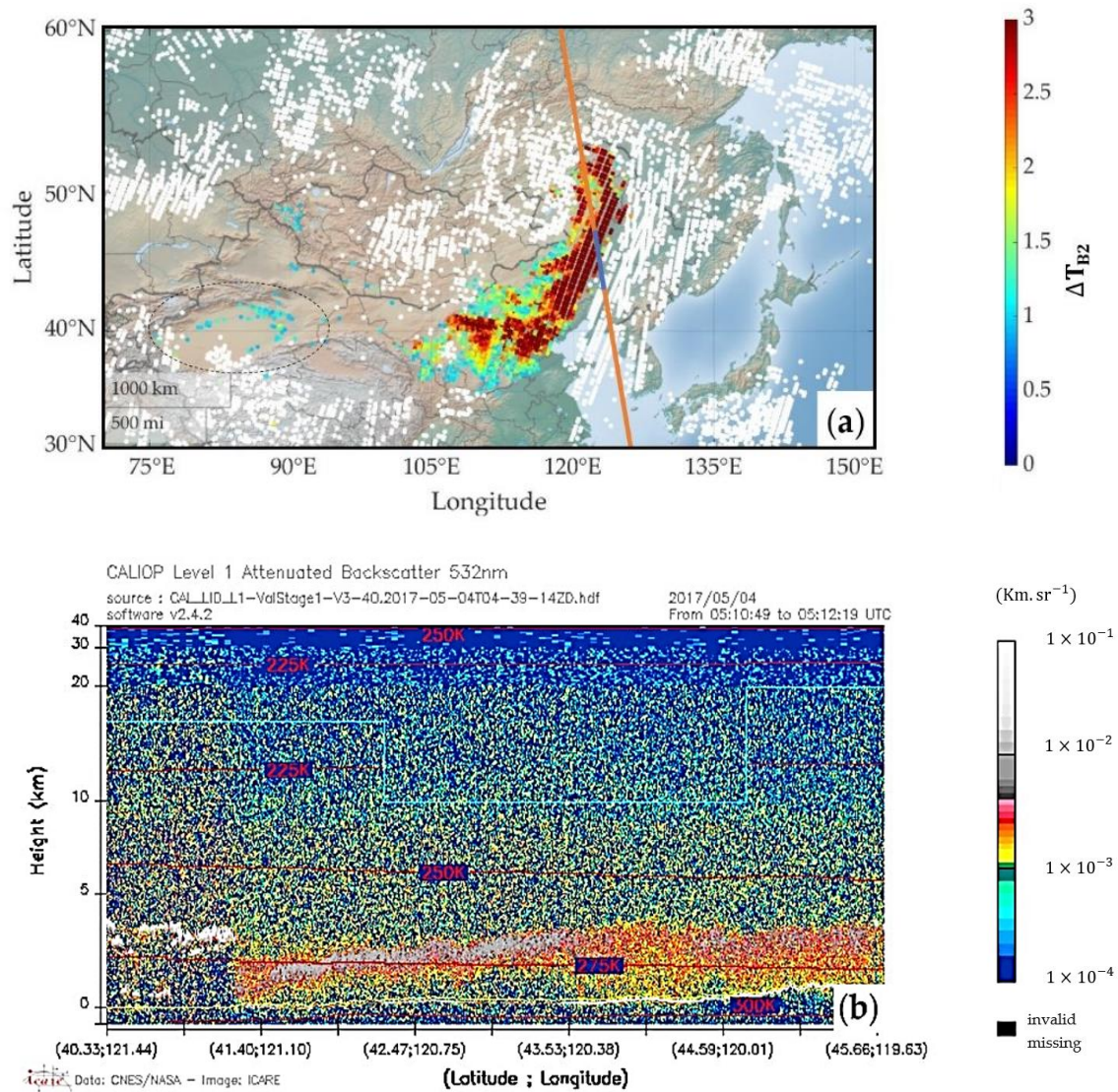
Figure 54 (a) The difference in the brightness temperature of the IASI dust selection after LSE correction during the dust storm on the 4 May 2017 at daytime, with clouds selection (white pixels). The dashed black circles present the minimized false aerosol detection region. The orange line is the CALIOP orbit track and the blue line is the CALIOP viewing section; **(b)** CALIOP-attenuated backscatter at 532 nm (www.icare.univ-lille.fr, accessed on 27 November 2021).

Conclusion

The IASI instrument detects different atmospheric components with a high spectral resolution: gas, airborne dust, and clouds depending on their optical layer thickness. However, the LSE can affect detections above land, especially desert surfaces, causing false mineral dust detections with surface detections and affecting quantified parameters. Previous uses of an LSE monthly dataset from IASI show under-estimation or over-estimation of LSE signal due to the LSE's temporal variability. A new LSE method was developed and used to optimize the use of these datasets. The surface effect was minimized from a clear sky detection above the desert and a mineral dust detection. In addition, the IASI optical thickness was derived to verify the optimization that allowed the total removal of the surface features without removing dust signatures. The method applied on a case study on 4 May 2017 removed the selection of false aerosol detections above the Taklamakan Desert. Results were compared to MODIS and CALIOP for validation. Finally, the LSE optimization is a crucial step toward characterizing the dust's physico-chemical properties.

CHAPTER III. AEROSOL COMPOSITION RETRIEVAL

In this chapter, we introduce different mineral groups and previous mineralogical studies. Then, we present new experimental optical properties (i.e., the extinction coefficient spectra) measured using laboratory FTIR spectra for Gobi dust and pure minerals (quartz, illite, and calcite). An effective extinction coefficient is simulated using a linear combination of the pure mineral extinctions spectra to reproduce the Gobi dust spectrum and IASI dust detections. Then, laboratory measurements are compared to the IASI optical thickness, showing the same molecular features. Finally, we couple the IASI optical thickness with a linear combination of pure mineral spectra to compute the mineralogical dust mass weights. In addition, we apply the method to a dust storm that occurred between 3 and 7 May 2017 using IASI observations based on METOP-A and the results are compared with a second dust event between 14 and 22 March 2021 and METOP B. Finally, we compute the forward model to obtain an a priori on the SD, which will be used in the future to solve the inverse problem.

3.1 EXPERIMENTAL LABORATORY DATA

3.1.1 Dust Mineralogy

Mineral dust is composed of silicates, carbonates, and oxides forming the Earth's crustal components from which pure minerals can be divided into different groups based on their structure. Hence, we can distinguish:

1- *Phyllosilicates* (e.g., illite, kaolinite, chlorite and smectite) are formed of sheets of tetrahedra silicates. They are abundant in clay-sized dust (discussed in **Section 1.3.1**) and hence termed "clay minerals", while chlorite is the only specie that can be found in both clay and silt particles *(Griffin et al., 1968)*.
2- *Tectosilicates* (e.g., quartz and feldspars) have an interlocking tetrahedra structure. They are minor in clay-sized particles and major in silt fraction since they have strong covalent bonds hard enough to be broken by wind erosion. They form 75% of the Earth's crust.
3- *Carbonates* (e.g., calcite and dolomite) are found in both clay *(Abtahi, 1980)* and silt particles.
4- *Minor minerals* include iron oxides (e.g., goethite and hematite) and sulfates (e.g., gypsum) mostly present in clay-sized fractions.

Until now, information about dust mineralogy on large spatial scale is still limited. Due to the lack of airborne dust composition, *Journet et al., 2014* used an indirect approach to obtain dust mineralogy on a global scale. The study estimated the global soil mineralogy from 211 soil units. The average mineralogy for the clay and silt fractions from surface topsoil from seven continental dust sources. A general circulation model was used with an aerosol scheme (LMDZ-INCA) for dust emission and transport. The study found that phyllosilicates dominate the clay-sized particles with averages between 63-71%; tectosilicates presented only 3-5 %, while carbonates are between 6-9%. Whereas the silt-sized are most abundant with tectosilicates and carbonates, no

percentages were given since there is less information available for silt fractions. The airborne dust and parent soil fractions were compared, showing a different composition.

On a regional scale, East Asia is known to have a variable regional mineralogical composition, as it depends on the geomorphology and the soil composition. Three broad types of dust sources were identified in East Asia *(Xuan and Sokolik, 2002)*. Type I deserts are located in topographic lows, such as the Taklamakan desert; these deserts are associated with fluvial fans *(Ginoux et al., 2012)*. Type II deserts are located on the plateau, with natural dust sources coming from the Gobi Desert of Inner Mongolia. Type III deserts are in dry agricultural areas, e.g., the Horqin Sandy Land, which was shown to have a particular influence on some desert storms *(Minamoto et al., 2018)*. **Figure 55** displays the mineralogical composition data from literature of the three regions I, II and III. We collected mineralogical literature data of the three dust sources: Taklamakan Desert *(Di Biagio et al., 2014)*, Gobi Desert *(Wang, 2019)* and Horqin Sandy land *(Shen et al., 2009)*. The first was derived from Fourier transform infrared spectrometry while the others used XRD method to measure the mineralogical composition collected dust samples. The dust is highly rich in phyllosilicates in all regions. From West to East Asia, the carbonate soil content decreases and the feldspar content increases. Hence, the diversity in the dust constituents allow to trace dust sources. For instance, a study used experimental methods, i.e., geochemical tracing methods, to link dust mineralogy and sources depending on the geology *(Chen and Li, 2011)*. SEM method was also employed to exploit the quartz and illite/quartz ratio contents and link them to particle size distribution *(Shao et al., 2007)*.
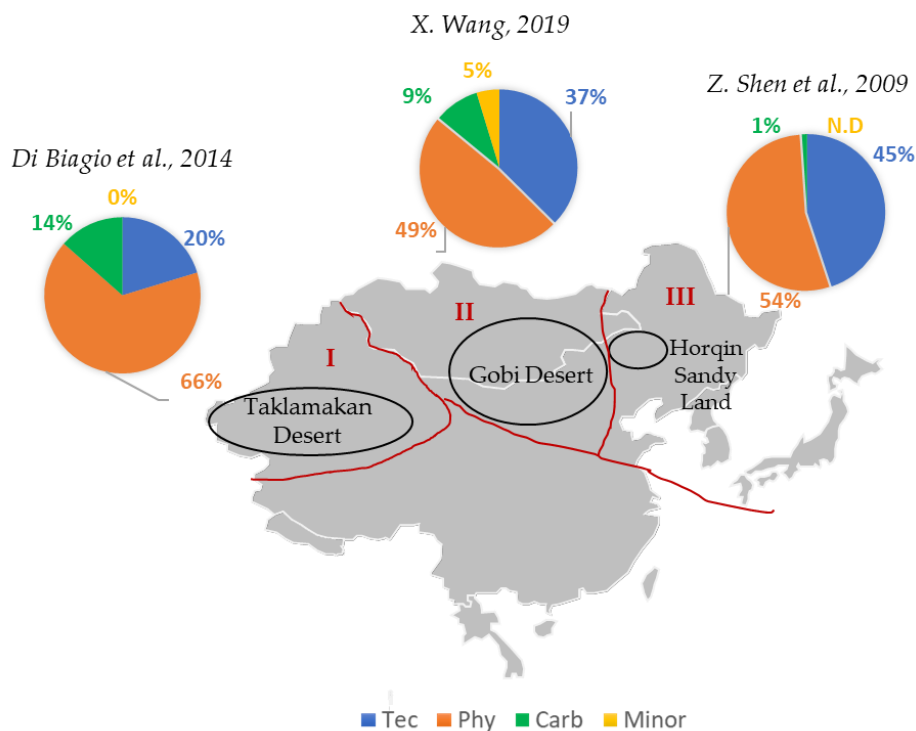
Figure 55 Mineralogical composition (percent of mass weights) from literature data of three major desert sources (black) in three region types (red). Tec: Tectosilicates, Phy: Phyllosilicates, Carb: Carbonates, N.D: Non-determined data.

The quantification of the dust mineralogy remains complex and limited due to the dependency on the particle size fraction and the dust sources, the aeolian transport and mixing, and the aging processes that alter the physic-chemical properties of dust. Moreover, investigating dust mineralogy is still challenging from satellite instruments. It may be due to the challenges posed by the LSE contribution to the measured radiance and the lack of adequate experimental optical properties (i.e., CRI) crucial in aerosol retrievals. The first limitation was overpassed after applying an LSE correction method fully described in **Chapter II**. The second urges us to measure the optical properties experimentally to be applied to the IASI spectra, as it will be discussed in the next section.

3.1.2 Gobi Dust Optical Properties

Laboratory Measurements

The laboratory setup and experimental procedure are described in detail in the references *(Herbin et al., 2017; Hubert et al., 2017)*, and are only summarized herein. The experimental study was performed by two laboratories: PhysicoChimie des Processus de Combustion et de l'Atmosphère (PC2A) and Laboratoire d'Optique Atmosphérique (LOA). *Deschutter, 2022* analyzed samples of pure quartz crystal, pure amorphous illite, and pure calcite crystal, in addition to Gobi dust samples that were collected in Yanchi, Ningxia province in China (107.475211°E,36.487333°N) *(Romanias et al., 2016)*. Sample particles (around 5 g of mass) were placed in suspension by maintaining mechanical agitation using a magnetic stirrer as illustrated in **Figure 56.** Using a mass flow controller set at 2 $L. \min^{-1}$, the particles were carried by pure nitrogen gas into a buffer volume to ensure homogeneous aerosol flow and then into two consecutive spectrometer setups. The first was a Fourier transform infrared spectrometer with a 10 m multipass cell, which measured the extinction coefficient in the spectral range between 650 and 9000 cm^{-1}. The second was a UV-visible spectrometer with a 1 m cell measuring extinction coefficients between 10,000 and 40,000 cm^{-1}. In this study, we are interested in the spectral range between 750 and 1250 cm^{-1} (in the atmospheric window) corresponding to the aerosol detection. At the exit of the cell, a scanning mobility particle sizer (SMPS) and an aerodynamic particle sizer (APS) were simultaneously used to record the size distribution generated by the apparatus between 10 nm and 20 μm. Results of Gobi dust had an average geometric size diameter of 0.5 μm with a standard deviation of 1.95 μm.
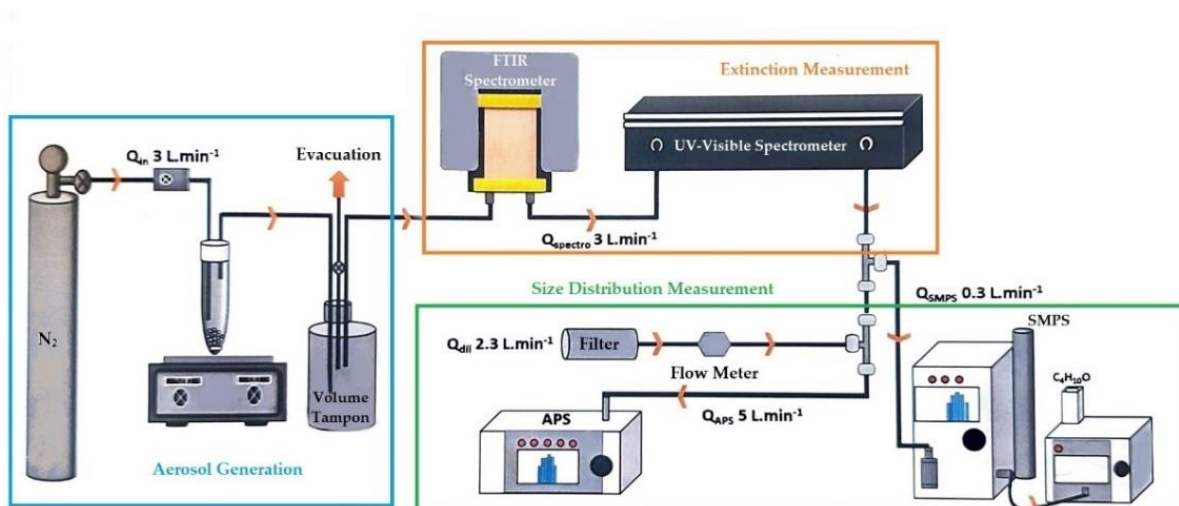
Figure 56 Experimental apparatus parts: aerosol generation, extinction measurement, and size distribution measurement (Reproduced from *Deschutter, 2022*).

Molecular Features

Figure 57a shows the measured extinction coefficient of the Gobi dust sample**.** The absorption peaks are identical to the peaks of the pure mineral extinction coefficients (quartz, illite, and calcite), as illustrated in **Figure 57b**, which are normalized to remove the dependency on concentration. These measurements are in agreement with the mineralogy in the literature, where mineral fingerprints show the presence of the three mineral families: tectosilicates, phyllosilicates, and carbonates, with the presence of quartz, illite, and calcite from each group, respectively.
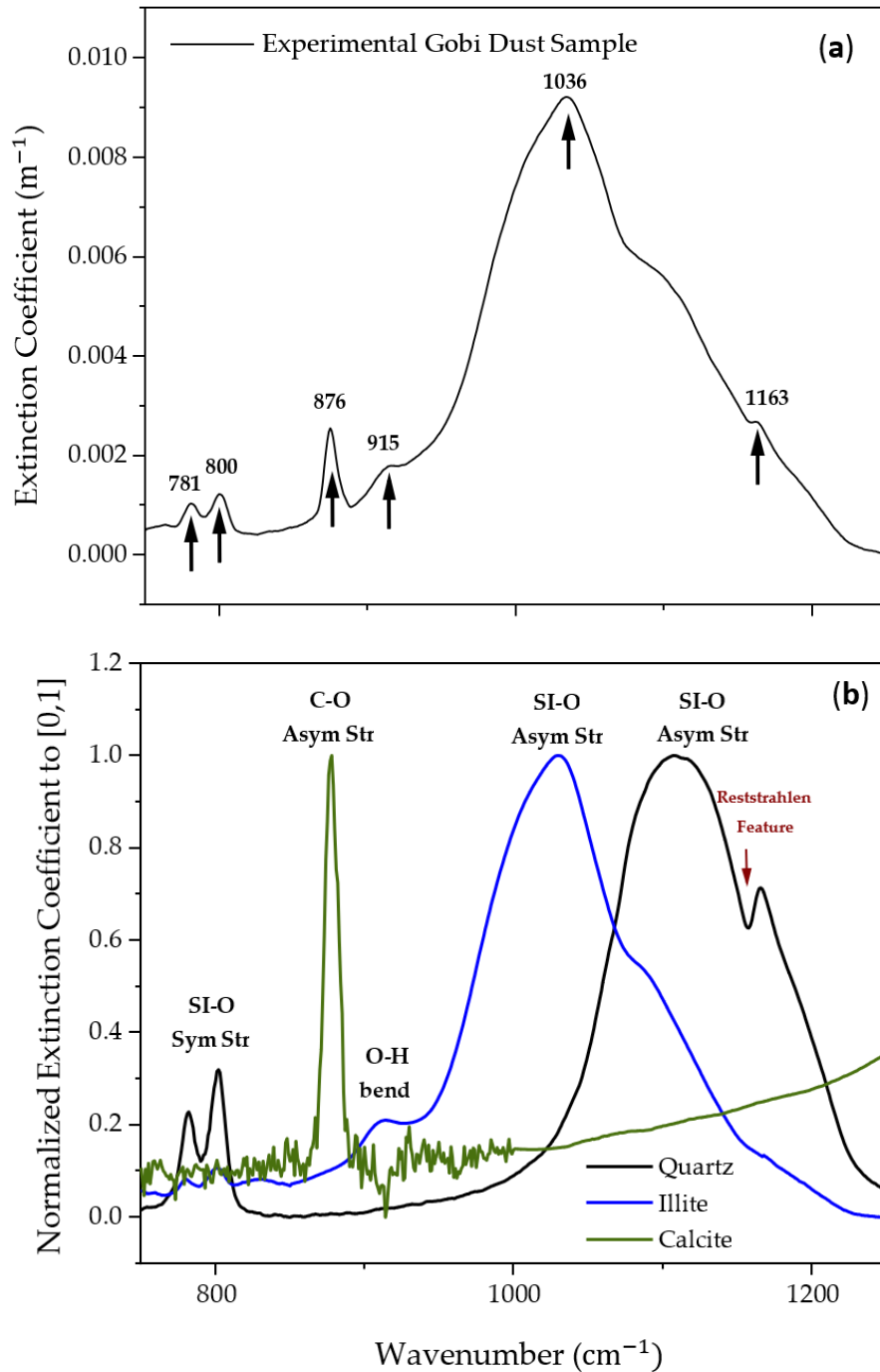
Figure 57 Laboratory extinction coefficient by Fourier Transform infrared spectrometer of (**a**) Gobi dust samples, with arrows indicating extinction peaks, and (**b**) normalized extinction coefficient to [0, 1] of the pure minerals quartz, illite, and calcite with their molecular assignments *(Deschutter, 2022)*. Sym Str: symmetrical stretching; Asym Str: asymmetrical stretching; Bend: bending.

The most intense bands for quartz from the tectosilicates group are between 1080 and 1177 cm^{-1}, generated by Si-O asymmetrical stretching. The Si-O symmetrical stretching produces a doublet at 778 and 795 cm^{-1} *(Reig et al., 2002; Spitzer and Kleinman, 1961)*. This doublet caused by the same Si-O stretching is also found in phyllosilicates or clay minerals (e.g., illite, kaolinite...) *(Madejova and Komadel, 2001)*. The major peak present in the latter group at 1033 cm^{-1} is due to the Si-O asymmetrical stretching. This shift difference with respect to the stretching mode in quartz is explained by cation substitutions, particularly Al^{2+} for Si^{2+}. The shoulder at 916 cm^{-1} for illite is assigned to the -O-H bending associated with Al, Fe, or Mg cations *(Madejová et al., 2017)*. The fundamental vibrations of CO$_3$ anions in carbonates (e.g., calcite, dolomite, etc.) show a spectral feature at 885 cm^{-1} of carbonates in Thermal InfraRed (TIR) caused by C-O asymmetrical stretching *(Bishop et al., 2021; Green and Schodlok, 2016)*. **Table 2** summarizes the molecular assignments in the TIR active modes of the abundant minerals of the three main mineral groups in desert dust from previous studies.

Table 2 Molecular assignments of some minerals in TIR.

Mineral Group	Mineral Name	Molecular Assignment	Central Wavenumber (cm^{-1})	References
Tectosilicates	Quartz	Si-O Symmetrical Stretching	778, 795	*(He et al., 2019; Reig et al., 2002; Spitzer and Kleinman, 1961)*
		Si-O Asymmetrical Stretching	1080, 1102, 1177	
Phyllosilicates	Illite	-O-H Bending	916	*(Madejová et al., 2017; Madejova and Komadel, 2001)*
		Si-O Asymmetrical Stretching	1033	
Carbonates	Calcite	C-O Asymmetrical Stretching	879 to 904	*(Bishop et al., 2021; Green and Schodlok, 2016)*

Linear Combination Method

Airborne dust particles occur as a mixture of pure minerals in the volume of a particle. The distribution of the molecules can be heterogeneous in the case of an internal

mixture or homogeneous in the case of an external mixture. By individual-particle analysis, SEM measurements of Gobi sample particles showed an external mixture. **Figure 58a** shows the micrograph of a particle using the SEM technique, indicating its morphology and mixture state. In addition, Energy-Dispersive X-ray Spectroscopy allows the fraction of minerals found in each particle. The study was performed on hundreds of individual particles, from which 80% were composed of 70% of one mineral**,** as indicated in **Figure 58b**.
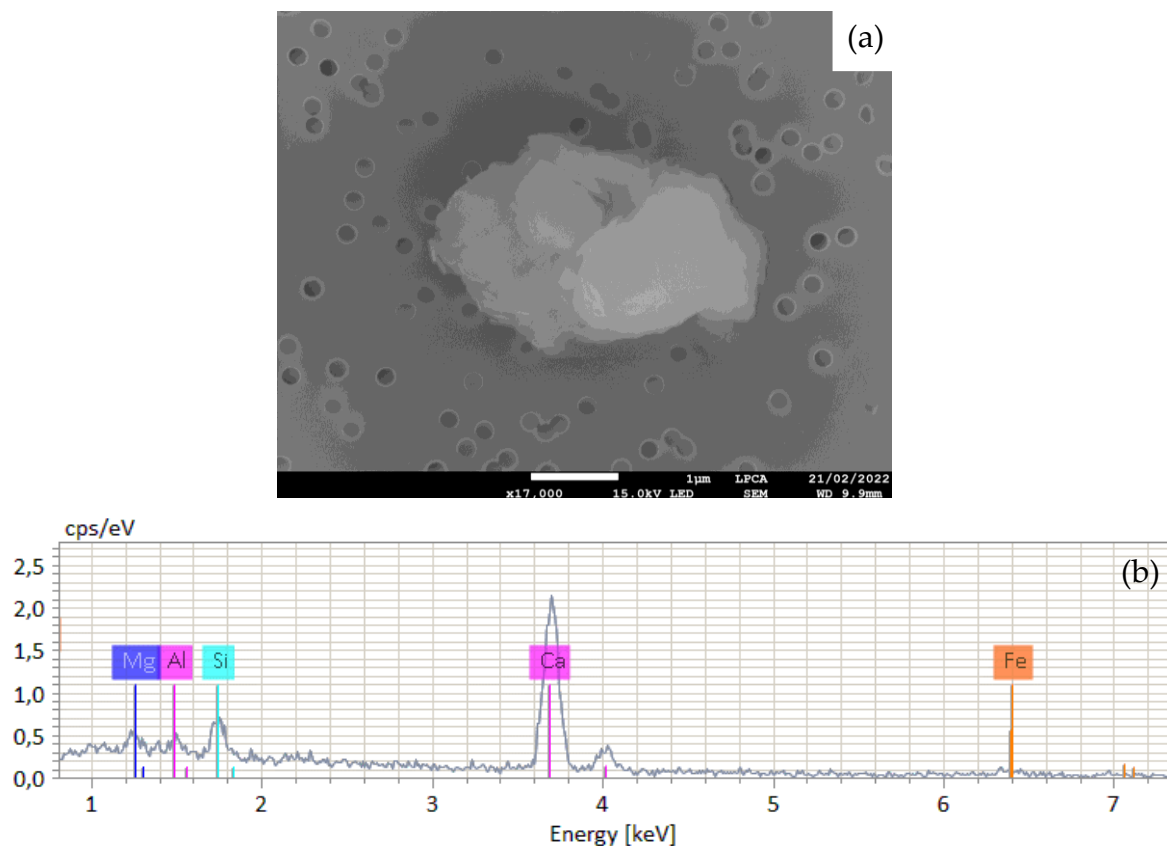
Figure 58 (a) Scanning electron micrograph and **(b)**the Energy-Dispersive X-ray Spectroscopy chart (low panel) of an individual particle of Gobi dust sample showing the associated minerals *(Bichon et al., 2021)*.

In this case, the optical properties of individual minerals can be used to model the optical properties of dust. An effective extinction coefficient $k_{eff}(v)$ can be obtained from a linear combination (LC) of the individual mineral extinctions *(Sokolik and Toon, 1999)*. The combination is calculated from the normalized experimental extinction coefficients

of quartz $\bar{k}_Q$, illite $\bar{k}_I$, and calcite $\bar{k}_{Ca}$, with an extinction fraction of the mineral groups in question, f_{Tec}, f_{Phy}, and f_{Ca}, respectively, and it is calculated by:

$$k_{eff}(v) = f_{Tec}\bar{k}_Q(v) + f_{Phy}\bar{k}_I(v) + f_{Ca}\bar{k}_{Ca}(v) \quad \textbf{(26)}$$

Equation (26) is of the form $\mathbf{b} = \mathbf{Ax}$ where b is the dust measurement spectrum for *n* wavenumbers, **A** contains the individual minerals spectra, and **x** is the unknown mass weight vector. In this case, we have more equations than unknowns and the system is overdetermined. This problem is resolved by the linear approach which uses a least square solution that minimizes **Ax** from **b**, by multiplying both side by the transpose matrix $\mathbf{A^T}$, and it is given by:

$$\mathbf{A^T b = A^T A x} \quad \textbf{(27)}$$

Then the remaining residue is calculated by:

$$\|\boldsymbol{b - Ax}\| \quad \textbf{(28)}$$

Figure 59 shows an LC simulation fitted to the Gobi dust spectrum. The individual mineral spectra reproduced a fit with 13.7% of quartz, 79.8% of illite, and 6.5% of calcite to obtain an external mineral mixture spectrum with the remaining residue $\in_{Re}$ from the predicted spectrum $k_{eff}(v)$ and the experimental spectrum $k_{exp}(v)$. The residue difference between the LC simulated spectrum and the Gobi dust spectrum is 2.5%.
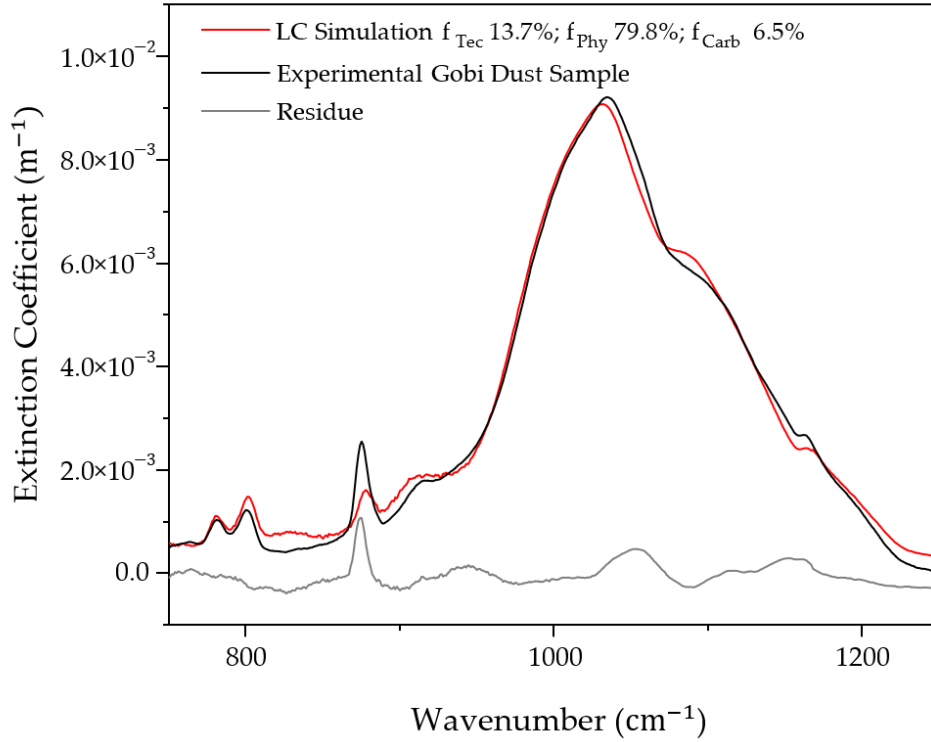
Figure 59 Simulation of the linear combination of pure mineral coefficients (red) fitted with the experimental Gobi dust extinction spectrum (black) with the remaining residue from the simulation and experimental spectrum (gray).

In order to compare the results with the data in the literature, it is important to convert the extinction weights to mass weights. This can be performed by obtaining the mass extinction coefficient MEC (in $m^2 . g^{-1}$), which can be calculated from the maximum value of the extinction coefficient $k_i^{max}(v)$ divided by the mass concentration MC_i for the mineral i:

$$MEC_i = \frac{k_i^{max}(v)}{MC_i} \quad \textbf{(29)}$$

where MC_i is obtained from the particle size distribution recorded experimentally by the APS and the SMPS. The densities used in this study for the mineral components quartz (Q), illite (I), and calcite (Ca) were $\rho_Q = 2.65\,g . cm^{-3}, \rho_I = 2.8\,g . cm^{-3}$, and $\rho_{Ca} = 2.71\,g . cm^{-3}$, respectively.

Hence, the mass weight w_i is obtained the product of the individual mineral extinction weight f_i and its mass extinction coefficient MEC_i, divided by the sum of the same product over all the minerals, and it is given as follows:

$$w_i = \frac{f_i MEC_i}{\sum_i f_i MEC_i} \quad \textbf{(30)}$$

Then, by applying **Equation (29)** to the experimental normalized extinction coefficients, the extinction masses of quartz, illite, and calcite were $MEC_Q = 0.189 \text{ m}^2\text{g}^{-1}$, $MEC_I = 0.209 \text{ m}^2\text{g}^{-1}$, and $MEC_{Ca} = 0.187 \text{ m}^2\text{g}^{-1}$, respectively. The obtained mass weights from **Equation (30)** are: $w_{Tec} = 15.3\%$, $w_{Phy} = 80\%$, and $w_{Carb} = 4.7\%$, respectively.

3.2 MINERALOGICAL MAPPING USING IASI

3.2.1 IASI Molecular Features

The optical thickness was derived from the IASI radiance (defined in **Chapter II)**, corresponding to the dust extinction coefficient multiplied by a dust layer (**Equation 25**). Furthermore, the experimental extinction coefficient allows identifying spectral features, as discussed in **Section 3.1.2**. To compare the satellite dust detection to the experimental dust measurements, an example of an IASI equivalent optical thickness spectrum of Gobi dust detected on 4th May 2017 was compared with the laboratory optical thickness spectrum of Gobi dust calculated from the optical path of the apparatus multiplied by the extinction coefficient (**Figure 60**). The results show spectral signatures identical to the laboratory dust features, providing information about the mineral families in each detection. Note that this comparison was done to test the sensitivity of IASI optical thickness on the mineral dust spectral features. The C-O asymmetrical stretching allows carbonates detection, and the O-H bending indicates the presence of phyllosilicates. In addition, tectosilicates or phyllosilicates can be distinguished by the Si-O asymmetrical stretching assignment position in the spectrum as it shifts position between the two families. In addition, the Si-O symmetrical stretching reveals the possibility of having either tectosilicates or phyllosilicates in the detection, as the doublets are present at the same wavenumbers

for the two groups. Therefore, using an experimental dust extinction coefficient allows the identification of the mineralogical composition from the IASI optical thickness.
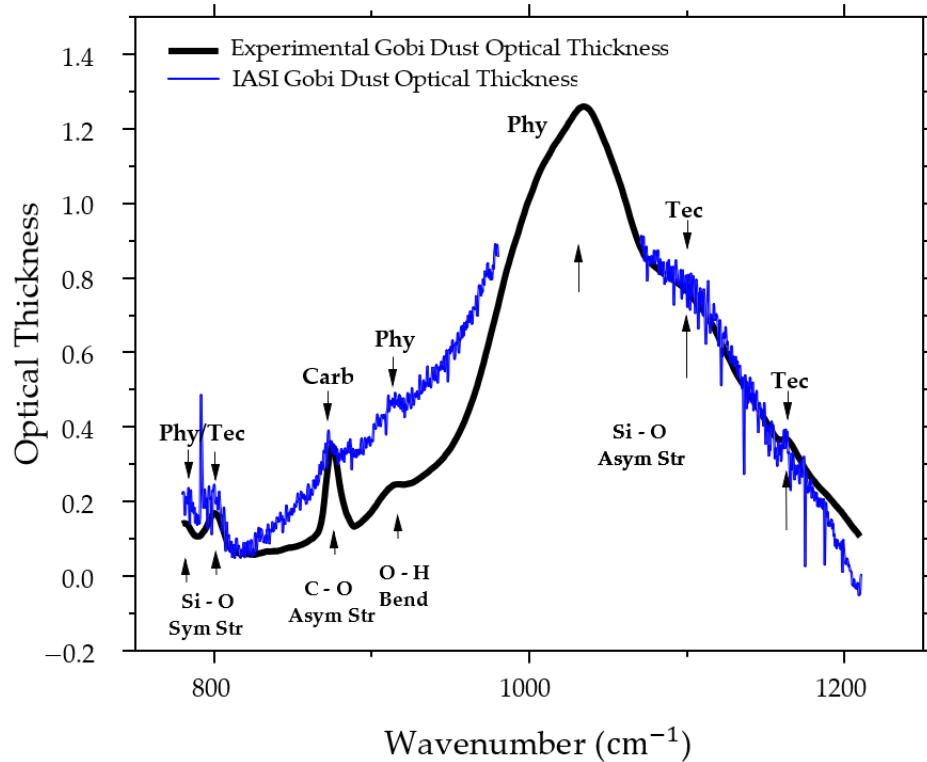
Figure 60 The laboratory Gobi dust spectrum with the molecular assignment for each fingerprint is in black *(Deschutter, 2022)*. Sym Str: symmetrical stretching; Asym Str: asymmetrical stretching; Bend: bending. The IASI equivalent optical thickness detection of the dust plume on 4 May 2017 at daytime after LSE correction, with mineralogical family assignment, is in blue. Tec: tectosilicates; Phy: phyllosilicates; Carb: carbonates.

3.2.2 Linear Combination Method: Application on IASI Observations

Dust sample collection can be critical as the mineral composition is highly variable in source and time, which can pose a challenge when dust sampling is difficult. To remove this dependency, the linear combination of the pure mineral extinctions of quartz, illite, and calcite, described in **Section 3.1.2,** was used to obtain the mineralogical extinction fractions. The equality between the IASI spectral optical thickness $\tau(v)$ from **Equation (25)** and the linear combination from **Equation (26)** is solved as follows:

$$\tau(v) = \left[f_{Tec}\bar{k}_Q(v) + f_{Phy}\bar{k}_I(v) + f_{Ca}\bar{k}_{Ca}(v)\right] \times L + \epsilon \textbf{ (31)}$$

103

where the total error ϵ is the sum of the residue error ϵ_{Re} of gases narrow bands and the error of having other minor families not taken into consideration ϵ_{minor}. The layer thickness L value does not affect the result, as it is considered a constant parameter for each pixel.

In **Figure 61**, **Equations (29)** and **(30)** were applied to an example from the May 2017 dust event. The LC method gives 16.8% for tectosilicates, 78.3% for phyllosilicates, and 4.9% for carbonates. The IASI optical thickness shows intense narrow bands of gases, which increase the residue up to 20%.

To remove gases' narrow bands, the *Savitzky-Golay method* is applied. It performs a polynomial regression to the data points in the moving window *(Press et al., 2007)*. Smoothed window points are chosen in a way so it does not remove the IASI sensitivity to aerosols. The smoothing is computed using MATLAB software developed by Math-Works *(MathWorks, 2019)*.

The residue dropped to 5% by removing the gas effect to smooth the fitting, indicating a significant error caused by the gases present in the atmosphere. In addition, the calculated values are close to the percentages obtained in the experimental spectrum. Therefore, the LC method allowed us to obtain new mineralogical mass weights from satellite IASI detections using laboratory optical properties of major pure minerals.
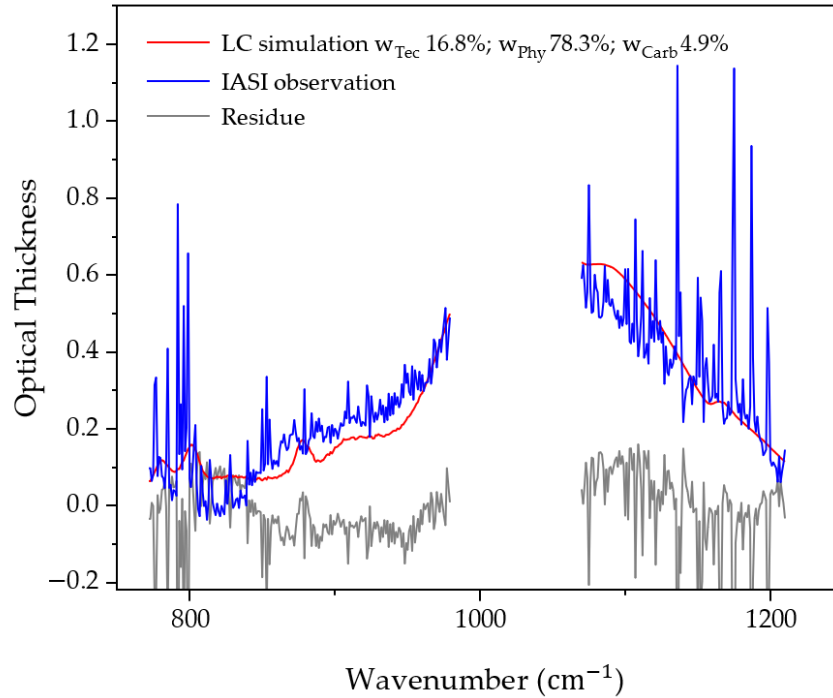
Figure 61 Simulation of the linear combination of pure mineral coefficients (red) fitted with the IASI dust optical thickness (blue) with the remaining residue from the simulation and experimental spectrum (gray) and the RMS (light gray envelope).

3.3 CASE STUDIES

After testing the LC method on both laboratory measurements and satellites observations, in this section we will apply the method on case studies of dust storms in East Asia. We used IASI-A for the first dust storm in May 2017, and a second dust storm in March 2021. In the two cases, we will link the mineralogical mass weights to regional dust sources. Finally, we compared results between IASI-A and IASI-B.

3.3.1 May 2017 from IASI-A

An intense dust storm occurred from 3 to 8 May 2017, affecting visibility in North China as dust loads crossed the region. The storm started in the southwest of inner Mongolia, where the dust plume moved southeastward, passing through North China, the Korean peninsula, and Japan to dissipate in Russia. Three cold fronts generated dust during this event. The first two fronts lifted dust from the Gobi Desert on 3 May. On 4 May, at night, a third front started and different blown dust loads were generated and merged

between 4 and 6 May from both the Horqin Sandy Land and Gobi Desert *(Minamoto et al., 2018)*. **Figure 62** shows the evolution of the dust plume mass weights for tectosilicates, phyllosilicates, and carbonates in May 2017 between 3 and 6 May. The dust plume could not be detected anymore on 7 and 8 May. In addition to the calculation of the RMS of the residue obtained from the LC method. The optical thickness at 1072.5 cm^{-1}, where the aerosol absorption feature is the strongest. The IASI optical thickness at 1072.5 cm^{-1} shows a homogeneous temporal evolution between day and night detections.

The LC method was applied to approximately 4000 spectra, from which 8% rejected solutions with negative mass weights. The rejected values can be linked to the difference in the size-fraction between the IASI dust detections and experimental dust used for the LC fitting. This result indicates the importance of the microphysical dust information to better estimate the mineralogical composition.

All the mineral families during this dust event reported wide spatial variability. **Table 3** presents for each overpass the mean mass weight values, RMS, and the optical thickness at 1072.5 cm^{-1} in the three regions (I, II, and III) presented in **Figure 55**. The mean value of tectosilicates was 48.5% in region I, whereas it was less than half in regions II and III. Conversely, the contents of phyllosilicates in regions II and III were close to 73% and 46% in region I. The contents of carbonates in the three regions had values of around 5.5%.

The hybrid single-particle Lagrangian integrated trajectory (HYSPLIT) model has employed to link the mineralogical values to the possible dust sources. **Figure 63** shows 24 h of backward trajectories on 5 May at 11 UTC, predicting the sources of detected dust masses. From the left to the right, the first (I) comes from the Taklamakan Desert. Dust particles are emitted in the region without long-distance transport, which is explained by the high content of tectosilicates and the lower content of phyllosilicate. The second (II) originates from the Gobi Desert, traveling Eastward with the lowest tectosilicate and the highest carbonate content. The third (III) shows the Gobi load trajectory transported North-Eastward and passing above the Horqin Sandy Land, where its dust loads are mixed with Gobi dust. In the example of 5 May during the day (5D), the weight of the

tectosilicates strengthened again after a third cold front mixed dust from both deserts since the Horqin Sandy Land is rich in feldspars *(Shen et al., 2009)*.
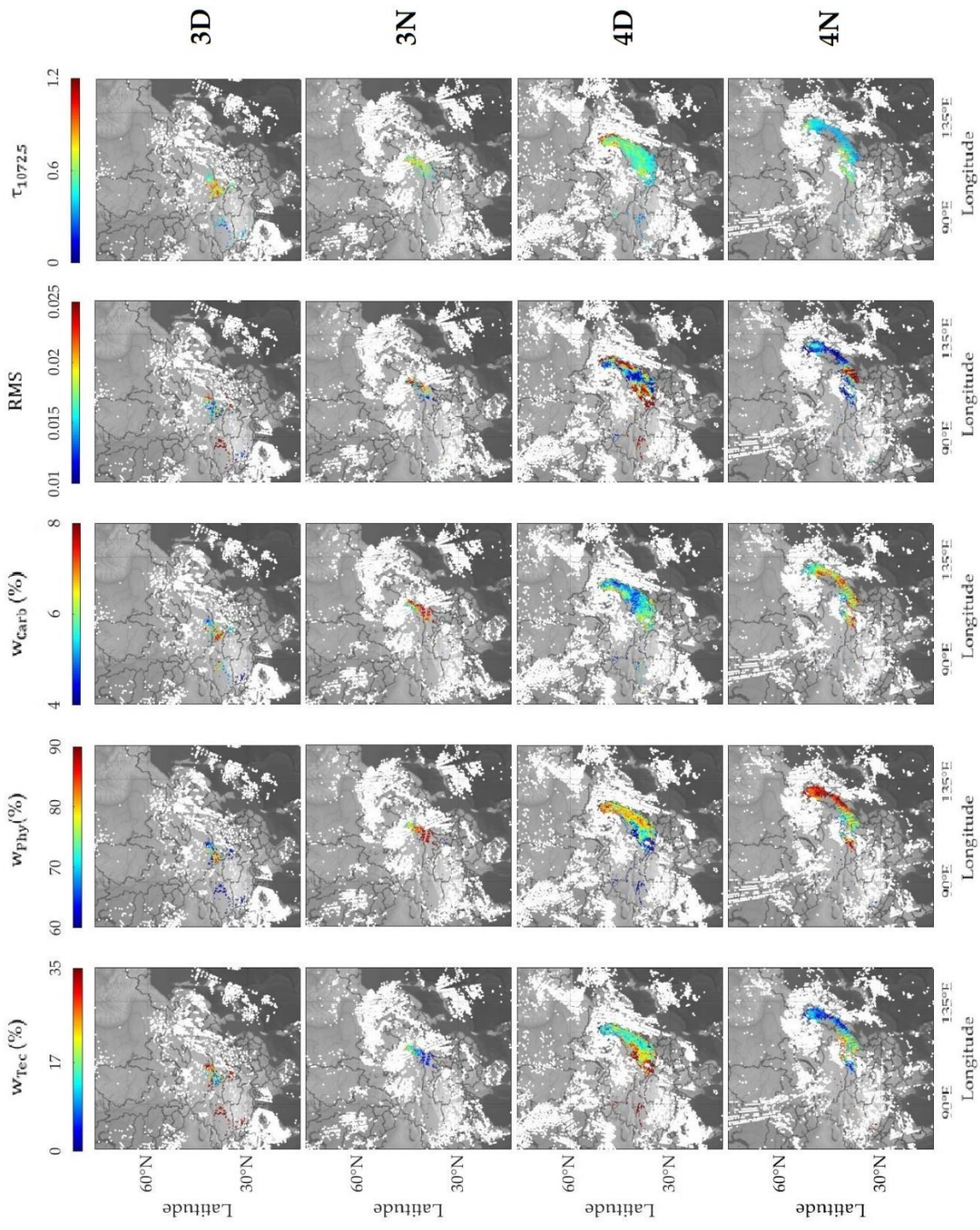
Figure 62 Mineralogical mass weight maps of tectosilicates, phyllosilicates, and carbonates during the 3–6 May 2017 dust storm by day (D) and night (N) from IASI detections. The last two column from the left also show the RMS of the spectral residues of the LC method and the optical thickness at 1072.5 cm⁻¹ (graph continues to next page).
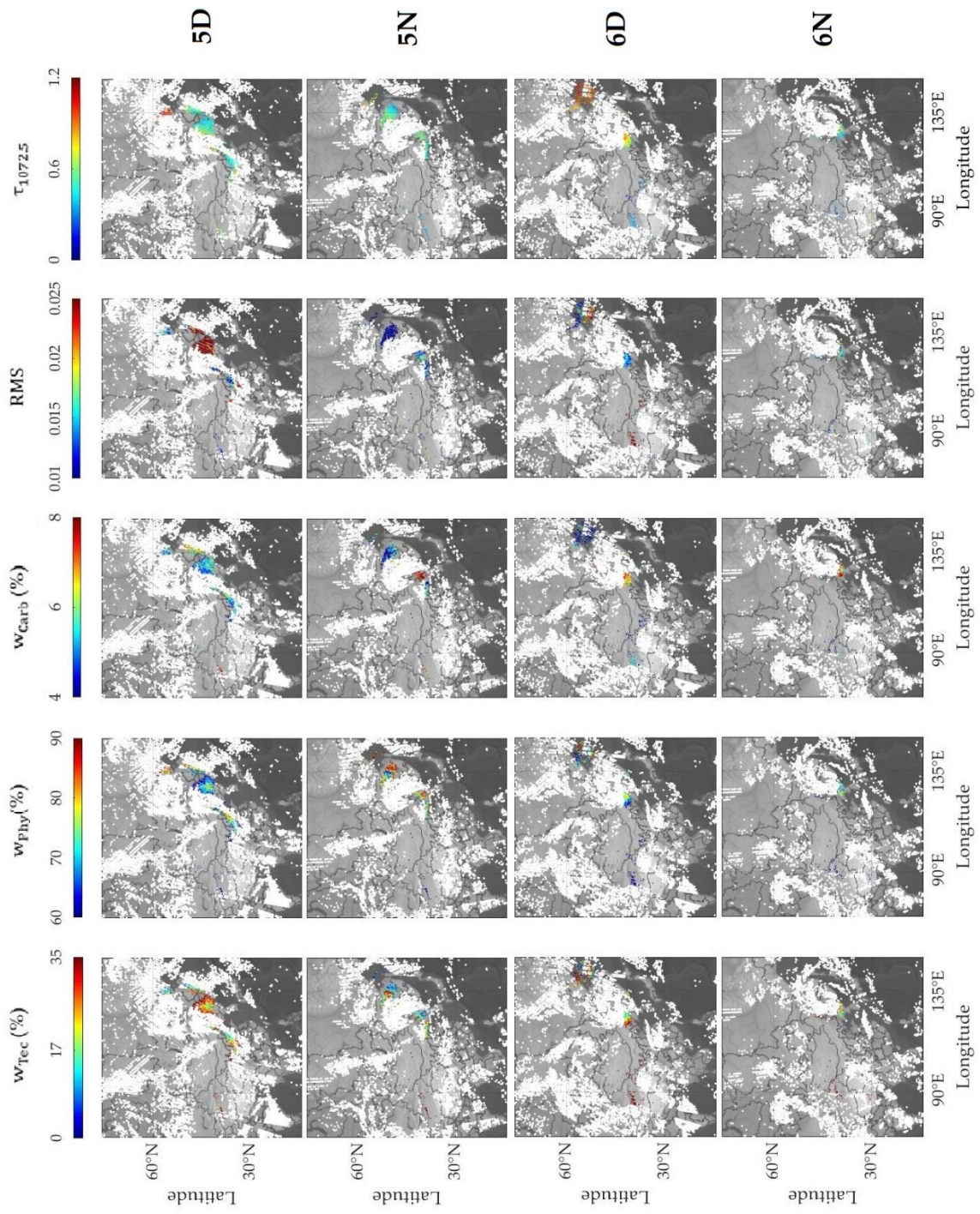
Table 3 The IASI mean mineralogical values and STD of the three dust region sources in the dust storm of May 2017 in East Asia.

| Date | Mean Mass Weight per Half-Day (%) | | | | | | | | | Mean RMS | | | Mean $\tau_{1072.5\ cm^{-1}}$ | | |
| | Tec | | | Phy | | | Carb | | | | | | | | |
	I	II	III	I	II	III	I	II	III	I	II	III	I	II	III
3D	52.0	23.5	-	43.0	70.4	-	5.0	6.1	-	0.029	0.018	-	0.357	0.706	-
3N	46.0	10.8	-	48.5	82.3	-	5.5	6.9	-	0.017	0.018	-	0.477	0.631	-
4D	55.4	20.2	-	39.5	74.3	-	5.1	5.5	-	0.029	0.018	-	0.368	0.555	-
4N	50.8	12.5	-	46.1	81.2	-	3.1	6.3	-	0.014	0.015	-	0.574	0.456	-
5D	37.9	20.3	27.5	55.4	74.1	67.3	6.7	5.6	5.2	0.013	0.021	0.033	0.667	0.603	0.515
5N	43.9	17.2	17.2	50.8	76.2	78.6	5.3	6.6	4.5	0.015	0.014	0.008	0.406	0.539	0.529
6D	57.0	23.5	23.4	38.4	69.8	72.9	4.6	6.7	3.7	0.045	0.015	0.016	0.325	0.702	0.916
6N	45.1	23.6	-	51.1	69.5	-	3.8	6.9	-	0.014	0.016	-	0.407	0.516	-
Mean	48.5	19.0	22.7	46.6	74.7	72.9	4.9	6.3	4.4	0.022	0.017	0.019	0.448	0.589	0.653
STD	6.0	4.7	4.2	5.6	4.6	4.6	1.0	0.5	0.6	0.011	0.002	0.011	0.111	0.083	0.186

Figure 63 HYSPLIT 24 h backward trajectory for different dust detections in dust storms on 5 May 2017 by night (*https://www.ready.noaa.gov/index.php*, accessed on 1 December 2021).

3.3.2 Generalization

March 2021 from IASI-A

The mineralogical mapping method was applied to a more recent dust storm in March 2021. The first dust plume was generated from the Mongolian Gobi Desert on 14 March, with winds blowing on 15 March, uplifting aerosols from the Gobi Desert and Horqin Sandy Land together to travel southeastward. On 16 March, another dust plume was produced from the Taklamakan Desert, mixing with loads already in the atmosphere. A previous study only investigated emissions from the Gobi Desert between 14 and 15 March *(Wang et al., 2021)*.

The study applied was applied between 14 March and 18 March during the day, as shown in **Figure 64**. The IASI mineralogical weights showed a regular temporal evolution as the first and second dust plumes were carried into the atmosphere. From 3500 spectra, the LC fitting rejected 15% of the values, the double of values rejected for the May 2017

event. The result can be linked to the difference in the size distribution between the emissions for the two cases in the study; the PM_{10} (suspended particles with a diameter less than 10 µm) concentration emissions were doubled in March 2021 *(She et al., 2018)*.

Table 4 shows the IASI mean mineralogical values per half-day, with the RMS and the optical thickness at 1072.5 cm^{-1}. In this case, the mean mass weight value of the tectosilicates was 25% in region I. Intense dust emissions from this region started on 16 March during the day (16D), and the dust was found to be made up of 66% phyllosilicates and 7.4% carbonates. In region II, the results show consistent mineral weights with the previous case study. However, region III indicates the uplift of heavier tectosilicate particles and fewer phyllosilicate fine particles. The carbonate mean values were close for region I and II, with the highest peak from region I at 9% and the lowest in region III at 5.2%. Large optical thickness values were found in this case as the dust mass concentration emitted reached almost 1×10^4 µg/m^3 while the May 2017 concentrations reached a maximum of 5×10^3 µg/m^3 *(She et al., 2018; Wang et al., 2021).*
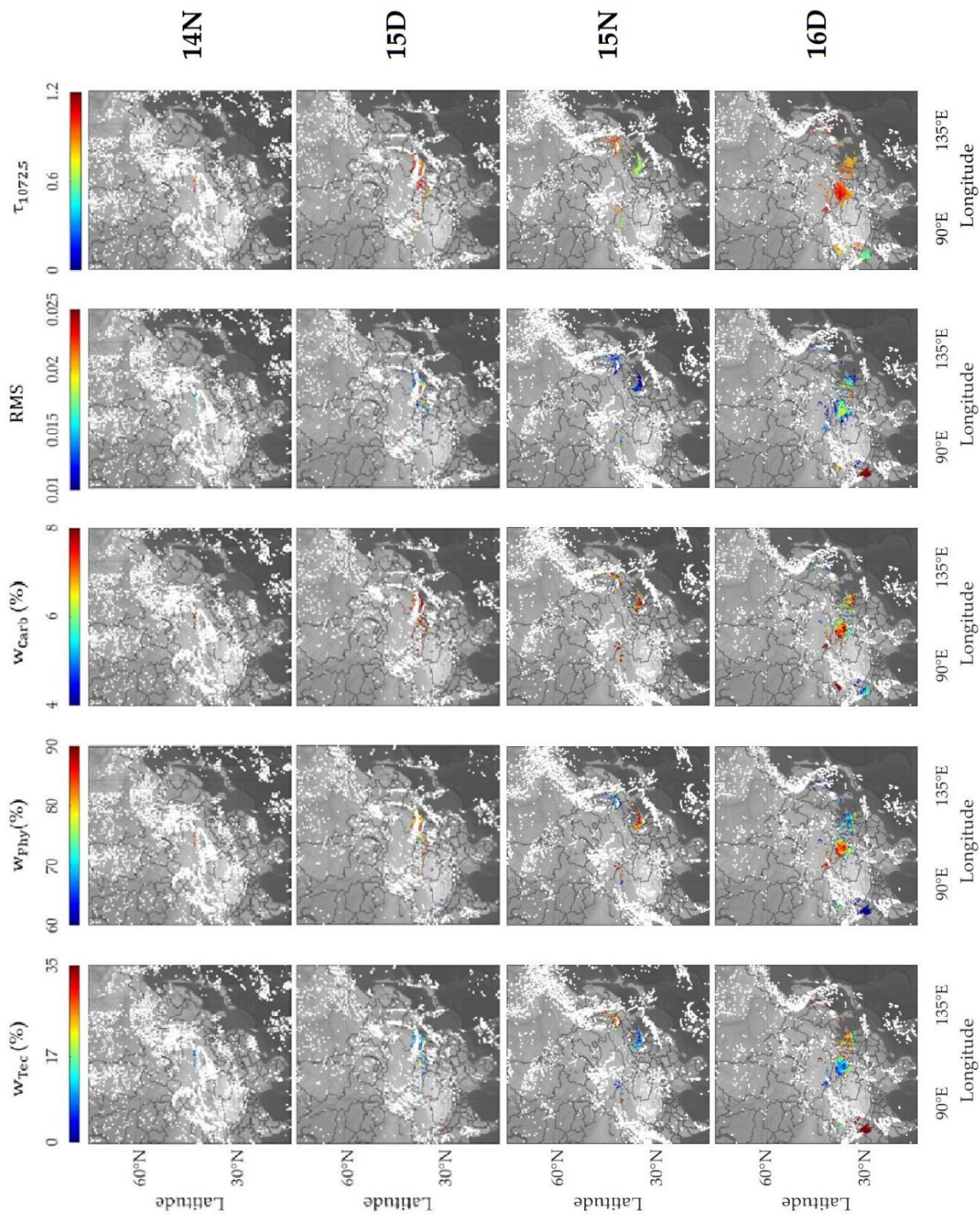
Figure 64 Mineralogical mass weight maps of tectosilicates, phyllosilicates, and carbonates during the 14–18 March 2021 dust storm by day (D) and night (N) from IASI detections. The last two column from the left also show the RMS of the spectral residues of the LC method and the optical thickness at 1072.5 cm⁻¹ (graph continues to next page).
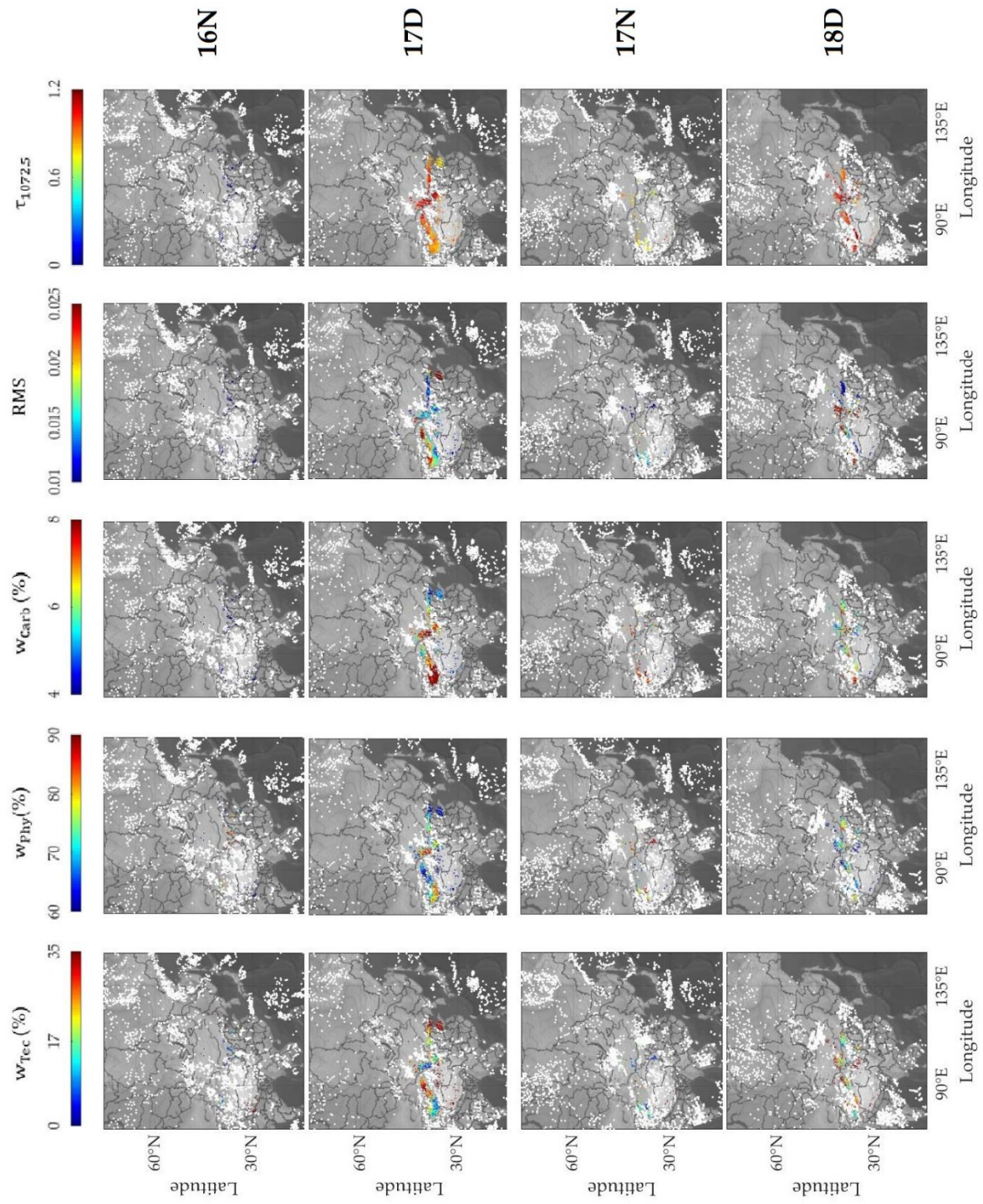
On 15 March 2021, dust mass III had high tectosilicate content having a mixture of the Gobi and Horqin sources, a similar scenario to 5 May 2017, with the Horqin Sandy land source causing the increase in tectosilicate weight. The mass load II shows lower tectosilicate content as it originated only from the Gobi Desert. In addition, the weight of phyllosilicates was higher in II than III, suggesting that dust emissions in II were from the Gobi Desert. By 16 and 17 March (16N and 17N), clouds covered the region, masking dust plumes detection. On 17 March by day (17D), the mineralogical weights had heterogeneous variability in the three different regions, each related to a different source. We used the HYSPLIT 24 h backward trajectory that shows on 17D the presence of dust emission in region I above Taklamakan Desert, originating from 16 March by day and traveling in the same direction (Eastward) as the uplifted masses of region II from the Gobi Desert. In addition, another mass traveled from Central Asia, showing different mineralogy that was particularly rich in tectosilicates (the values of this plume are not shown in **Table 4**).

On 15 March 2021, dust mass III had high tectosilicate content having a mixture of the Gobi and Horqin sources, a similar scenario to 5 May 2017. On the other hand, mass load II shows lower tectosilicate content as it originated only from the Gobi Desert. Hence, the Horqin Sandy land is an important dust source rich in tectosilicate. In addition, the weight of phyllosilicates was higher in II than III, suggesting that dust emissions in II were from the Gobi Desert. By 16 and 17 March (16N and 17N), clouds covered the region, masking dust plumes detection. On 17 March by day (17D), the mineralogical weights had heterogeneous variability in the three different regions, each related to a different source. Therefore, we used the HYSPLIT 24 h backward trajectory on 17D to better understand the origin source (**Figure 65**). Three locations were selected; the first trajectory, on the left, shows a mass that traveled from Central Asia, having different mineralogy that was particularly rich in tectosilicates (the values of this plume are not shown in **Table 4**). The second indicates that dust emissions occurred on 16 March day above the Taklamakan Desert (region I), which occurred and traveled in the same direction (Eastward) as the third uplifted masses of region II from the Gobi Desert.

Table 4 The IASI mean mineralogical values and STDs of the three dust region sources in the dust storm of March 2021 in East Asia.

| Date | Mean Mass Weight per Half-Day (%) | | | | | | | | | Mean RMS | | | Mean $\tau_{1072.5 \text{ cm}^{-1}}$ | | |
| | Tec | | | Phy | | | Carb | | | Date | | | Tec | | |
	I	II	III	I	II	III	I	II	III	I	II	III	I	II	III
14N	-	26.6	-	-	65.1	-	-	8.3	-	-	0.014	-	-	0.958	-
15D	-	16.1	-	-	75.9	-	-	8.0	-	-	0.016	-	-	0.971	-
15N	-	22.4	44.1	-	69.3	50.2	-	7.1	5.2	-	0.017	0.010	-	0.698	0.967
16D	21.9	17.0	40.1	68.1	76.4	54.7	9.0	6.8	6.4	0.020	0.015	0.011	0.833	0.943	0.72
16N	-	26.0	-	-	66.9	-	-	7.4	-	-	0.020	-	-	0.731	-
17D	23.8	23.6	-	68.8	69.9	-	7.4	6.4	-	0.019	0.017	-	0.892	0.976	-
17N	28.8	26.6	-	62.0	66.7	-	6.8	6.3	-	0.025	0.016	-	0.786	0.776	-
18D	26.8	24.4	-	67.0	69.4	-	6.2	6.2	-	0.016	0.015	-	1.024	1.002	-
Mean	25.3	22.8	42.1	66.5	70.0	52.5	7.4	7.1	5.8	0.020	0.016	0.011	0.884	0.882	0.841
STD	2.7	3.9	2.0	2.6	3.9	2.2	1.0	0.7	0.6	0.004	0.002	0.011	0.089	0.117	0.124

Figure 65 HYSPLIT 24 h backward trajectory for different dust detections in dust storms on 17 March 2021 by day (*https://www.ready.noaa.gov/index.php*, accessed on 1 December 2021).

IASI-A and IASI-B

METOP A ended its mission in November and December 2021, and only METOP B and C continue the mission. Hence, a comparison between IASI-A and IASI-B is crucial to test the applicability of this study on the present IASI platforms. The comparison was applied to the 2017 case study, where only two METOPs, A and B, were in an orbital phase with a time gap of 45 min, with similar views from both satellites ensuring the maximum daily coverage. The results from 4 May 2017 during the day are shown in **Figure 66**, with no notable spatial shift between the two platforms as the dust plume traveled slowly from west to east. The plume mineralogical extinction evolution increased consistently in mineral weights after 45 min according to IASI-B, with continuous dust emissions from the Gobi Desert. The 1500 dust spectra were selected from IASI-A, while 2400 spectra were selected from IASI-B due to the overlap in IASI orbits. These results confirm the ability to apply this method using different IASI platforms, in addition to the ability to identify the dust emission source.
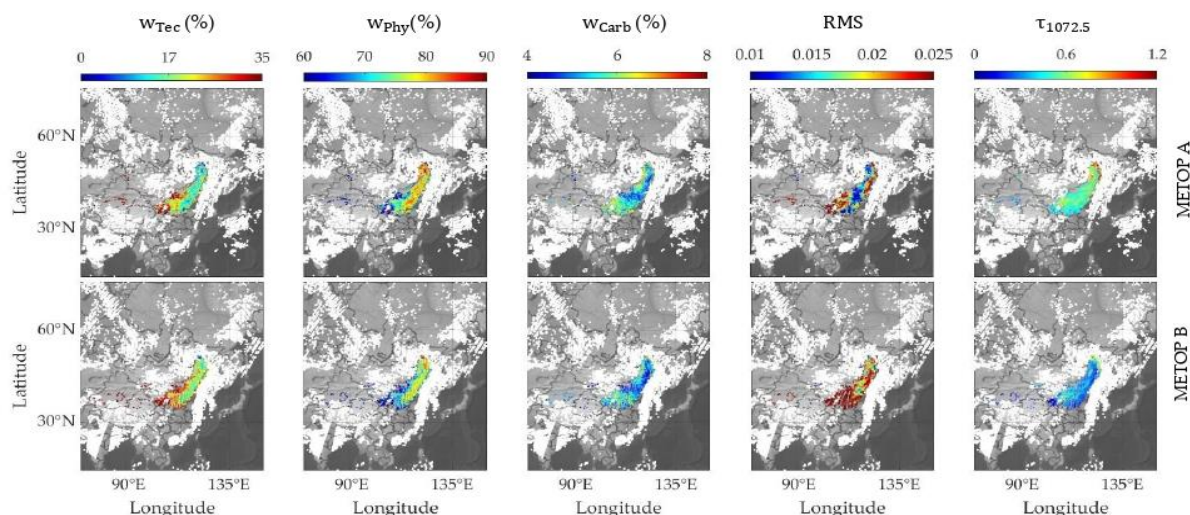
Figure 66 Mineralogical extinction coefficient maps of tectosilicates, phyllosilicates, and car-bonates on 4 May during the 2017 dust storm from IASI detection of METOP A and METOP B. The last two column from the left also show the RMS of the spectral residues of the LC method and the optical thickness at 1072.5 cm^{-1}.

In conclusion, we were able to apply the LC method and evaluate the spatial and temporal evolution of the chemical composition on two case studies: May 2017 and March 2021, with four years of difference and two different seasons. Results were homogeneous between daylight and night detections, and between two MetOp platforms A and B. Moreover, we were able to link the results with dust sources.

3.4 RESULTS COMPARISON WITH LITERATURE

Journet et al., 2014 provided airborne dust mineralogical datasets on a global scale using parent soil samples and a transport model. On the other hand, *Wang,* 2019 used XRD method on a sample from the Gobi Desert to obtain dust mineralogy. In study, we use the LC method to obtain composition information using laboratory spectral measurements and IASI satellite detections. For both cases, the mass weight values of phyllosilicates are closer to the percentages found for clay dust from *Journet et al., 2014* than by the regional study from *Wang, 2019*. On the other hand, the percentage of tectosilicates lies between the values of these two studies. The obtained results can be related to the size fraction. This work used laboratory spectra having a clay-sized distribution similar to the indirect approach applied on clay fractions studied by *Journet et al., 2014*. However, the XRD

118

regional measurement didn't distinguish clays from silt particles which explains a lower content of phyllosilicates and higher content tectosilicates in their study. In addition, the IASI mineralogical values applied on region I displays two scenarios: May 2017 tectosilicates content was high and characterized by short-range aeolian transport, and the second case in March 2021 shows low tectosilicates content characterized by a long-transport.

3.5 PERSPECTIVES TOWARDS SOLVING THE RETRIEVAL PROBLEM

Remote sensing instruments capture the solar and terrestrial radiation passing through the atmosphere and interacting with its components. Therefore, these sensors do not give a direct measurement of the aerosol's particle size or concentration but rather their influence on atmospheric radiation. Here lies the importance of the *inversion methods*, which enable us to solve an inverse problem and retrieve aerosols' microphysical parameters. In this section, we introduce briefly the concept of the microphysical retrievals with a sensitivity study on major dust parameters using ARAHMIS code. In addition, we show present work's results (simulation and inversion) on an example of IASI spectrum.

An inverse problem finds from a set of observations the causal atmospheric state that produced them. It solves a set of linear or non-linear equations in the presence of some errors in the measurements and assumptions made to formulate the equations. A retrieval problem has two components: a *forward model* that presents the calculation of the measurements from the target quantity and the *inverse model* which gives an estimation of this quantity with associated errors. In order to solve the inverse problem the main question is : "Given the radiation field, how well may we infer atmospheric parameters from this information?"- *Goody and Ynug, 1995*. Solving the retrieval problem in remote sensing is mathematically ill-conditioned; it contains more unknowns than the available equations leading to the existence of multiple solutions. It is necessary in such case to restrict the range of possibilities by applying an *a priori* knowledge of the result.

3.5.1 Forward Model

We consider that the observations (i.e., radiances) measured in the spectral range of an instrument are assembled in the *measurement vector* **y** and the unknown parameters into the *state vector* **x**. This vector can include the geophysical and atmospheric variables: pressure, temperature, gases profiles, aerosol SD, concentration, altitude, thickness layer, and surface emissivity and temperature. The best possible representation of the atmospheric state is determined by the physics of measurement, termed the *forward function f(x):*

$$\mathbf{y} = f(\mathbf{x}) \quad \textbf{(32)}$$

However, one must distinguish between the reality set by **y** that comes with a measurement error $\in$ and the best description of this reality f(**x**) due to a measuring . Hence, **y** is approximated by a forward model **F(x)**, and is written as follows:

$$\mathbf{y} = F(\mathbf{x}) + \in \quad \textbf{(33)}$$

In this work, the measurement vector **y** corresponds to the IASI brightness temperature detection. On the other hand, the state vector **x** has 2 parameters: the aerosol SD and concentration. The first is the *effective radius* r_e (in m), calculated from the geometric radius and geometric standard deviation, and given by **Equation (34)** in general and by **Equation (35)** when the standard deviation is fixed:

$$r_e = \frac{\int r^3 n(r) dr}{\int r^2 n(r) dr} \quad \textbf{(34)}$$

$$r_e = r_g e^{2.5 ln^2 \sigma_g} \quad \textbf{(35)}$$

The second parameter presents the *Volume Mixing Ratio* VMR (in ppm): the ratio of the amount of a substance *i i*n a given volume V_i (in m^3) to the total amount of all species in that volume V_{total} , and it is written as follows:

$$VMR = \frac{V_i}{V_{total}} \quad \textbf{(36)}$$

Reference formulae can be found in detail in *Seinfeld and Pandis, 2006* and summarized hereby. The ratio in **Equation (36)** is multiplied by the partial air column p_{air} (in particles.m^{-2}) to give information about the number of particles per unit surface N_S (in particles.m^{-2}), and it is given by:

$$N_S = VMR \times p_{air} \text{ (37)}$$

Then, the *effective number concentration* can be calculated by:

$$N_e = N_S e^{-3.0 ln^2 \sigma_g} \text{ (38)}$$

Finally, one can derive the *effective mass volume concentration* (in g.m^{-3}) with the effective radius r_e and the effective number concentration N_e, with the knowledge of the aerosol's density ρ, and it is written as follows:

$$M_e = \frac{4}{3} \pi \rho r_e^{3} N_e \text{ (39)}$$

The forward model operator **F(x)** describes the RTE (**Equation (15)** discussed previously in **Chapter II**) is shown in **Figure 67**. To calculate the total extinction coefficient $k(v, h)$, we remove clouds detections.

First, one must consider gases contributions resulting from an additive factor in the absorption cross section. We use the *LBL approach* to calculate the attenuation coefficient $k_{abs \, gas}$ of gases species at all atmospheric levels with a very narrow spectral resolution less than $0.01 \, cm^{-1}$. It is solved by the knowledge of the spectral position lines, their intensity or their width at half maximum. The gases spectral lines are used from the High-resolution Transmission Molecular Absorption (HITRAN).

Second, for simplicity we consider that the particles are spherical. In our case, the parameter factor x is close to 1, since IASI detections have a wavelength close to the diameter of airborne dust ($D \approx \lambda$). Hence, we apply Mie Theory that allows efficient calculation of the aerosol extinction coefficient $k_{ext}^{aerosol}$. To study their influence on the measurement we only vary the SD and concentration parameters. The CRI of Gobi dust spectrum is fixed in this study from *Deschutter, 2022*.

Other fixed parameter is the surface emissivity is computed by using *Zhou et al., 2014* with the LSE correction method described in **Chapter II**. In addition to the values of the atmospheric parameters (Pressure, temperature, gases concentrations) which are used from radio sounders measurements i.e., the UWYO database (http://weather.uwyo.edu/upperair/sounding.html) and reanalysis profiles i.e., ECMWF database (https://apps.ecmwf.int/datasets/). **Figure 67** shows the forward model scheme of ARAHMIS code developed in LOA by *H. Herbin & F. Ducos.*

The plume altitude and thickness layer are determined by lidar measurements e.g., CALIOP/CALIPSO shown in **Figure 53b**.
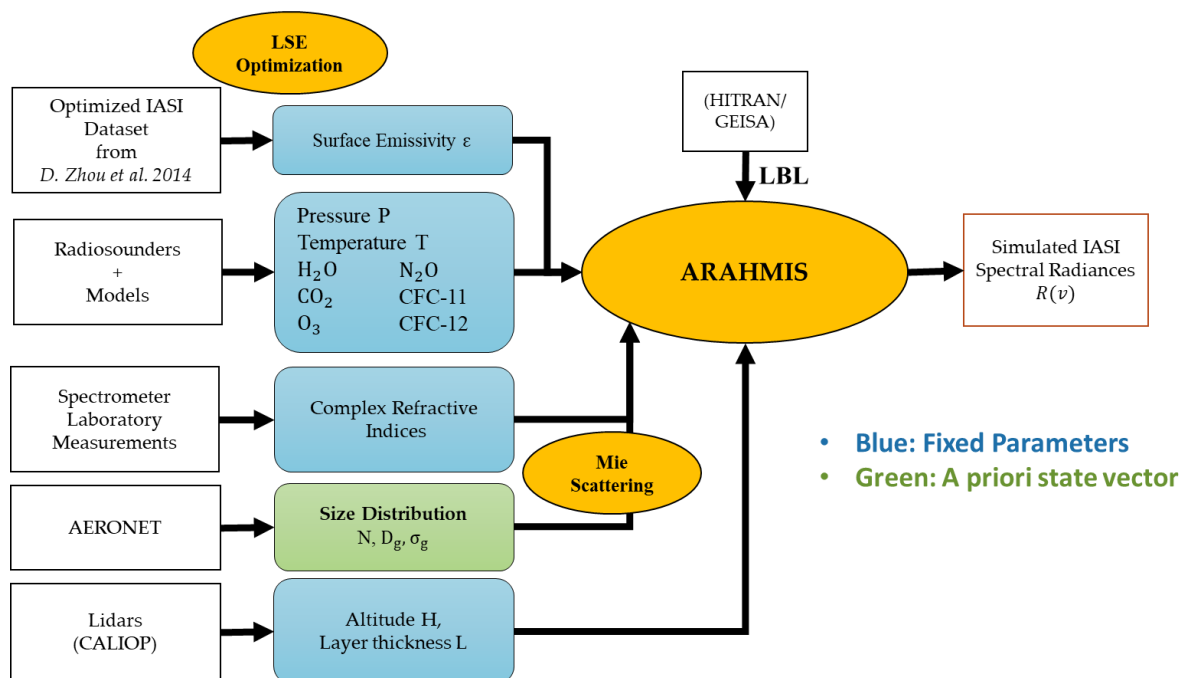
Figure 67 ARAHIS forward model scheme used to simulate IASI spectra.

3.5.2 Influence of the physico-chemical parameters on IASI spectra

Sensitivity on the CRI

The CRI is a crucial parameter because it determines both the contribution of absorption and scattering of the studied particles. Moreover, we have seen previously that, in the spectral domain of thermal IR, the CRI varies according to the chemical composition of the particles (see **Section 3.3**). **Figure 68** shows several simulated IASI spectra of the Gobi dust spectrum with complex refractive indices from the literature *(Di Biagio et al., 2014)* and *(Deschutter, 2022)* used in our work. It is important to specify that the spectra were simulated by fixing the gases concentrations, the altitude of the dust layer between 1 and 3 km, the VMR at 4. 30×10^{-11} ppm, the mean geometric radius at 0.25 µm. We see a difference in the shape of the spectrum as a function of the CRI. More precisely, if we are interested in the spectral range between 800 and 1000 cm^{-1}, we observe that the behavior of the spectra is different depending on the complex index of refraction used (left panel). The choice of the optical properties, impact the simulated spectra, and can alter the retrieval results. Therefore, it is important to choose the adequate CRI representing the mineralogical composition of the IASI observation.
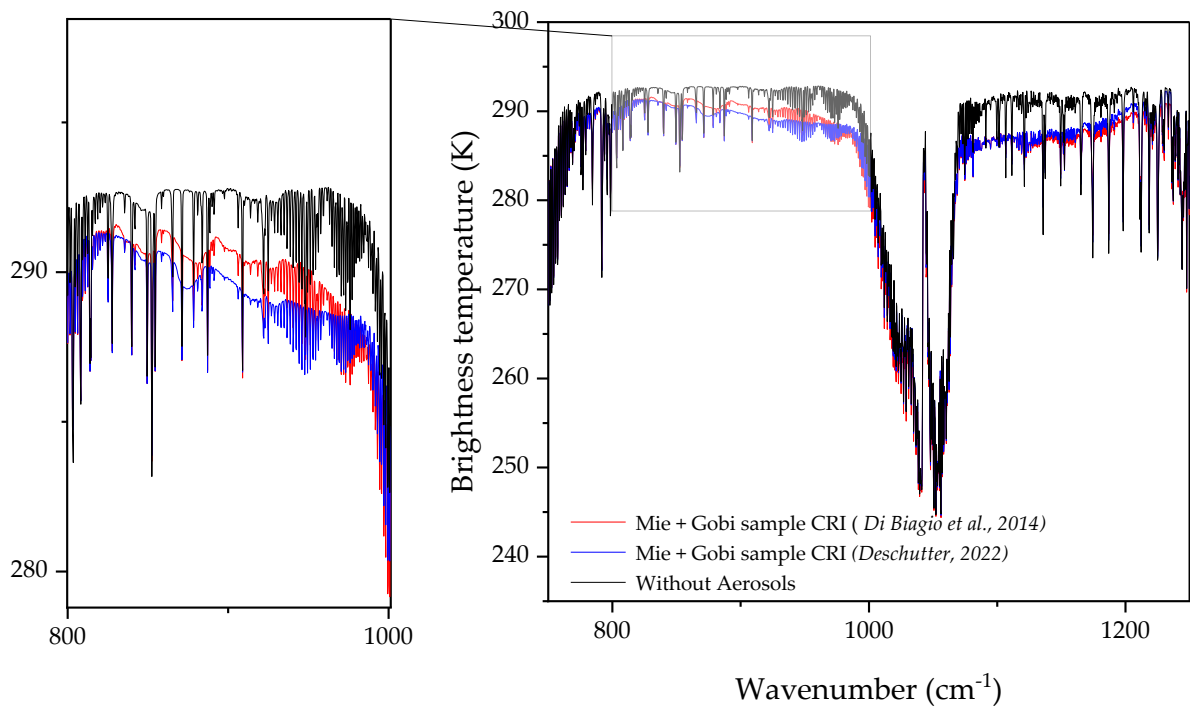
Figure 68 The influence of the CRI on the IASI spectra of Gobi dust compared with spectrum without aerosol particles (right panel) and the zoom between 800 and 1000 cm⁻¹.

Sensitivity on the Altitude

Figure 69 illustrates the influence of altitude on IASI spectra. The spectra were simulated by fixing the gases concentrations, the CRI of Gobi dust from *Deschutter, 2022*, the VMR at 4.30×10^{-11} ppm, the mean geometric radius at 0.25 µm. Depending on the altitude at which the dust plume is located, for a given concentration, the thermal contrast between the surface temperature and the temperature of the layer studied will increase as one rise in the different layers of the atmosphere. The altitude can impact the sensitivity of IASI on the optical thickness. We chose an a priori value of the altitude based on the data recorded by CALIOP or measurements taken from the literature. To constrain the algorithm, we fixed this parameter.
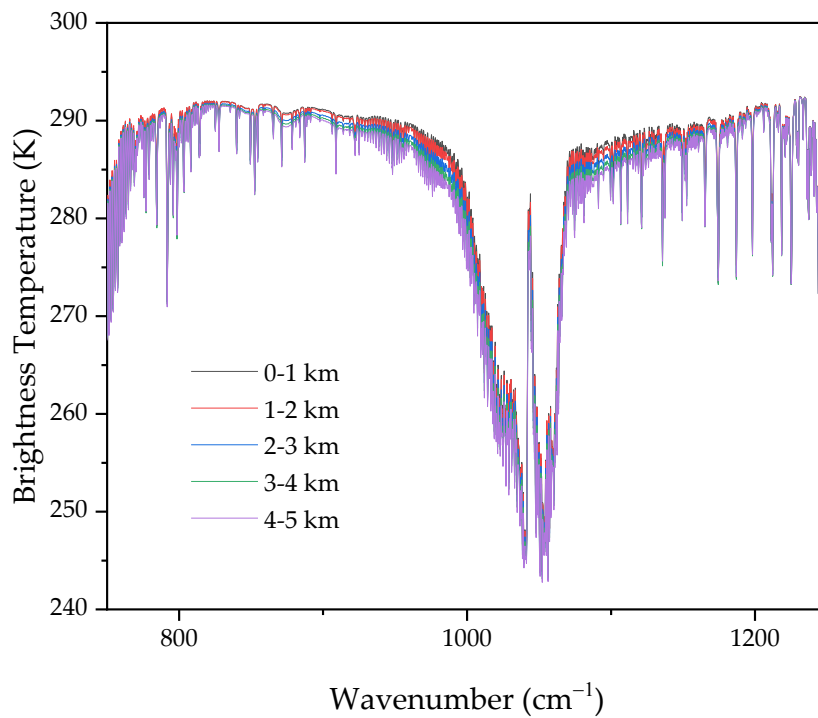
Figure 69 The influence of the altitude of dust plume on the IASI simulated spectra of Gobi dust.

SD Impact

One essential data that should be adjusted is the mean geometric radius of the particles in the dust plume. It is a parameter of the state vector that we want to retrieve. Therefore, it is necessary to establish an a priori value of the mean geometric radius r_g of the aerosol population and then give it a variability. **Figure 70** represents the extinction of Gobi dust plume for radii of 0.15 to 0.50 µm in steps of 0.05 µm. According to the simulations, the mean geometric radius strongly influences the extinction in the studied wavelength range. We must therefore be careful about the choice of the a priori but especially about the variability of this parameter.
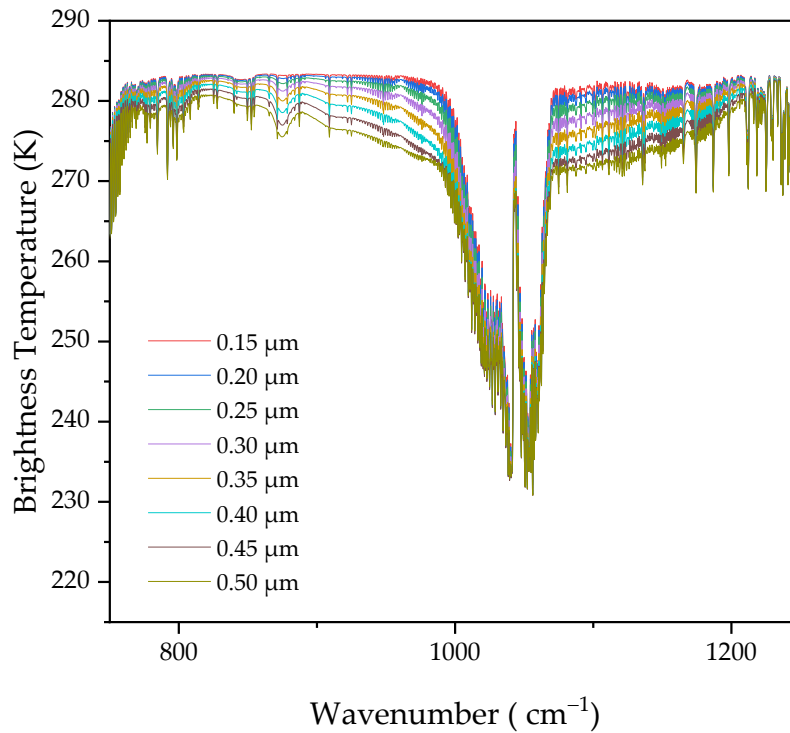
Figure 70 The effect of increasing the mean geometric radius on the IASI simulated spectra of Gobi dust.

VMR Impact

The four Gobi dust spectra in **Figure 71** were simulated for a mean geometric radius of 0.25 μm and a standard deviation of 2 μm at an altitude between 1 and 2 km. We notice that when we increase the VMR, the absorption band of Si-O around 1000 cm^{-1} deepen. This means the more the dust layer is concentrated or thick, the more the 'V-shape' is pronounced.
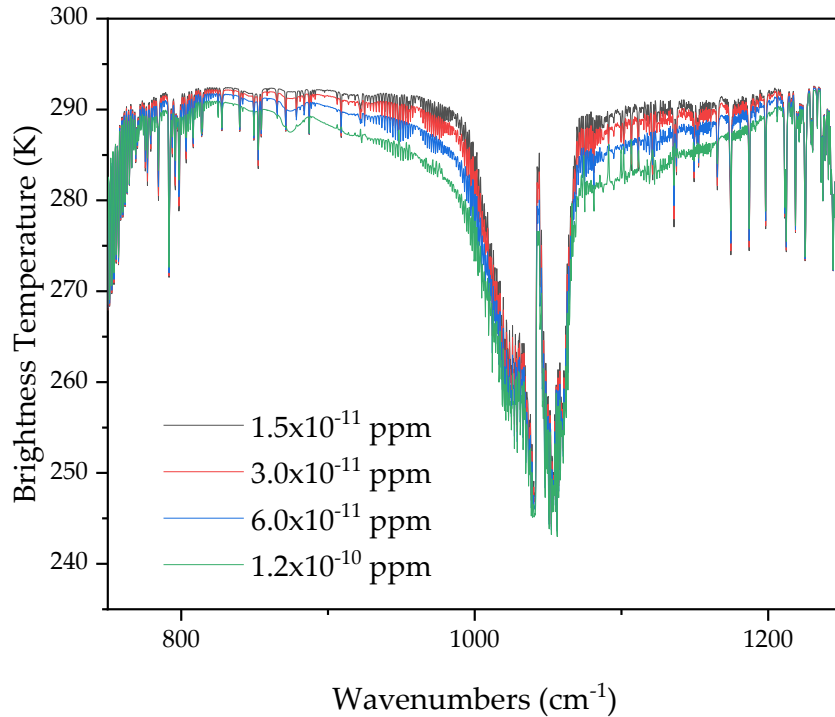
Figure 71 The effect of increasing the VMR the IASI simulated spectra of Gobi dust.

3.5.3 Case Study: May 2017

We apply the forward model on two spectral detections from the case study of May 2017 described in **Section 3.3.1**, in order to solve the retrieval problem and quantify the mean geometric radius and the VMR in a future work. **Figure 72** shows forward model simulations applied to dust spectrum (top panel) and a clear sky above the desert detection (low panel) from May 2017 dust storm. The simulations are fitted to IASI measurements where the gas components were computed using the *Line-by-Line approach*. The surface emissivity was computed using *Zhou et al., 2014* and the LSE optimization method. Aerosols were considered spherical, and Mie's theory was applied to the population of aerosols having a mean geometric radius r_g, a geometric standard deviation σ, and a Volume Mixing Ratio (VMR). The fittings show an RMS (1.01K) having an order close to the instrument noise (0.25 K). This result was obtained with fixing gases parameters and can be improved, which will allow us to solve the inverse problem in the future and retrieve the effective radius and the VMR.
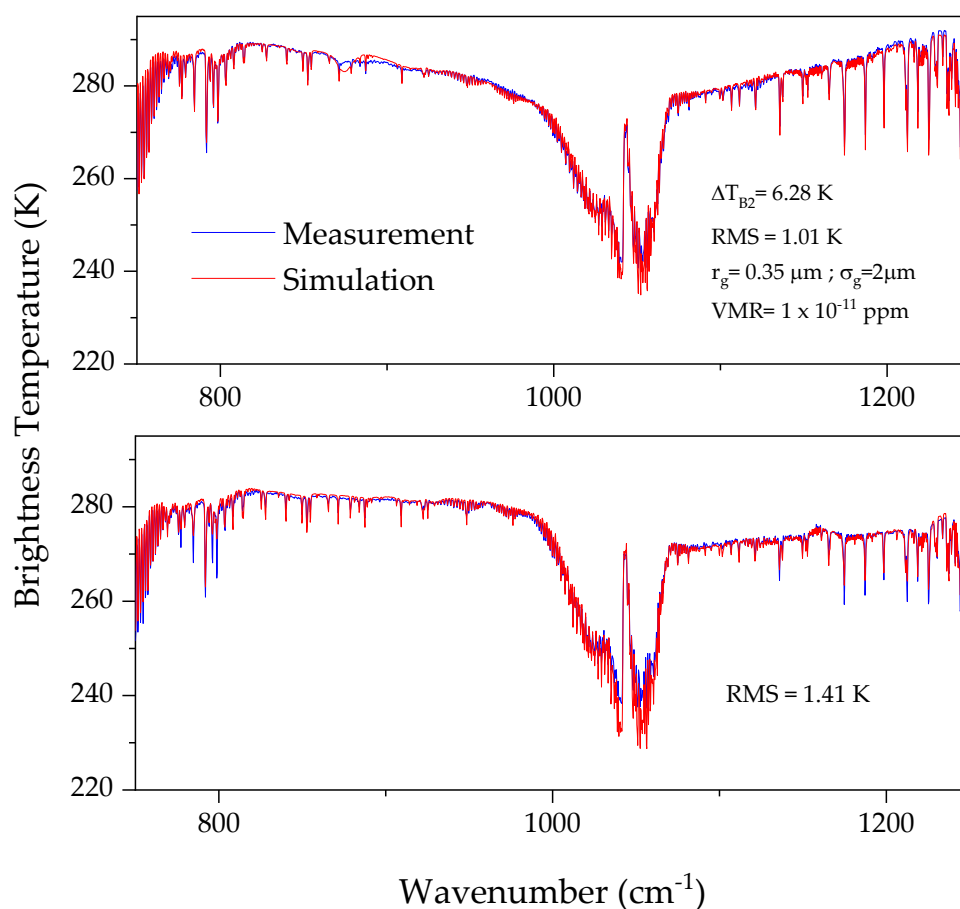
Figure 72 ARAHMIS fits of IASI dust spectrum spectra having different ΔT_{B2} (top panel) and a clear sky above the sea spectrum (low panel) from 4 May 2017.

Conclusion

This chapter introduced a method for computing mineralogical weights during dust storm events using both experimental optical properties and satellite detections from IASI.

First, we considered that dust presents an external mixture of pure minerals and we applied an LC method to the laboratory extinction coefficients of pure minerals to fit the Gobi dust spectrum showing a residue of 2.5%. In addition, after LSE correction, an aerosol optical thickness spectrum from the IASI was derived, with spectral features similar

to those from laboratory Gobi dust sample. The LC was also applied to the satellite optical thickness and the residue shifted to 20% due to the presence of narrow gas bands; however, this residue dropped to 5% after smoothing the IASI spectrum.

Second, mineralogical weight maps were obtained for three mineral groups: tectosilicates, phyllosilicates, and carbonates, with the RMS and the optical thickness at 1072.5 cm^{-1}. The method was applied to two case studies from IASI-A operation by day and night, in two different seasons, with a time gap of four years between them: spring 2017 and winter 2021. The results also showed mean mineralogical weights similar to the clay-sized literature data, with a high temporal and spatial variability for tectosilicates and carbonates that allowed to trace the dust source. Hence, this method presents a powerful tool to link dust mineralogy to the original sources.

These results imply the temporal stability of IASI-A in a time gap of five years and show the ability to use IASI detection in different seasons. In addition, IASI-A and IASI-B were compared giving consistent mineral weights, which allow for the application of this work using different IASI platforms in the future.

Moreover, laboratory optical properties exploited with IASI measurements allowed for obtaining new mineralogical dust composition in the East Asian deserts. Hence, the laboratory optical properties (individual minerals and Gobi dust extinctions) used are suitable. No previous work used satellite remote sensing to differentiate dust mineralogical families. This study crossed the different challenges posed by LSE and the mineralogical variability, and obtain the mineral dust composition.

Finally, an important link between the LC rejected values and the particle size distribution was attributed. This result leads us to solve the retrieval problem by solving the RTE equation and in the future find an a priori for the effective radius and VMR. First, we briefly studied the sensitivity of aerosol parameters using ARAHMIS code. Then, we reproduced two IASI observations, one above the desert and the other of a mineral dust. The next step is to inverse the mineral dust fit to retrieve the parameters in question.

GENERAL CONCLUSION AND PERSPECTIVES

The atmosphere is formed by gaseous species, clouds, and aerosols from different sources, primarily from deserts. Recently, more efforts were made to quantify their impacts on the Earth's thermal balance, climate, and human health. Significant progress has been made by satellite remote sensing instruments better to understand aerosols emission, dispersion, and impacts, but many questions remain open, especially in composition quantification. Due to the difficulty to properly represent the spectral surface emissivity, spaceborne sensors remain limited in detecting aerosols above land. To better understand these observations, a perfect knowledge of the optical properties of aerosols is also necessary. This objective has led us to develop a new methodology to correct the LSE and optimize IASI observations. Then, we used new experimental optical properties and linked them with the dust mineralogical composition. This thesis has brought new knowledge about the chemical composition from IASI measurements using laboratory optical properties. We were able to bring quantitative information about airborne dust composition using a spaceborne remote sensing instrument.

First, we found that dust detections above land were highly affected by LSE. Soil rich in quartz generates the Reststrahlen phenomenon, altering the IASI observation and causing false aerosol detection and characterization. A mean monthly emissivity dataset was previously used to solve this problem. However, the direct use of these data can strongly change the spectral detection, losing aerosol signals. To achieve the first objective of this thesis, a new LSE optimization method was developed using the same data and based on the Reststrahlen feature at 1159 cm^{-1}. A correction factor was calculated and applied to the IASI detection spectra. This method improved the surface emissivity representation and thereby the aerosol detections without altering the mineral dust

information from both day and night observations. This was demonstrated on two case studies with different temporal and seasonal characteristics, which shows the ability to apply the LSE correction method to different situations.

Second, a new method was applied to the laboratory optical properties of Gobi dust samples having external mixture state, and new mineralogical mass weights were obtained. The IASI optical thickness was derived from the radiances showing the same spectral features as laboratory measurements. This result leads to applying the method on the IASI optical thickness spectra of two East Asian dust storms, giving us new information about aerosol composition. Results were consistent with the literature data, particularly with the clay fractions' composition. In addition, we could trace dust sources by comparing them with HYSPLIT trajectories. Hence, we attained the second and third objectives by linking new optical properties to the chemical composition and using it in remote sensing detection from IASI to characterize the mineralogical composition of airborne dust.

One of the strengths of this work, is the use of the IASI which has global coverage, day and night detections with a high spectral resolution, owing the capability to detect mineral dust. The correction of IASI spectra from the new LSE methodology leads to reliable quantification of aerosol properties.

Also, we directly used the extinction coefficients in the LC method without making assumptions on the particles' shape, that presents until now a complex parameter to quantify. Typically, mineralogical measurements are performed on dust samples or aerosol particles generated from parent soils in laboratory. We were able to quantify the aerosol composition directly from dust plumes using satellite detections and laboratory spectral measurements. This work fills the gap of the aerosol chemical properties retrieval directly from uplifted dust in the atmosphere.

We considered in this study only major minerals in East Asia without taking into consideration minor minerals i.e., hematite which is known to be an important species in Saharan dust storms. In addition, hematite is not detectable in the TIR band and its spectral features rely in FIR. Therefore, it is interesting in the future to apply the LC method on another satellite sensor e.g., Far-infrared Outgoing Radiation Understanding & Monitoring (FORUM) which will interestingly also cover the far-infrared (from 100 to 667 cm⁻

[1]), never before sounded in its entirety from space. The mission will start in 2027 (https://www.forum-ee9.eu).

This study showed external mixtures of dust samples, however internal mixtures should be taken into consideration in many other cases. The *effective medium theory* can be used to better estimate the extinction for inhomogeneities in internal mixtures *(Liu et al., 2014)*.

As shown in Chapter III, results are close to literature mineralogy for clay-sized particles. Solving the LC equations lead to have up to 15% of rejected values which were negative values of tectosilicates mass weights, these particles tend to be silt. Hence, it is important to consider the size distribution and retrieve its value. In the future, we will use IASI detections with the laboratory optical properties to retrieve the aerosol microphysical properties (SD, concentration) using ARAHMIS code developed in LOA from the optimal estimation method.

The work done during this thesis is published in *Remote Sensing MDPI* journal and presented in different international conferences and seminars (see **Appendix A and B**).

Appendix A

Article

Aerosol Mineralogical Study Using Laboratory and IASI Measurements: Application to East Asian Deserts

Perla Alalam [1], Lise Deschutter [1,2], Antoine Al Choueiry [3], Denis Petitprez [2] and Hervé Herbin [1,*]

[1] Laboratoire d'Optique Atmosphérique, LOA, UMR 8518, CNRS, Université de Lille, F-59000 Lille, France; perla.alalam@univ-lille.fr (P.A.); lise.deschutter@univ-lille.fr (L.D.)

[2] Physicochimie des Processus de Combustion et de l'Atmosphère, PC2A, UMR 8522, CNRS, Université de Lille, F-59000 Lille, France; denis.petitprez@univ-lille.fr

[3] Laboratoire des Biomatériaux and des Matériaux Intelligents, LBMI, Université Libanaise Faculté des Sciences II, Jdeidet P.O. Box 90656, Lebanon; antoine.choueiry@ul.edu.lb

[*] Correspondence: herve.herbin@univ-lille.fr

Abstract: East Asia is the second-largest mineral dust source in the world, after the Sahara. When dispersed in the atmosphere, mineral dust can alter the Earth's radiation budget by changing the atmosphere's absorption and scattering properties. Therefore, the mineralogical composition of dust is key to understanding the impact of mineral dust on the atmosphere. This paper presents new information on mineralogical dust during East Asian dust events that were obtained from laboratory dust measurements combined with satellite remote sensing dust detections from the Infrared Atmospheric Sounding Interferometer (IASI). However, the mineral dust in this region is lifted above the continent in the lower troposphere, posing constraints due to the large variability in the Land Surface Emissivity (LSE). First, a new methodology was developed to correct the LSE from a mean monthly emissivity dataset. The results show an adjustment in the IASI spectra by acquiring aerosol information. Then, the experimental extinction coefficients of pure minerals were linearly combined to reproduce a Gobi dust spectrum, which allowed for the determination of the mineralogical mass weights. In addition, from the IASI radiances, a spectral dust optical thickness was calculated, displaying features identical to the optical thickness of the Gobi dust measured in the laboratory. The linear combination of pure minerals spectra was also applied to the IASI optical thickness, providing mineralogical mass weights. Finally, the method was applied after LSE optimization, and mineralogical evolution maps were obtained for two dust events in two different seasons and years, May 2017 and March 2021. The mean dust weights originating from the Gobi Desert, Taklamakan Desert, and Horqin Sandy Land are close to the mass weights in the literature. In addition, the spatial variability was linked to possible dust sources, and it was examined with a backward trajectory model. Moreover, a comparison between two IASI instruments on METOP-A and -B proved the method's applicability to different METOP platforms. Due to all of the above, the applied method is a powerful tool for exploiting dust mineralogy and dust sources using both laboratory optical properties and IASI detections.

Keywords: remote sensing; mineral dust; aerosols; laboratory measurements; optical properties; chemical properties; land surface emissivity; mineralogical extinction weight

1. Introduction

Mineral dust is the product of wind erosion of the land surface in arid and semi-arid regions [1]. Due to its essential impact on the climate system, more attention has been paid to mineral dust, which plays a fundamental role in air quality [2]. Moreover, climate change and desertification amplify global dust emissions in the atmosphere [3]. Dust can directly perturb the radiative flux by interacting with solar and thermal radiation through absorption and scattering processes [4]. It can also indirectly affect clouds, ice formation,

and nucleation [5]. Climate alteration depends on the physicochemical properties of dust, since the forcing effect is associated with dust mineralogical composition changes in the atmosphere [6]. The sulfuric acid coating can affect ice nucleation, depending on the mineral composition of dust [7]. In addition, iron solubilization depends on the dust mineralogy, and it is mainly linked to the presence of clay minerals [8].

Mineral dust presents one of the most abundant sources of Particulate Matter (PM) originating from natural sources in the atmosphere [9]. In particular, East Asia can produce up to 800 Tg y^{-1} of mineral dust [10], with the most frequent dust storms occurring in springtime [11]. The Gobi Desert, Taklamakan Desert, and nearby plateaus are considered the primary dust sources in Asia [12]. Dust masses are transported downwind from Mongolia and China [13], crossing the Korean Gulf and Japan [14] to the Pacific Ocean until they reach the North American continent [15], and sometimes reaching Europe [16]. One of the particularities of this region is the diversity in its mineralogical composition; the dust is rich in silicates and carbonates, which are considered source tracers in East Asia [17].

Previous studies have analyzed desert dust mineralogical properties from East Asia using experimental methods, i.e., geochemical tracing methods, to link dust mineralogy and sources depending on the geology [18]. Scanning Electron Microscopy (SEM) was used to exploit the quartz and illite/quartz ratio contents and link them to particle size distribution [19]. In addition, using X-ray Diffractometry (XRD), it was proven that, from West to East Asia, the calcite content decreases and the feldspar content increases [20]. Moreover, dust optical properties derived from Fourier transform infrared spectrometry (FTIR)—extinction coefficient spectra—exhibited mineralogical fingerprints showing chemical information about different desert dust sources [21].

Satellite instruments detect dust plume distribution and evolution at a global scale, e.g., lidars. Cloud-Aerosol Lidar with Orthogonal Polarization (CALIOP) based on the CALIPSO satellite, provide dust altitude and layer thickness information [22]. In addition, multispectral radiometers can outline dust plume evolution, e.g., the geostationary satellite HIMAWARI 8 RGB imager [23] and the Moderate Resolution Imaging Spectroradiometer (MODIS), which also differentiates natural dust from anthropogenic dust with lower Aerosol Optical Depth (AOD) values [24]. Furthermore, spectrometers with high spectral resolution allow for quantifying aerosol parameters such as the effective radius from the Atmospheric Infrared Sounder (AIRS) [25] and the Infrared Atmospheric Sounding Interferometer (IASI) [26].

Until now, no mineralogical aerosol information has been investigated from satellite spectrometers. This may be due to the challenges posed by the lack of experimental optical properties of pure minerals and dust, as well as the encountered satellite remote sensing limitations. The latter includes cloud coverage, which can mask aerosol detections, and the land surface effect, which contaminates observations. In particular, East Asian dust is uplifted near the surface in the troposphere above the continent [27], where the Land Surface Emissivity (LSE) variability affects remote sensing detection [28]. This presents a primary error source, as it impacts clear sky and dust layer detection above the land [29].

This work investigates the capability of IASI spectra to provide the composition of mineralogical dust using the optical properties of pure minerals found in the laboratory. In Section 2, the IASI instrument is demonstrated to have different advantages in infrared detection. We also discuss the false IASI dust detection caused by the LSE and the use of a mean monthly emissivity atlas that can underestimate or overestimate the IASI radiances. Then, we introduce a new LSE correction method to optimize the LSE dataset; a new diagram scheme is presented with the optimization equations. Next, we determine the optical thickness spectrum derived from IASI radiances, and we use it to verify the LSE optimization method. In Section 3, we present new experimental optical properties (i.e., the extinction coefficient spectra) measured using Thermal Infrared (TIR) data for Gobi dust and pure minerals (quartz, illite, and calcite). An effective extinction coefficient is simulated using a linear combination of the pure mineral extinctions spectra to reproduce both the Gobi dust spectrum and IASI dust detection. In Section 4, laboratory measurements are

137

compared to the IASI optical thickness, showing the same molecular features. Finally, we couple the IASI optical thickness with a linear combination of pure mineral spectra to compute the mineralogical dust mass weights. In Section 5, we apply the method to a dust storm that occurred between 3–7 May 2017, using IASI observations based on METOP-A. Finally, we summarize the work by comparing the results with METOP B and a second dust event between 14–22 March 2021.

2. Gobi Dust Detection from Satellite Remote Sensing

2.1. IASI

The IASI instrument is a central element of the METOP satellite series launched by the European meteorological polar orbit. Developed by CNES and in cooperation with EUMETSAT, three sun-synchronized METOP satellites (-A, -B, and -C) have been dispatched in the last 15 years with IASI-A, -B, and -C on board, and in the next 20 years, a new generation of IASI-NG will continue the IASI mission with increased resolution and radiometric performance [30]. The instrument scans in nadir view with a swath of 2200 km. Each field of view corresponds to 2×2 circular pixels, each with a 12 km diameter footprint in nadir. The IASI covers a continuous infrared spectral range between 645 and 2760 cm^{-1} (3.62 and 15.5 µm) and provides 8461 channels with a high spectral resolution of 0.5 cm^{-1} and low radiometric noise [31]. In addition, IASI has shown high-stability performance over time, with 1.8 million atmospheric detections per day above the Earth's surface [32]. It was fundamentally developed for meteorological operations and atmospheric gas estimation [33,34]. Recently, studies have proven the use of IASI spectral detections in aerosol applications [26,35]. However, few have been exploited due to the lack of optical property references that are a fundamental element in aerosol characterization.

Figure 1 shows three IASI detection examples of a clear sky above the sea, clear sky above the desert, and mineral dust. An observation of a clear sky above the sea with a negligible LSE contribution shows a flat brightness temperature spectrum in the atmospheric windows (780 to 980 cm^{-1} and 1070 to 1210 cm^{-1}). Conversely, the detection of a clear sky above the desert has high LSE variability that is characterized by a peak at 1159 cm^{-1}, with a lower shift in its brightness temperature between 1069 and 1250 cm^{-1}. These two features appear due to a high reflectance phenomenon called the 'Reststrahlen Effect' that occurs on surfaces rich in quartz and arises from coherent oscillations of vibrational optical phonon modes [36]. It is triggered by a sudden drop in the real refractive index value [37]. As the real part becomes smaller than the imaginary part, the reflectance increases to a value of 1, which results in a quartz-rich surface decreasing in the LSE to values of less than 1 in the Reststrahlen region.

Dust is detectable in the atmospheric window, where only narrow gas bands are exhibited. It produces a 'V shape' and the LSE signal can affect the spectrum when detections are above the desert. Carbon dioxide, ozone, and water vapor enhance wide absorption bands (displayed in shaded gray in Figure 1) as well as narrow absorption bands in the spectra [33]. For simplicity, the wide bands are removed from the IASI spectra discussed in the next graphs. IASI dust spectra are selected by applying conditions to the difference in the brightness temperature ΔT_B, which is calculated by subtracting two brightness temperature values T_{B,v_1} and T_{B,v_2} for two wavenumbers v_1 and v_2 respectively, and is written as follows:

$$\Delta T_B = T_{B,v_1} - T_{B,v_2} \tag{1}$$
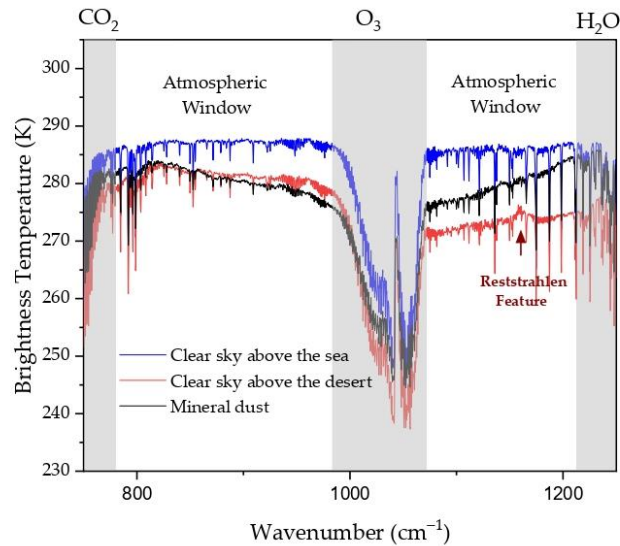
Figure 1. IASI detection spectra of a clear sky above the sea (in blue), a clear sky above the desert (in red) with a Reststrahlen feature, and mineral dust above the desert (in gray). Carbon dioxide, ozone, and water vapor absorption bands are presented in patterned regions, masking atmospheric detection.

In this study, two brightness temperature differences were considered for dust selection: $\Delta T_{B1} = T_{B,809.25} - T_{B,988}$ and $\Delta T_{B2} = T_{B,1191.25} - T_{B,1112}$. Particular wavenumber values were selected to prevent the selection of narrow water vapor bands in the spectrum. Without considering an LSE correction, the dust selection can be misleading, as mineral dust detection can be more likely inclined due to the surface signal, especially in the band where the Reststrahlen region is present. Figure 2a shows the IASI dust selection (ΔT_{B1} and ΔT_{B2}) during a Gobi dust storm on 4 May 2017 at 3:00 UTC; however, to visualize and study the surface effect, only ΔT_{B2} is illustrated. A false dust detection in the dashed black circle was selected, while the same region detected by MODIS showed a negligible daily average AOD (Figure 2b). The false detection and selection from the IASI spectra are related to the LSE constraints.
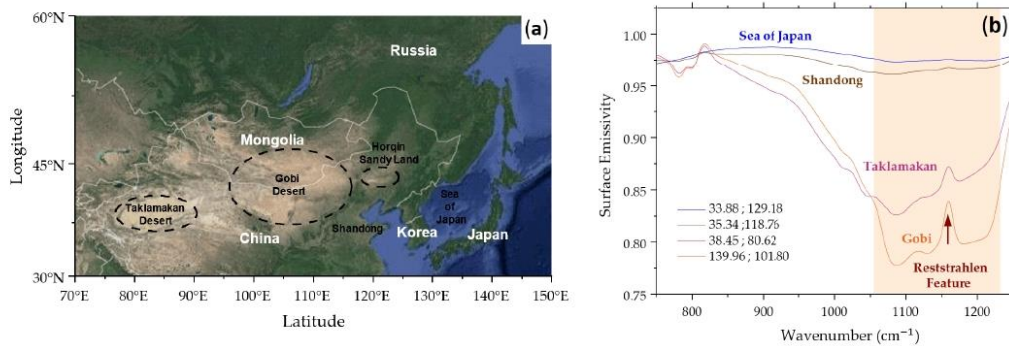
Figure 3. (**a**) Topographic map of East Asia region with dashed black circles around the main desert sources; (**b**) mean monthly surface emissivity of four different surfaces during the month of May (Adapted with permission from Ref. [44], 2021, Daniel Zhou). The shaded orange box indicates the Reststrahlen region.

The direct use of this dataset can underestimate or overestimate the spectral observation, and this can be due to the LSE variability caused by diurnal and seasonal cycles, the satellite viewing angles, or surface type variation [45]. The correction is expected to reproduce a clear sky spectrum above the sea. This is not the case in the example shown in Figure 4. with an over correction of a desert spectrum in green. The brightness temperature is strongly altered after applying the correction at 1059 cm^{-1}, resulting a trough instead of the Reststrahlen peak and a higher shift in the brightness temperature between 1069 and 1250 cm^{-1} instead of a flat clear sky above the sea detection. This result indicates that the direct use of the dataset can amplify the LSE correction and alter the atmospheric information in question. Hence, optimization of the LSE is crucial to finding an optimal aerosol quantification. As a result, establishing the surface contribution and removing it from satellite observations remains challenging.
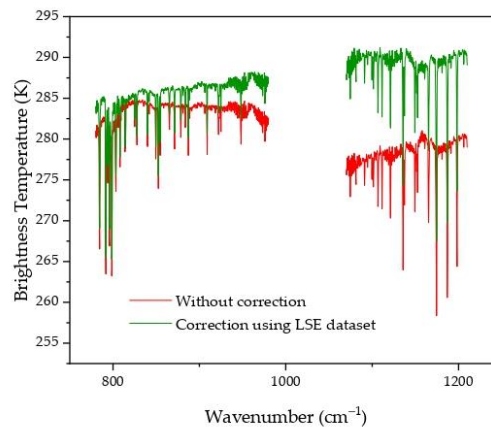
Figure 4. Brightness temperature desert spectrum example before and after the LSE correction using a monthly average emissivity value (Adapted with permission from Ref. [44], 2021, Daniel Zhou).

2.2. Surface Emissivity Optimization Method and Dust Spectral Selection

The intensity of the Reststrahlen feature is proportional to the particle size. As the mean particle diameter decreases, the surface scattering increases, resulting in increased absorption energy and hence a lower reflectance [46]. Based on this, the Reststrahlen feature can be used as a surface effect indicator; it is highly visible on desert surface detections compared to airborne dust. Therefore, in order to optimize the LSE effect on IASI radiances, a new methodology was developed by calculating the Reststrahlen relative value $X_{m(v)}$ of a spectrum $m(v)$ for both the IASI spectral radiance and the mean monthly emissivity value at the same pixel. The method expresses the relative value between the observed spectrum with the Reststrahlen effect $m_{w/}(v_R)$ at the Reststrahlen wavenumber $v_R = 1159$ cm^{-1} and the expected value of the observation spectrum without the Reststrahlen effect $m_{w/o}(v_R)$ and it is written as follows:

$$X_{m(v_R)} = \frac{m_{w/}(v_R) - m_{w/o}(v_R)}{m_{w/o}(v_R)} \tag{2}$$

where $m_{w/o}(v_R)$ is computed by solving a linear function of the form $y = ax + b$ calculated in the neighboring Reststrahlen feature and taking into consideration the narrow gas bands.

Then, we define the emissivity correction factor C as follows:

$$C = \frac{X_{L(v_R)}}{X_{\varepsilon(v_R)}} \tag{3}$$

With C being the ratio between the Reststrahlen relative value for the spectral radiance detection $X_{L(v_R)}$ and the Reststrahlen relative value for the mean monthly emissivity spectrum $X_{\varepsilon(v_R)}$ for the same detected grid, both calculated by Equation (2).

The corrected surface emissivity $\varepsilon_C(v)$ is estimated from the mean monthly surface emissivity $\overline{\varepsilon}(v)$ and the correction factor C, and it is written as follows:

$$\varepsilon_C(v) = 1 + C(\overline{\varepsilon}(v) - 1) \tag{4}$$

The correction in Equation (3) is calculated when a significant Reststrahlen effect is present. A minimum condition is applied to the $m_{w/}(v_R) - m_{w/o}(v_R)$ value of both the radiance and emissivity spectra. A particular case is applied to the detection of concentrated dust layers and saturated clouds in which the surface is masked and no emissivity correction is taken into consideration. The correction factor C is 0; hence, the corrected surface emissivity ε_C is 1. The saturated cloud spectra are characterized by having a CO_2 brightness temperature peak 668 cm^{-1} higher than the O_3 peak at 1044 cm^{-1}. However, when the LSE variability is small, the Reststrahlen wavenumber $\overline{\varepsilon}(v_R)$ approaches 1. In this case, the correction factor C equals 1, and the literature dataset is directly used $(\varepsilon_C(v) = \overline{\varepsilon}(v))$. After solving Equation (4) to obtain the optimized emissivity $\varepsilon_C(v)$, the corrected spectral radiance $L_c(v)$ is calculated. The dust spectra are then selected by converting the radiance to the brightness temperature $T_{Bc}(v)$ spectra and applying conditions to ΔT_{B1} and ΔT_{B2} (defined in Section 2.1). Figure 5 illustrates the flowchart of the optimization method described.

141
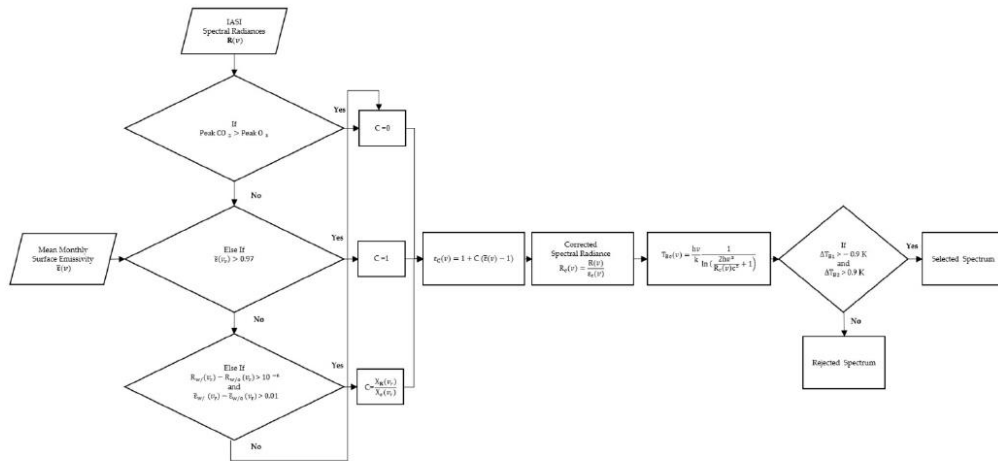
Figure 5. LSE correction scheme diagram.

In Figure 6, the optimization method is applied to two IASI observation examples, detections of a clear sky (in red) and mineral dust (in gray) above the desert. The green spectrum shows that all the effects dominated by the Reststrahlen phenomenon are removed from the clear sky above the desert, as if a clear sky above the sea (in blue) was detected after the correction. The peak at 1059 cm^{-1} was optimized and the lower shift between 1069 and 1250 cm^{-1} was flattened. In contrast, the modification in the mineral dust detection (in black) was minimal, with the dust spectral signature maintaining a 'V-shaped' brightness temperature.
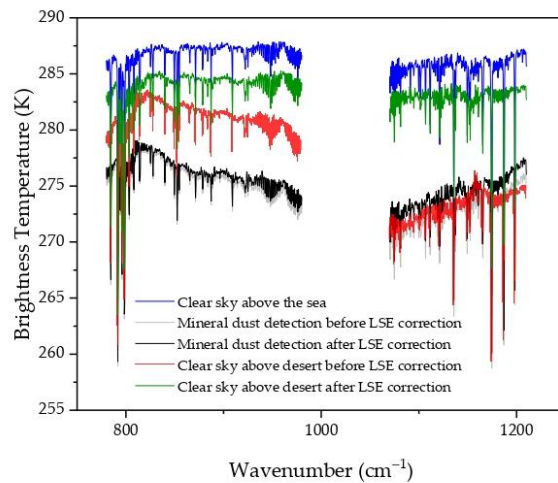
Figure 6. IASI spectral detection example for a clear sky above the sea compared to a clear sky above the desert and mineral dust detection before and after LSE optimization.

2.3. IASI Optical Thickness

The radiative transfer equation depends on the surface emission, the absorption in the atmosphere, and the surface reflection and scattering. In particular, the thermal window region of the spectrum is the primary contributor to the measured radiance and comes from the surface emission, and it is written as follows:

$$R(v) = \varepsilon(v)B(v, T_S)e^{-\int_0^H k_v(h)dh} \tag{5}$$

where the spectrum $R(v)$ is a function of the surface emissivity $\varepsilon(v)$, the surface temperature T_s described by the Planck function $B(v, T)$, and the total extinction k_v of the atmospheric layers of thickness H, containing gases, aerosols, and clouds.

Consider a homogeneous and stratified dust layer of thickness L. The Beer–Lambert law can be applied to this dust layer. For an incident spectral radiance $R_0(v)$ at wavenumber v, the attenuated amount of $R_{obs}(v)$ passing through a dust layer of thickness L has an extinction coefficient $K_{ext}^{aerosol}(v)$ resulting from the absorption and scattering, and it is written as follows:

$$R_{obs}(v) = R_0(v)e^{-k_{ext}^{aerosol}(v)L} \tag{6}$$

The incident spectral radiance $R_0(v)$ represents a clear sky spectrum above the sea where $R_0(v) \geq R_{obs}(v)$. The spectrum is selected from the same observation date with the sea detection nearest to the dust observation.

From IASI radiances, we can calculate the optical thickness $\tau(v)$, and this is obtained by the natural logarithm of the ratio of a clear sky spectral radiance $R_0(v)$ and a spectral radiance observation $R_{obs}(v)$:

$$\tau(v) = \ln\left(\frac{R_0(v)}{R_{obs}(v)}\right) \tag{7}$$

This ratio becomes independent from the Planck function $B(v, T_s)$ by subtracting it in the calculation, and unconstrained by the surface emissivity after applying the LSE optimization method discussed above. What remains in the equation is the aerosol extinction multiplied by the layer thickness L with an error ϵ_{Re}, which includes noise and the remaining residue of gas present in the spectrum. Thus, Equation (7) is written as follows:

$$\tau(v) = \ln\left(\frac{e^{-k_{ext}^{gases}(v)\cdot H}}{e^{-k_{ext}^{gases}(v)\cdot H - k_{ext}^{aerosol}(v)\cdot L}}\right) = k_{ext}^{aerosol}(v)L + \epsilon_\tau \tag{8}$$

Equation (8) has been applied to the example spectra shown in Figure 6. Before the LSE correction of the clear sky detection above the desert, the optical thickness spectrum has an extinction coefficient of a land surface, i.e., a sand surface contaminated by the Reststrahlen effect (Figure 7a). After the LSE correction, only the optical thickness approaches zero with no aerosol features. This indicates that the spectral signal comes entirely from the land surface. However, merely a minor optimization affected the optical thickness of the mineral dust detection above the desert (Figure 7b) with an aerosol extinction signal remaining. This result verifies that the LSE optimization method corrected only land surface signals without removing the aerosol fingerprints that present crucial data to quantify the aerosol physicochemical properties.
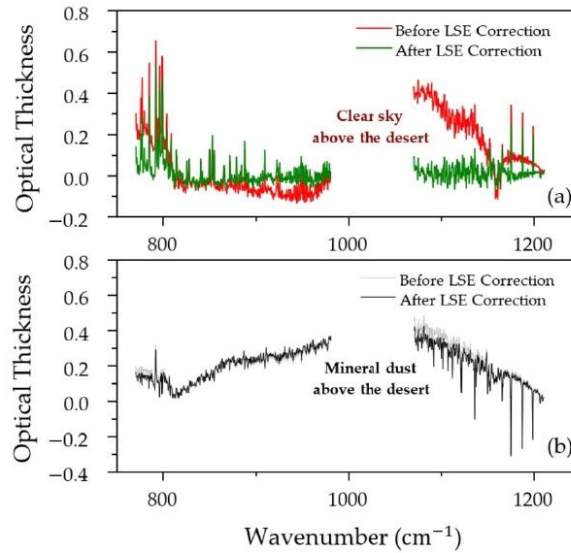
Figure 7. Example optical thickness spectra of (**a**) a clear sky above the desert and (**b**) mineral dust above the desert before and after LSE correction.

2.4. Cloud Selection

East Asia is also characterized by high coverage of clouds that can mask aerosol detection. The cloud selection was computed using a principal component analysis (PCA) code developed in Laboratoire d'Optique Atmosphérique (LOA) [47]. An example is shown in Figure 8a for IASI detection, where clouds (in gray) mixed with the dust plume and separated the detection into four different loads. IASI detection and selection are consistent with the RGB image in Figure 8b showing geostationary HIMAWARI 8 RGB imagery, where thin high clouds (in olive color) contaminated the plume into four different aerosol sections (in pink). The IASI map with a Mercator projection shows homogeneous cloud selection with the same morphology but with a different projection than the HIMAWARI 8 imagery, which has a polar projection. The inverted 'L-shape' cloud selection from the IASI map has the same shape in the imagery but is elongated. This comparison indicates the consistency of the IASI cloud and the dust selections.

144

Dust **Thick High Cloud** Thick Mid Cloud Cold Low Cloud Cold Desert Cold Land
Ocean **Thin High Cloud** Thin Mid Cloud Warm Low Cloud Warm Desert Warm Land
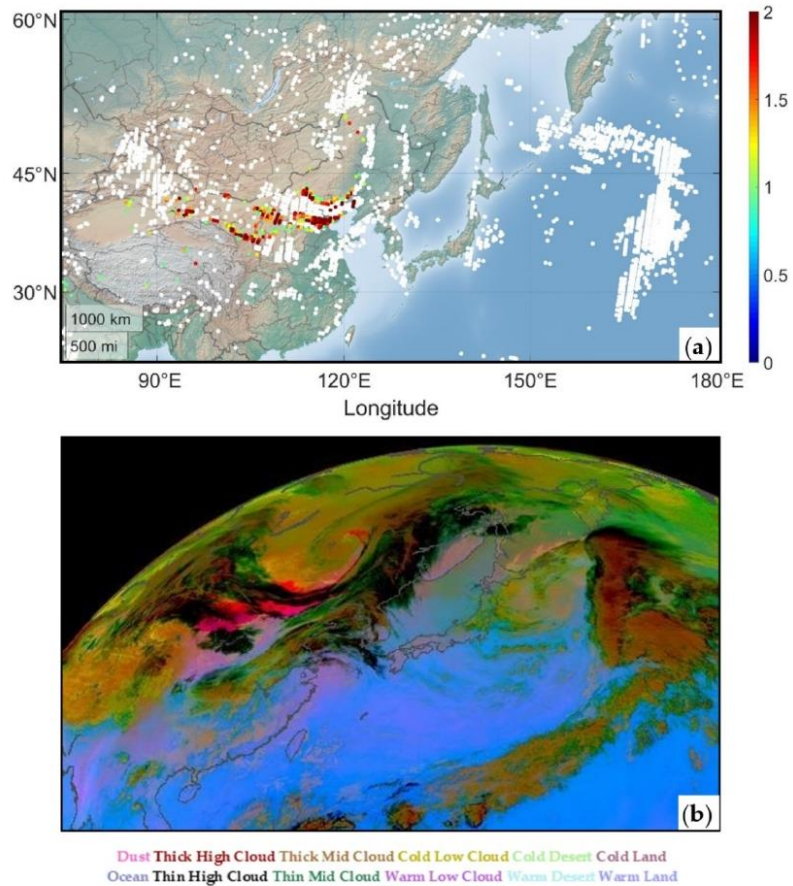
Figure 8. (**a**) IASI dust and cloud selection on 15 March 2021; (**b**) RGB Dust False-like SEVIRI from HIMAWARI (www.icare.univ-lille.fr, accessed on 1 December 2021).

Finally, the methodology was applied to the same detection example of the 2017 dust storm on May 4 previously presented in Figure 2a, before the LSE correction, and it is plotted in Figure 9a, after the LSE correction. The selection above the Taklamakan desert is eliminated and a minor change can be seen in the dust plume that originated from the Gobi Desert. The dust selection after LSE optimization and approved with CALIOP-attenuated backscattering at 532 nm is shown in Figure 9b. A thick aerosol layer was detected in the low troposphere between 1 and 3 km. Hence, an optimized LSE correction and dust selection were established without dust signal elimination. Therefore, by using the new LSE method, dust selection was established considering cloud detection.
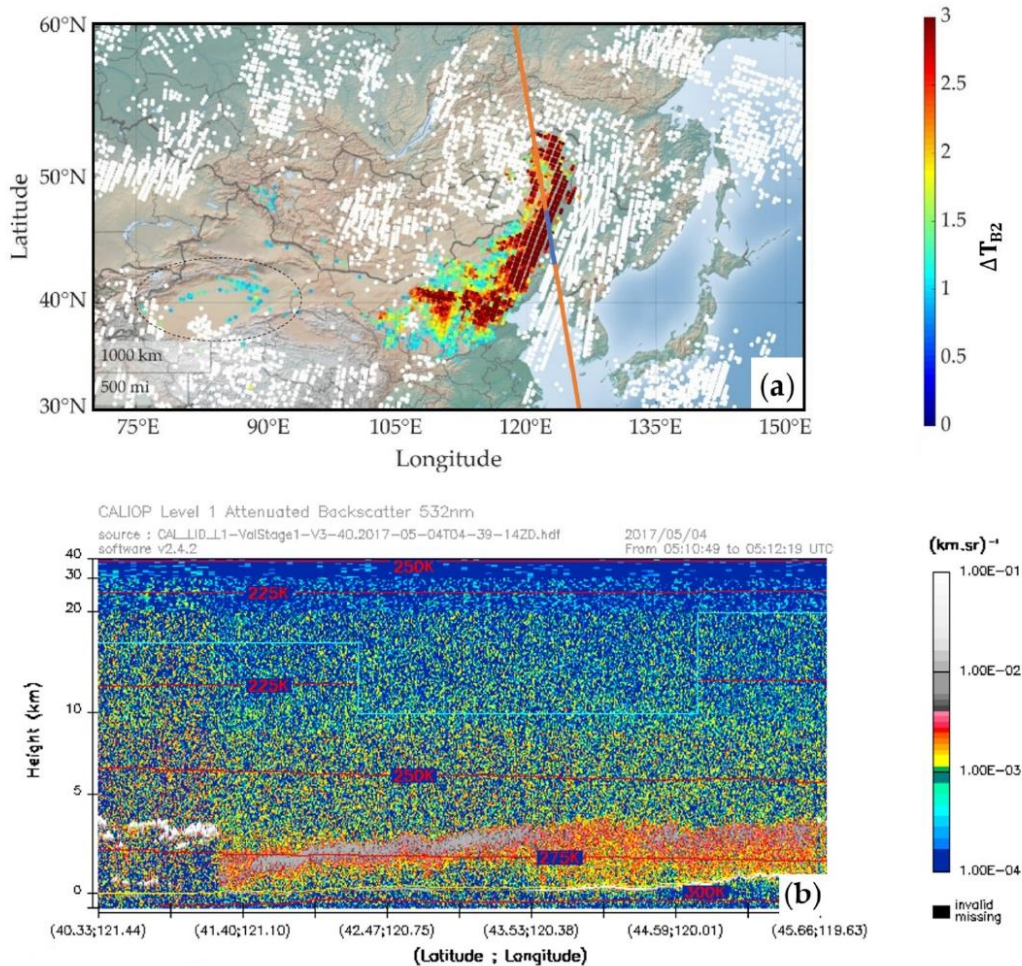
Figure 9. (**a**) The difference in the brightness temperature of the IASI dust selection after LSE optimization during the dust storm on 4 May 2017, in daytime. The dashed black circles present the removed false aerosol detection region. The orange line is the CALIOP orbit track, and the blue line is the CALIOP viewing section; (**b**) CALIOP-attenuated backscatter at 532 nm (www.icare.univ-lille.fr, accessed on 27 November 2021).

3. Experimental Laboratory Data

3.1. Gobi Mineralogical Dust Composition

In general, mineral dust is composed of both silicates and carbonates. One of the major mineralogical families is the phyllosilicates group (including illite, kaolinite, and smectite), which is abundant in Asian dust, with a dominance of illite [17]. Members of the tectosilicates group, i.e., quartz and feldspars, form 75% of the Earth's crust and appear in desert dust samples. The carbonate family contains calcite and dolomite, which are considered tracers of East Asian dust [48].

A study provided an estimate of the global mineralogy of a soil and airborne dust dataset based on 120 soil units of clay and silt fraction. In airborne dust, phyllosilicates were abundant, with 74.6% of the weight mass and illite, kaolinite, and smectite as the major minerals. Quartz and feldspars were minor, with an average of 4.9% and 3.7%, respectively. Calcite represented 8.9% of the total weight mass, and minor minerals represented 8.1% [49].

3.2. Extinction Coefficient Spectra and Molecular Assignments

The laboratory setup and experimental procedure are described in detail in the references [50,51], and are only summarized herein. The experimental study was performed by two laboratories: PhysicoChimie des Processus de Combustion et de l'Atmosphère (PC2A) and Laboratoire d'Optique Atmosphérique (LOA). The analyzed samples included pure quartz crystal, pure amorphous illite, and pure calcite crystal [52], in addition to the analysis of Gobi dust samples that were collected in Yanchi, Ningxia province in China (107.475211°E, 36.487333°N) [53]. Sample particles (5 g of mass) were placed in suspension by maintaining mechanical agitation using a magnetic stirrer. Using a mass flow controller set at 2 L·min^{-1}, the particles were carried by pure nitrogen gas into a buffer volume to ensure homogeneous aerosol flow and then into two consecutive spectrometer setups. The first was a Fourier transform infrared spectrometer with a 10 m multipass cell, which measured the extinction coefficient in the spectral range between 650 and 9000 cm^{-1}. The second was a UV-visible spectrometer with a 1 m cell measuring extinction coefficients between 10,000 and 40,000 cm^{-1}. At the exit of the cell, a scanning mobility particle sizer (SMPS) and an aerodynamic particle sizer (APS) were simultaneously used to record the size distribution generated by the apparatus between 100 nm and 20 μm. Only TIR spectra were used in this study between 750 and 1250 cm^{-1} in the atmospheric window corresponding to the aerosol detection.

The extinction coefficient of the Gobi dust sample in Figure 10a shows absorption peaks identical to the peaks of the pure mineral extinction coefficients of quartz, illite, and calcite illustrated in Figure 10b [52]. These extinction coefficients present a measurement of each individual mineral and were normalized to remove the dependency on concentration. These optical properties are in accordance with the mineralogy in the literature, where mineral fingerprints show the presence of the three mineral families: tectosilicates, phyllosilicates, and carbonates, with the presence of quartz, illite, and calcite from each family, respectively.
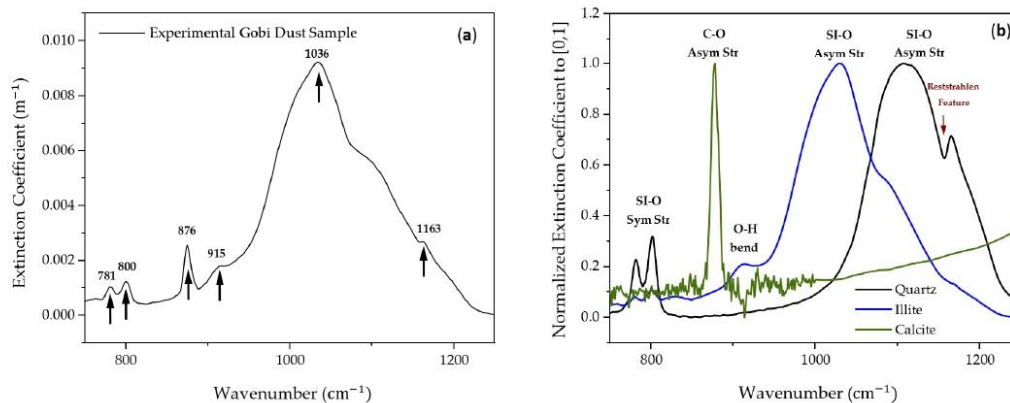
Figure 10. Laboratory extinction coefficient by FTIR of (**a**) Gobi dust samples, with arrows indicating extinction peaks, and (**b**) normalized extinction coefficient to [0, 1] for the pure minerals quartz, illite, and calcite with their molecular assignments (Adapted with permission from Ref. [52]). Sym Str: symmetrical stretching; Asym Str: asymmetrical stretching; Bend: bending.

The most intense bands for quartz from the tectosilicates family are between 1080 and 1177 cm^{-1}, generated by Si-O asymmetrical stretching. The Si-O symmetrical stretching produces a doublet at 778 and 795 cm^{-1} [54,55]. This doublet caused by the same Si-O stretching is also found in phyllosilicates or clay minerals (e.g., illite, kaolinite ...) [56]. The major peak present in the latter group at 1033 cm^{-1} is due to the Si-O asymmetrical stretching. This shift difference with respect to the stretching mode in quartz is explained by cation substitutions, particularly Al^{2+} for Si^{2+}. The peak at 916 cm^{-1} for illite is assigned to the -O-H bending associated with Al, Fe, or Mg cations [57]. The fundamental vibrations of CO$_3$ anions in carbonates (e.g., calcite, dolomite, etc.) show a spectral feature at 885 cm^{-1} of carbonates in TIR caused by C-O asymmetrical stretching [58,59]. Table 1 summarizes the molecular assignments in the active thermal infrared (TIR) of the abundant minerals of the three main mineral groups in desert dust from previous studies.

Table 1. Molecular assignments of some minerals in TIR.

Mineral Group	Mineral Name	Molecular Assignment	Central Wavenumber (cm^{-1})	References
Tectosilicates	Quartz	Si-O Symmetrical Stretching	778, 795	[54,55,60]
		Si-O Asymmetrical Stretching	1080, 1102, 1177	
Phyllosilicates	Illite	-O-H Bending	916	[56,57]
		Si-O Asymmetrical Stretching	1033	
Carbonates	Calcite	-C-O Asymmetrical Stretching	879 to 904	[58,59]

Airborne dust particles occur as a mixture of pure minerals, where the distribution of the molecules can be heterogeneous in the volume of a particle in the case of an internal mixture, or homogeneous in the case of an external mixture. In the case of an external mixture of mineral dust, the optical properties of individual minerals can be used to model the optical properties. An effective extinction coefficient $k_{eff}(v)$ can be obtained from a linear combination (LC) of the individual mineral extinctions [61]. The combination is calculated from the normalized experimental extinction coefficients of quartz $\overline{k}_Q$, illite $\overline{k}_I$, and calcite $\overline{k}_{Ca}$, with an extinction fraction of the mineral groups in question, f_{Tec}, f_{Phy}, and f_{Ca}, respectively, and it is calculated by:

$$k_{eff}(v) = f_{Tec}\overline{k}_Q(v) + f_{Phy}\overline{k}_I(v) + f_{Ca}\overline{k}_{Ca}(v) \tag{9}$$

Figure 11 shows an LC simulation fitted to the Gobi dust spectrum. The individual mineral spectra reproduced a fit with 13.7% of quartz, 79.8% of illite, and 6.5% of calcite to obtain an external mineral mixture spectrum with the remaining residue $\in_{Re}$ from the predicted spectrum $k_{eff}(v)$ and the experimental spectrum $k_{exp}(v)$. The residue difference between the LC simulated spectrum and the Gobi dust spectrum is 2.5%. This result suggests that the Gobi dust sample was made up of external mixtures of minerals, which is in accordance with the SEM experimental results showing external mixtures of this Gobi dust sample [62].
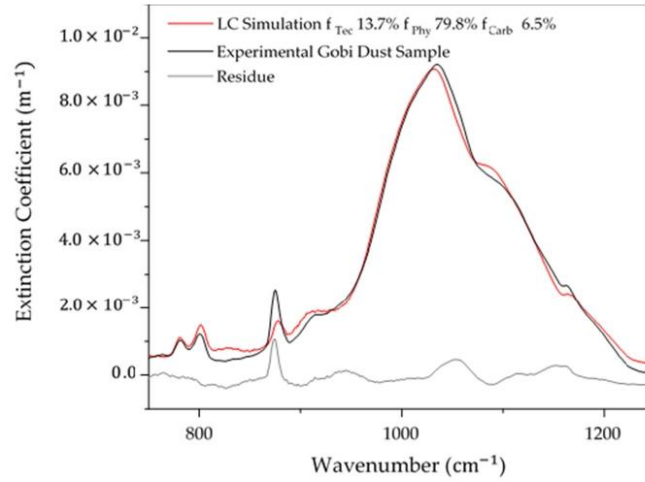
Figure 11. Simulation of the linear combination of pure mineral coefficients (red) fitted with the experimental Gobi dust extinction spectrum (black) with the remaining residue from the simulation and experimental spectrum (gray) and the RMS (light gray envelope).

In order to compare the results with the data in the literature, it is important to convert the extinction weights to mass weights. This can be performed by obtaining the mass extinction coefficient (MEC; $m^2 \cdot g^{-1}$), which can be calculated from the maximum value of the extinction coefficient $k_i^{max}(v)$ divided by the mass concentration MC_i for the mineral i:

$$MEC_i = \frac{k_i^{max}(v)}{MC_i} \qquad (10)$$

where MC_i is obtained from the particle size distribution recorded experimentally by the APS and the SMPS. The densities used in this study for the mineral components quartz (Q), illite (I), and calcite (Ca) were $\rho_Q = 2.65 \text{ g} \cdot cm^{-3}$, $\rho_I = 2.8 \text{ g} \cdot cm^{-3}$, and $\rho_{Ca} = 2.71 \text{ g} \cdot cm^{-3}$, respectively.

Hence, the mass weight w_i is obtained as follows:

$$w_i = \frac{f_i \, MEC_i}{\sum_i f_i \, MEC_i} \qquad (11)$$

Then, by applying Equation (10) to the experimental normalized extinction coefficients, the extinction masses of quartz, illite, and calcite were $MEC_Q = 0.189 \text{ m}^2 \cdot g^{-1}$, $MEC_I = 0.209 \text{ m}^2 \cdot g^{-1}$, and $MEC_{Ca} = 0.187 \text{ m}^2 \cdot g^{-1}$, respectively. Finally, the obtained mass weights from Equation (11) were $w_{Tec} = 15.3\%$, $w_{Phy} = 80\%$, and $w_{Carb} = 4.7\%$, respectively.

The mass weight values of the phyllosilicates and carbonates are in agreement with percentages found by Journet et al., (2014) [49]. However, in this example, the percentage of tectosilicates was more than the average by approximately 8% (for quartz and feldspars).

4. Mineralogical Mapping Method

As defined in Section 2, the optical thickness was derived from the IASI radiance, and it corresponds to the dust extinction coefficient multiplied by a dust layer. Furthermore, it was discussed in Section 3 that the experimental extinction coefficient allows for the identification of spectral assignments. To compare the satellite dust detection to the experimental dust measurements, an example of an IASI optical thickness spectrum of Gobi dust detected

on 4 May 2017 was compared with the laboratory optical thickness spectrum of Gobi dust (Figure 12). The results show spectral signatures identical to the laboratory dust features, which can provide information about the mineral families present in each detection. The C-O asymmetrical stretching allows for the detection of carbonates, and the O-H bending indicates the presence of phyllosilicates. In addition, tectosilicates or phyllosilicates can be distinguished by the Si-O asymmetrical stretching assignment position in the spectrum as it shifts position between the two families. In addition, the Si-O symmetrical stretching reveals the possibility of having either tectosilicates or phyllosilicates in the detection, as the doublets are present at the same wavenumbers for the two groups. Therefore, the use of an experimental dust extinction coefficient allows for the identification of the mineralogical component in the IASI residue and can be used to obtain information about the extinction weights of each mineral family.
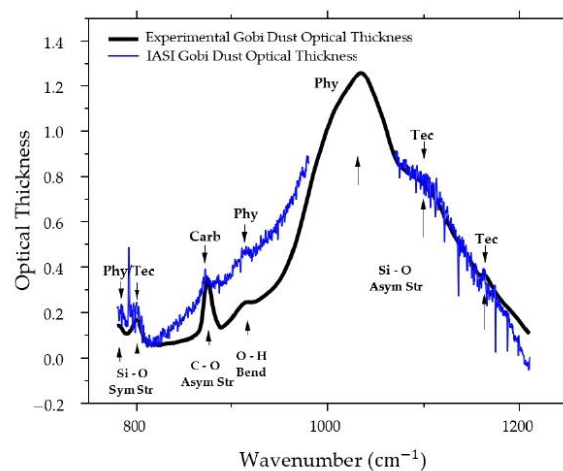
Figure 12. The laboratory Gobi dust spectrum with the molecular assignment for each fingerprint is in black. Sym Str: symmetrical stretching; Asym Str: asymmetrical stretching; Bend: bending. The IASI spectral residue detection of the dust plume on 4 May 2017, at daytime after LSE correction, with mineralogical family assignment, is in blue. Tec: tectosilicates; Phy: phyllosilicates; Carb: carbonates.

Dust sampling depends on the location and the date of the sample collection. This can pose a challenge when it is difficult to collect dust from a particular dust event. To remove this dependency, the linear combination of the pure mineral extinctions of quartz, illite, and calcite described in Section 3 was used to obtain the mineralogical extinction fractions. The equality between the IASI spectral optical thickness $\tau(v)$ from Equation (7) and the linear combination from Equation (9) is solved as follows:

$$\tau(v) = \left[f_{Tec}\overline{k}_Q(v) + f_{Phy}\overline{k}_I(v) + f_{Ca}\overline{k}_{Ca}(v) \right] \times L + \epsilon \tag{12}$$

where the total error ϵ is the sum of the residue error ϵ_{Re} and the error of having other minor families not taken into consideration ϵ_{minor}. The layer thickness L value does not affect the result, as it is considered constant for each pixel.

In Figure 13, Equations (11) and (12) were applied to an example from the May 2017 dust event. The LC method gives 16.8% for tectosilicates, 78.3% for phyllosilicates, and 4.9% for carbonates. The IASI optical thickness shows intense narrow bands of gases, which increases the residue by up to 20%. By removing the gas effect to smooth the fitting, the residue dropped to 5%, indicating a significant error caused by the gases present

150

in the atmosphere. In addition, the percentages calculated are close to the percentages calculated using the experimental spectrum (Section 3), with an increase in the percentage of tectosilicates.
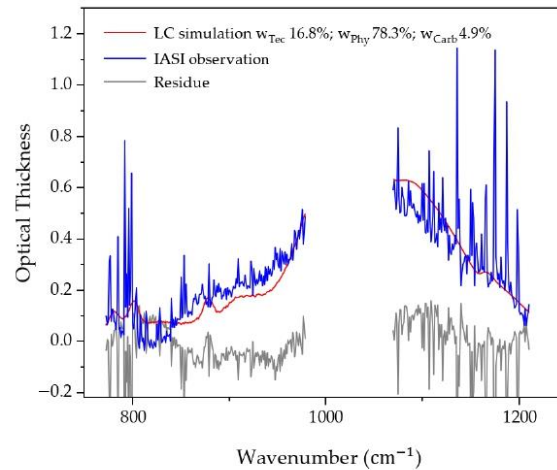
Figure 13. Simulation of the linear combination of pure mineral coefficients (red) fitted with the IASI dust optical thickness (blue) with the remaining residue from the simulation and experimental spectrum (gray) and the RMS (light gray envelope).

5. Case Studies

5.1. May 2017 from IASI-A

An intense dust storm occurred from 3 to 8 May 2017, affecting visibility in North China as dust loads crossed the region. The storm started in the southwest of Inner Mongolia, where the dust plume moved southeastward, passing through North China, the Korean peninsula, and Japan before finally dissipating in Russia. Three cold fronts generated dust during this event. The first two fronts lifted dust from the Gobi Desert on May 3. On May 4, at night, a third front started and different blown dust loads were generated and merged between May 4–6, from both the Horqin Sandy Land and the Gobi Desert [63]. Figure 14 shows the evolution of the dust plume mass weights for tectosilicates, phyllosilicates, and carbonates in May 2017 between May 3–6. In addition to the RMS of the residue using the LC method and the optical thickness at 1072.5 cm^{-1}, no dust plume was detectable by IASI on May 7 and 8. The LC method was applied to this case study with 8% of rejected solutions having negative mass weights. The latter results are linked to the difference in the particle size distribution between the detected dust and the experimental dust used for the LC fitting. Further knowledge of the microphysical dust parameters is essential for better mineralogical estimation. The IASI optical thickness at 1072.5 cm^{-1} shows the homogeneous temporal evolution between the day and night detections. When the optical thickness decreased, the RMS for the residue increased.

151
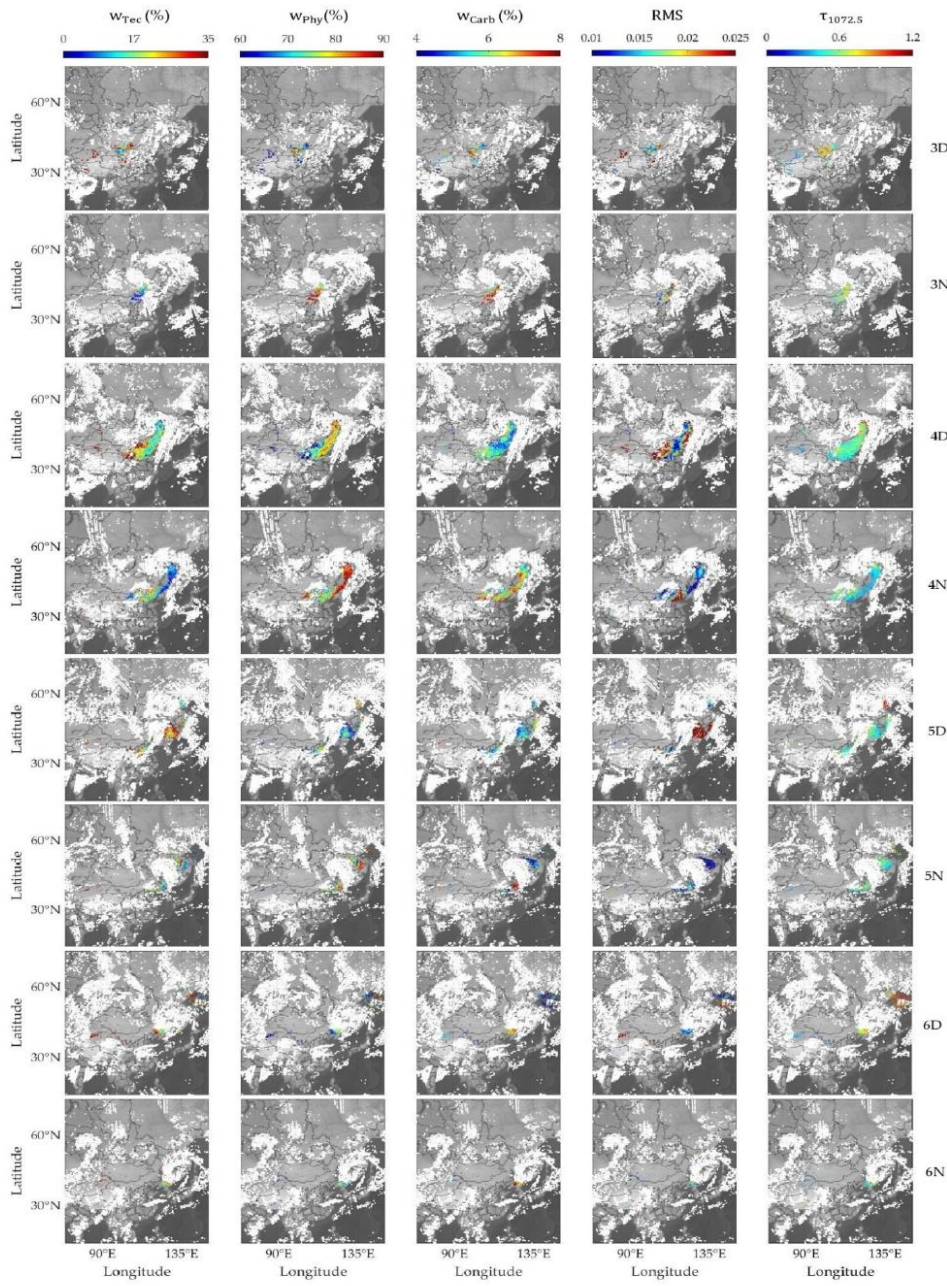
Figure 14. Mineralogical mass weight maps of tectosilicates, phyllosilicates, and carbonates during the 3–6 May 2017 dust storm by day (D) and night (N) from IASI detections.

Wide spatial variability was reported for all the mineral families. This is linked to the diversity of the mineralogical composition in East Asian dust sources. Regionally, from West to East Asia, the carbonate content in the desert soil decreases, and the feldspar content increases [20]. Previously, three broad types of dust sources were identified [64]. Type I deserts are located in topographic lows, such as the Taklamakan Desert; these deserts are associated with fluvial fans [65]. Type II deserts are located on the plateau, with natural dust sources coming from the Gobi Desert of Inner Mongolia. Type III deserts are in dry agricultural areas, e.g., the Horqin Sandy Land, which had a particular influence on this dust storm [63]. Table 2 presents the half-day mean mass weight values, RMS, and the optical thickness at 1077 cm^{-1}.

Table 2. Mean mineralogical values and STD of the three dust type sources in the dust storm of May 2017 in East Asia.

Date	Mean Mass Weight per Half-Day (%)									Mean RMS			Mean $\tau_{1072.5cm^{-1}}$		
	Tec			Phy			Carb								
	I	II	III	I	II	III	I	II	III	I	II	III	I	II	III
3D	52.0	23.5	-	43.0	70.4	-	5.0	6.1	-	0.029	0.018	-	0.357	0.706	-
3N	46.0	10.8	-	48.5	82.3	-	5.5	6.9	-	0.017	0.018	-	0.477	0.631	-
4D	55.4	20.2	-	39.5	74.3	-	5.1	5.5	-	0.029	0.018	-	0.368	0.555	-
4N	50.8	12.5	-	46.1	81.2	-	3.1	6.3	-	0.014	0.015	-	0.574	0.456	-
5D	37.9	20.3	27.5	55.4	74.1	67.3	6.7	5.6	5.2	0.013	0.021	0.033	0.667	0.603	0.515
5N	43.9	17.2	17.2	50.8	76.2	78.6	5.3	6.6	4.5	0.015	0.014	0.008	0.406	0.539	0.529
6D	57.0	23.5	23.4	38.4	69.8	72.9	4.6	6.7	3.7	0.045	0.015	0.016	0.325	0.702	0.916
6N	45.1	23.6	-	51.1	69.5	-	3.8	6.9	-	0.014	0.016	-	0.407	0.516	-
Mean	48.5	19.0	22.7	46.6	74.7	72.9	4.9	6.3	4.4	0.022	0.017	0.019	0.448	0.589	0.653
STD	6.0	4.7	4.2	5.6	4.6	4.6	1.0	0.5	0.6	0.011	0.002	0.011	0.111	0.083	0.186

During this dust event, the mean value of tectosilicates was 48.5% in type I, whereas in types II and III, it was less than half of that. Conversely, the contents of phyllosilicates in types II and III were close to 73% and were 46% in type I. The carbonate content in the three regions had values of around 5.5%.

The hybrid single-particle Lagrangian integrated trajectory (HYSPLIT) model showing 24 h of backward trajectories on May 5 at 11 UTC (Figure 15) validates the sources of these dust masses. The first (I) comes from the Taklamakan Desert. Dust particles are emitted in the region without long-distance transport, and this is explained by the high content of tectosilicates and the lower content of phyllosilicates. The second (II) is created by the Gobi Desert, with the lowest tectosilicate content and the highest carbonate content. The third (III) is a mix from the Gobi and Horqin Deserts. In the example of May 5 during the day (5D), the weight of the tectosilicates strengthened again after a third cold front mixed dust from both deserts since the Horqin Sandy Land is rich in feldspars [20]. Finally, the mean mass weight values of the phyllosilicates and carbonates show results that are consistent with the literature data presented in Section 3, while the tectosilicate content was higher in this study.

153
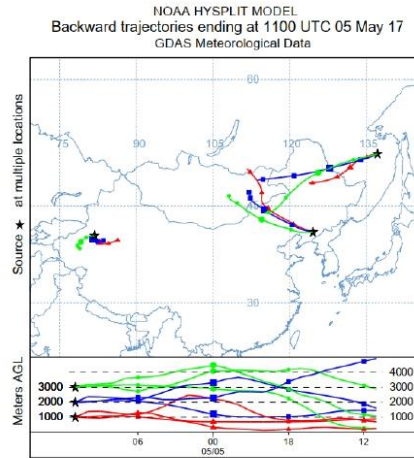
Figure 15. HYSPLIT 24 h backward trajectory for different dust detections in dust storms on 5 May 2017 by night (https://www.ready.noaa.gov/index.php, accessed on 1 December 2021).

5.2. Generalization

5.2.1. IASI-A and IASI-B

METOP-A ended its mission in November and December 2021, and only METOP-B and -C continue the mission [66]. Hence, a comparison between IASI-A and IASI-B is crucial to test the applicability of this study on the present IASI platforms. The comparison was applied to the 2017 case study, where only two METOPs, A and B, were in an orbital phase with a time gap of 45 min, with similar views from both satellites ensuring the maximum daily coverage. The results from 4 May 2017 during the day are shown in Figure 16, with no notable spatial shift between the two platforms as the dust plume traveled slowly from west to east. The plume mineralogical extinction evolution increased consistently in mineral weights after 45 min according to IASI-B, with continuous dust emissions from the Gobi Desert. These results confirm the ability to apply this method using different IASI platforms, in addition to the ability to identify the dust emission source.
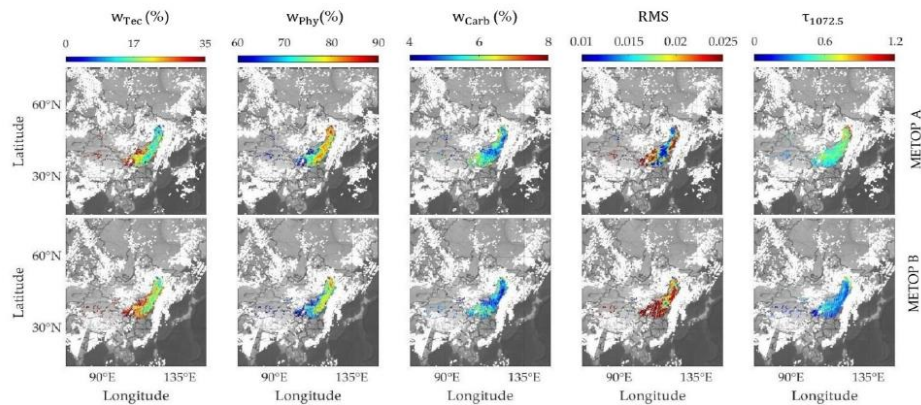
Figure 16. Mineralogical extinction coefficient maps of tectosilicates, phyllosilicates, and carbonates on May 4 during the 2017 dust storm from IASI detection of METOP-A and METOP-B.

154

5.2.2. March 2021 from IASI-A

The mineralogical mapping method was applied to a more recent dust storm that occurred in March 2021. The first dust plume was generated from the Mongolian Gobi Desert on 14 March, with winds blowing on 15 March uplifting aerosols from the Gobi Desert and Horqin Sandy Land together, to travel southeastward. On 16 March, another dust plume was produced from the Taklamakan Desert, floating and mixing with loads already present in the atmosphere. A previous study investigated dust sources only originating from the Gobi Desert between 14 and 15 March [67].

The study applied to a time interval between 14 March at night and 18 March during the day, as shown in Figure 17, where the mineralogical weights showed a regular temporal evolution as the first and second dust plumes were carried into the atmosphere. After applying the LC method, 15% of the values are rejected, the double of the percentage value of the first case. This can be linked to the difference in the size distribution between the emissions for the two cases in the study; the PM10 concentration emissions were double in March 2021 [67,68]. Likewise, in this case, the optical thickness was inverse to the residue RMS.

Table 3 shows the half-day mean mineralogical values, with the RMS and the optical thickness at 1072.5 cm^{-1}. In this case, the mean mass weight value of the tectosilicates was 25% of type I, unlike in May 2017. Intense dust emissions from this region started on 16 March during the day (16D), made up of 66% phyllosilicates and 7.4% carbonates. In type II, the results show consistency with the previous case study. However, type III indicates the uplift of heavier tectosilicate particles and fewer phyllosilicate fine particles. The carbonate mean values were close for types I and II, with the highest peak from type I at 9% and the lowest from type III at 5.2%. More intense optical thickness values were found in this case since the dust mass concentration emitted reached almost 1×10^4 µg/m^3 of the May 2017 values of less than 5×10^3 µg/m^3 [67,68].

Table 3. The mean mineralogical values and STDs of the three dust type sources in the dust storm of March 2021 in East Asia.

| Date	Mean Mass Weight per Half-Day (%)									Mean RMS			Mean $\tau_{1072.5\text{cm}^{-1}}$		
	Tec			Phy			Carb								
	I	II	III	I	II	III	I	II	III	I	II	III	I	II	III
14N	-	26.6	-	-	65.1	-	-	8.3	-	-	0.014	-	-	0.958	-
15D	-	16.1	-	-	75.9	-	-	8.0	-	-	0.016	-	-	0.971	-
15N	-	22.4	44.1	-	69.3	50.2	-	7.1	5.2	-	0.017	0.010	-	0.698	0.967
16D	21.9	17.0	40.1	68.1	76.4	54.7	9.0	6.8	6.4	0.020	0.015	0.011	0.833	0.943	0.72
16N	-	26.0	-	-	66.9	-	-	7.4	-	-	0.020	-	-	0.731	-
17D	23.8	23.6	-	68.8	69.9	-	7.4	6.4	-	0.019	0.017	-	0.892	0.976	-
17N	28.8	26.6	-	62.0	66.7	-	6.8	6.3	-	0.025	0.016	-	0.786	0.776	-
18D	26.8	24.4	-	67.0	69.4	-	6.2	6.2	-	0.016	0.015	-	1.024	1.002	-
Mean	25.3	22.8	42.1	66.5	70.0	52.5	7.4	7.1	5.8	0.020	0.016	0.011	0.884	0.882	0.841
STD	2.7	3.9	2.0	2.6	3.9	2.2	1.0	0.7	0.6	0.004	0.002	0.011	0.089	0.117	0.124

Figure 17. Mineralogical mass weight maps of tectosilicates, phyllosilicates, and carbonates during the 14–18 March 2021 dust storm by day (D) and night (N) from IASI detections.

First, on 15 March, dust mass III was a mixture of the Gobi and Horqin sources, with high tectosilicate content. This agrees with the results obtained in May 2017, with the Horqin Sandy Land source causing the increase in tectosilicate weight. This can be compared to dust mass II, presenting lower tectosilicate content as it originated only from the Gobi Desert. In addition, the weight of phyllosilicates was higher in II compared to III,

suggesting that dust emissions in II were from the Gobi Desert. By the nights of 16 and 17 March (16N and 17N), clouds covered the region, masking dust plume detection. On 17 March by day (17D), the mineralogical weights had heterogeneous variability in the three different regions, each related to a different source. In Figure 18, the HYSPLIT 24 h backward trajectory of that day indicates the presence of another type I dust load from the Taklamakan Desert, originating from the emissions of 16 March by day and traveling in the same direction as the uplifted masses of type II from the Gobi Desert. In addition, another mass traveled from Central Asia, showing different mineralogy that was particularly rich in tectosilicates (the values of this plume are not shown in Table 3).
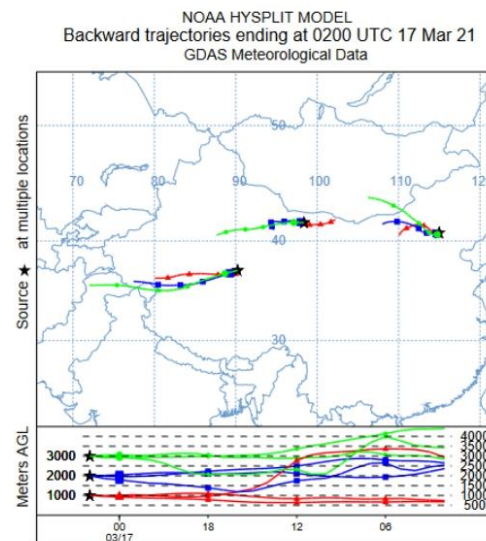
Figure 18. HYSPLIT 24 h backward trajectory for different dust detections in dust storms on 17 March 2021 by day.

6. Conclusions

This paper introduced a method for computing mineralogical weights during dust storm events using both experimental optical properties and satellite detections from IASI.

First, we found that dust detections above land were highly affected by LSE. Soil that is highly rich in quartz generates the Reststrahlen phenomenon, altering the IASI observation and causing false aerosol selection and characterization. To solve this problem, a mean monthly emissivity dataset was used. However, the direct use of these data can strongly change spectral detection, losing aerosol signals. Due to this, a new LSE optimization method was developed using the same data and is based on the Reststrahlen feature at 1159 cm^{-1}. A correction factor was calculated and applied to the IASI detection spectra. This method allowed for improving the surface effect of the aerosol detections without altering the mineral dust information from both day and night observations, as applied to the two case studies with different temporal and seasonal characteristics. This indicates the ability to apply the LSE correction method to different case studies.

Second, we considered that dust presents a heterogeneous mixture of pure minerals. Thus, we applied an LC method to the laboratory extinction coefficients of pure minerals to fit the Gobi dust spectrum, showing a residue of 2.5%. This indicates that the Gobi dust was an external mixture of individual minerals. In addition, after LSE correction, an aerosol optical thickness spectrum from the IASI was derived, with molecular features similar to

the optical thickness of the experimental Gobi dust sample. The LC was also applied to the satellite optical thickness and the residue shifted to 20% due to the presence of narrow gas bands. However, this residue dropped to 5% after smoothing the spectrum.

Third, mineralogical weight maps were obtained for three mineral families: tectosilicates, phyllosilicates, and carbonates, with the RMS and the optical thickness at 1077 cm^{-1}. The method was applied to two case studies detected from IASI-A by day and night, in two different seasons, with a time gap of 5 years between them: spring 2017 and winter 2021. The results also show mean mineralogical weights close to the literature. With high temporal and spatial variability for tectosilicates and carbonates, the weights were linked to the dust source. Hence, this method presents a powerful tool to link dust mineralogy to the original sources.

These results imply the temporal stability of IASI-A in a time gap of five years and show the ability to use IASI detection in different seasons. In addition, IASI-A and IASI-B were compared, giving consistent mineral weights, which allows for the application of this work using different IASI platforms in the future.

Finally, laboratory optical properties exploited with IASI measurements allowed for obtaining new information about mineralogical dust composition in the East Asian deserts. An important link between the LC rejected values and the particle size distribution was also determined. This highlights the importance of the quantification of the size distribution parameter. In future work, we will use laboratory complex refractive indices derived from extinction spectra to retrieve the microphysical and mineralogical dust properties.

Author Contributions: Conceptualization, H.H.; methodology, H.H. and P.A.; software, P.A. and H.H.; validation, P.A., H.H., L.D., A.A.C. and D.P.; formal analysis, P.A., H.H. and L.D.; investigation, P.A. and H.H.; writing—original draft preparation, P.A. and H.H.; writing—review and editing, P.A., H.H., L.D., A.A.C. and D.P.; supervision, H.H.; project administration, H.H.; funding acquisition, H.H. All authors have read and agreed to the published version of the manuscript.

Conflicts of Interest: The authors declare no conflict of interest.

References

1. Duniway, M.C.; Pfennigwerth, A.A.; Fick, S.E.; Nauman, T.W.; Belnap, J.; Barger, N.N. Wind erosion and dust from US drylands: A review of causes, consequences, and solutions in a changing world. *Ecosphere* **2019**, *10*, e02650. [CrossRef]
2. Querol, X.; Tobías, A.; Pérez, N.; Karanasiou, A.; Amato, F.; Stafoggia, M.; Pérez García-Pando, C.; Ginoux, P.; Forastiere, F.; Gumy, S.; et al. Monitoring the impact of desert dust outbreaks for air quality for health studies. *Environ. Int.* **2019**, *130*, 104867. [CrossRef] [PubMed]
3. Safriel, U.N. The assessment of global trends in land degradation. In *Climate and Land Degradation*; Sivakumar, M.V.K., Ndiang'ui, N., Eds.; Springer: Berlin/Heidelberg, Germany, 2007; pp. 1–38. ISBN 978-3-540-72438-4.
4. Bi, J.; Huang, J.; Shi, J.; Hu, Z.; Zhou, T.; Zhang, G.; Huang, Z.; Wang, X.; Jin, H. Measurement of scattering and absorption properties of dust aerosol in a Gobi farmland region of northwestern China—A potential anthropogenic influence. *Atmos. Chem. Phys.* **2017**, *17*, 7775–7792. [CrossRef]
5. Kanji, Z.A.; Sullivan, R.C.; Niemand, M.; DeMott, P.J.; Prenni, A.J.; Chou, C.; Saathoff, H.; Möhler, O. Heterogeneous ice nucleation properties of natural desert dust particles coated with a surrogate of secondary organic aerosol. *Atmos. Chem. Phys.* **2019**, *19*, 5091–5110. [CrossRef]

6. Michel, A.E.; Usher, C.R.; Grassian, V.H. Reactive uptake of ozone on mineral oxides and mineral dusts. *Atmos. Environ.* **2003**, *37*, 3201–3211. [CrossRef]

7. Augustin-Bauditz, S.; Wex, H.; Kanter, S.; Ebert, M.; Niedermeier, D.; Stolz, F.; Prager, A.; Stratmann, F. The immersion mode ice nucleation behavior of mineral dusts: A comparison of different pure and surface modified dusts. *Geophys. Res. Lett.* **2014**, *41*, 7375–7382. [CrossRef]

8. Marcotte, A.R.; Anbar, A.D.; Majestic, B.J.; Herckes, P. Mineral Dust and Iron Solubility: Effects of Composition, Particle Size, and Surface Area. *Atmosphere* **2020**, *11*, 533. [CrossRef]

9. Washington, R.; Todd, M.C. Atmospheric controls on mineral dust emission from the Bodélé Depression, Chad: The role of the low level jet. *Geophys. Res. Lett.* **2005**, *32*, 1–5. [CrossRef]

10. An, L.; Che, H.; Xue, M.; Zhang, T.; Wang, H.; Wang, Y.; Zhou, C.; Zhao, H.; Gui, K.; Zheng, Y.; et al. Temporal and spatial variations in sand and dust storm events in East Asia from 2007 to 2016: Relationships with surface conditions and climate change. *Sci. Total Environ.* **2018**, *633*, 452–462. [CrossRef]

11. Xie, Y.; Liu, Z.; Wen, T.; Huang, X.; Liu, J.; Tang, G.; Yang, Y.; Li, X.; Shen, R.; Hu, B.; et al. Characteristics of chemical composition and seasonal variations of PM2.5 in Shijiazhuang, China: Impact of primary emissions and secondary formation. *Sci. Total Environ.* **2019**, *677*, 215–229. [CrossRef]

12. Wu, J.; Kurosaki, Y.; Shinoda, M.; Kai, K. Regional Characteristics of Recent Dust Occurrence and Its Controlling Factors in East Asia. *SOLA* **2016**, *12*, 187–191. [CrossRef]

13. Chen, Y.; Luo, B.; Xie, S. dong Characteristics of the long-range transport dust events in Chengdu, Southwest China. *Atmos. Environ.* **2015**, *122*, 713–722. [CrossRef]

14. Mikami, M.; Shi, G.Y.; Uno, I.; Yabuki, S.; Iwasaka, Y.; Yasui, M.; Aoki, T.; Tanaka, T.Y.; Kurosaki, Y.; Masuda, K.; et al. Aeolian dust experiment on climate impact: An overview of Japan–China joint project ADEC. *Glob. Planet. Chang.* **2006**, *52*, 142–172. [CrossRef]

15. Guo, J.; Lou, M.; Miao, Y.; Wang, Y.; Zeng, Z.; Liu, H.; He, J.; Xu, H.; Wang, F.; Min, M.; et al. Trans-Pacific transport of dust aerosols from East Asia: Insights gained from multiple observations and modeling. *Environ. Pollut.* **2017**, *230*, 1030–1039. [CrossRef] [PubMed]

16. Grousset, F.E.; Ginoux, P.; Bory, A.; Biscaye, P.E. Case study of a Chinese dust plume reaching the French Alps. *Geophys. Res. Lett.* **2003**, *30*, 1277. [CrossRef]

17. Young Jeong, G. Mineralogy and geochemistry of Asian dust: Dependence on migration path, fractionation, and reactions with polluted air. *Atmos. Chem. Phys.* **2020**, *20*, 7411–7428. [CrossRef]

18. Chen, J.; Li, G.J. Geochemical studies on the source region of Asian dust. *Sci. China Earth Sci.* **2011**, *54*, 1279–1301. [CrossRef]

19. Shao, L.Y.; Li, W.J.; Yang, S.S.; Shi, Z.B.; Lü, S.L. Mineralogical characteristics of airborne particles collected in Beijing during a severe Asian dust storm period in spring 2002. *Sci. China Ser. D Earth Sci.* **2007**, *50*, 953–959. [CrossRef]

20. Shen, Z.; Caquineau, S.; Cao, J.; Zhang, X.; Han, Y.; Gaudichet, A.; Gomes, L. Mineralogical characteristics of soil dust from source regions in northern China. *Particuology* **2009**, *7*, 507–512. [CrossRef]

21. Di Biagio, C.; Formenti, P.; Styler, S.A.; Pangui, E.; Doussin, J.F. Laboratory chamber measurements of the longwave extinction spectra and complex refractive indices of African and Asian mineral dusts. *Geophys. Res. Lett.* **2014**, *41*, 6289–6297. [CrossRef]

22. Wainker, D.M.; Tackett, J.L.; Getzewich, B.J.; Liu, Z.; Vaughan, M.A.; Rogers, R.R. The global 3-D distribution of tropospheric aerosols as characterized by CALIOP. *Atmos. Chem. Phys.* **2013**, *13*, 3345–3361. [CrossRef]

23. Wang, Z.; Uno, I.; Yumimoto, K.; Pan, X.; Chen, X.; Li, J.; Wang, Z.; Shimizu, A.; Sugimoto, N. Dust Heterogeneous Reactions during Long-Range Transport of a Severe Dust Storm in May 2017 over East Asia. *Atmosphere* **2019**, *10*, 680. [CrossRef]

24. Ginoux, P.; Garbuzov, D.; Hsu, N.C. Identification of anthropogenic and natural dust sources using Moderate Resolution Imaging Spectroradiometer (MODIS) Deep Blue level 2 data. *J. Geophys. Res. Atmos.* **2010**, *115*, 5204. [CrossRef]

25. Pierangelo, C.; Mishchenko, M.; Balkanski, Y.; Chédin, A. Retrieving the effective radius of Saharan dust coarse mode from AIRS. *Geophys. Res. Lett.* **2005**, *32*, 1–4. [CrossRef]

26. Klüser, L.; Martynenko, D.; Holzer-Popp, T. Thermal infrared remote sensing of mineral dust over land and ocean: A spectral SVD based retrieval approach for IASI. *Atmos. Meas. Tech.* **2011**, *4*, 757–773. [CrossRef]

27. Chen, S.Y.; Huang, J.P.; Li, J.X.; Jia, R.; Jiang, N.X.; Kang, L.T.; Ma, X.J.; Xie, T.T. Comparison of dust emissions, transport, and deposition between the Taklimakan Desert and Gobi Desert from 2007 to 2011. *Sci. China Earth Sci.* **2017**, *60*, 1338–1355. [CrossRef]

28. Masiello, G.; Serio, C.; Venafra, S.; DeFeis, I.; Borbas, E.E. Diurnal variation in Sahara desert sand emissivity during the dry season from IASI observations. *J. Geophys. Res. Atmos.* **2014**, *119*, 1626–1638. [CrossRef]

29. Ackerman, S.A. Remote sensing aerosols using satellite infrared observations. *J. Geophys. Res. Atmos.* **1997**, *102*, 17069–17079. [CrossRef]

30. Crevoisier, C.; Clerbaux, C.; Guidard, V.; Phulpin, T.; Armante, R.; Barret, B.; Camy-Peyret, C.; Chaboureau, J.P.; Coheur, P.F.; Crépeau, L.; et al. Towards IASI-New Generation (IASI-NG): Impact of improved spectral resolution and radiometric noise on the retrieval of thermodynamic, chemistry and climate variables. *Atmos. Meas. Tech.* **2014**, *7*, 4367–4385. [CrossRef]

31. Blumstein, D.; Chalon, G.; Carlier, T.; Buil, C.; Hebert, P.; Maciaszek, T.; Ponce, G.; Phulpin, T.; Tournier, B.; Simeoni, D.; et al. IASI instrument: Technical overview and measured performances. *Infrared Spaceborne Remote Sens. XII* **2004**, *5543*, 196. [CrossRef]

32. Hilton, F.; Armante, R.; August, T.; Barnet, C.; Bouchard, A.; Camy-Peyret, C.; Capelle, V.; Clarisse, L.; Clerbaux, C.; Coheur, P.-F.; et al. Hyperspectral Earth Observation from IASI: Five Years of Accomplishments. *Bull. Am. Meteorol. Soc.* **2012**, *93*, 347–370. [CrossRef]

33. Clerbaux, C.; Boynard, A.; Clarisse, L.; George, M.; Hadji-Lazaro, J.; Herbin, H.; Hurtmans, D.; Pommier, M.; Razavi, A.; Turquety, S.; et al. Atmospheric Chemistry and Physics Monitoring of atmospheric composition using the thermal infrared IASI/MetOp sounder. *Atmos. Chem. Phys* **2009**, *9*, 6041–6054. [CrossRef]

34. Van Damme, M.; Clarisse, L.; Heald, C.L.; Hurtmans, D.; Ngadi, Y.; Clerbaux, C.; Dolman, A.J.; Erisman, J.W.; Coheur, P.F. Global distributions, time series and error characterization of atmospheric ammonia (NH3) from IASI satellite observations. *Atmos. Chem. Phys.* **2014**, *14*, 2905–2922. [CrossRef]

35. Wei, S.-W.; Lu, C.-H.; Liu, Q.; Collard, A.; Zhu, T.; Grogan, D.; Li, X.; Wang, J.; Grumbine, R.; Bhattacharjee, P.S. The Impact of Aerosols on Satellite Radiance Data Assimilation Using NCEP Global Data Assimilation System. *Atmosphere* **2021**, *12*, 432. [CrossRef]

36. Griffiths, P.R.; De Haseth, J.A. *Fourier Transform Infrared Spectrometry*, 2nd ed.; Wiley: Hoboken, NJ, USA, 2007; ISBN 978-0-471-19404-0.

37. Bohren, C.F.; Huffman, D.R. *Absorption and Scattering of Light by Small Particles*; Wiley: Hoboken, NJ, USA, 1989; ISBN 047105772X.

38. Bauduin, S.; Clarisse, L.; Theunissen, M.; George, M.; Hurtmans, D.; Clerbaux, C.; Coheur, P.F. IASI's sensitivity to near-surface carbon monoxide (CO): Theoretical analyses and retrievals on test cases. *J. Quant. Spectrosc. Radiat. Transf.* **2017**, *189*, 428–440. [CrossRef]

39. Clarisse, L.; Clerbaux, C.; Franco, B.; Hadji-Lazaro, J.; Whitburn, S.; Kopp, A.K.; Hurtmans, D.; Coheur, P.-F. A Decadal Data Set of Global Atmospheric Dust Retrieved From IASI Satellite Measurements. *J. Geophys. Res. Atmos.* **2019**, *124*, 1618–1647. [CrossRef]

40. Piontek, D.; Bugliaro, L.; Kar, J.; Schumann, U.; Marenco, F.; Plu, M.; Voigt, C. The New Volcanic Ash Satellite Retrieval VACOS Using MSG/SEVIRI and Artificial Neural Networks: 2. Validation. *Remote Sens.* **2021**, *13*, 3128. [CrossRef]

41. Zhou, D.K.; Smith, W.L.; Larar, A.M.; Liu, X.; Taylor, J.P.; Schlüssel, P.; Strow, L.L.; Mango, S.A. All weather IASI single field-of-view retrievals: Case study—Validation with JAIVEx data. *Atmos. Chem. Phys.* **2009**, *9*, 2241–2255. [CrossRef]

42. Zhou, D.K.; Larar, A.M.; Liu, X.; Smith, W.L.; Strow, L.L.; Yang, P.; Schlüssel, P.; Calbet, X. Global land surface emissivity retrieved from satellite ultraspectral IR measurements. *IEEE Trans. Geosci. Remote Sens.* **2011**, *49*, 1277–1290. [CrossRef]

43. Zhou, D.K.; Larar, A.M.; Liu, X. Monitoring surface climate with its emissivity derived from satellite measurements. *Land Surf. Remote Sens.* **2012**, *8524*, 55–61. [CrossRef]

44. Zhou, D.K.; Larar, A.M.; Liu, X. Update on Iasi Emissivity Atlas. In Proceedings of the 19th International TOVS Study Conference (ITSC-19), Jeju Island, Korea, 26 March–1 April 2014.

45. Huang, X.; Chen, X.; Zhou, D.K.; Liu, X. An Observationally Based Global Band-by-Band Surface Emissivity Dataset for Climate and Weather Simulations. *J. Atmos. Sci.* **2016**, *73*, 3541–3555. [CrossRef]

46. Simms, J.E.; Berney, I.E.S.; Harrelson, D.W.; Corcoran, M.K.; Castellane, R.M. *Analysis of Long Wave Infrared (LWIR) Soil Data to Predict Reflectance Response*; Engineer Research And Development Center Vicksburg Ms Geotechnical And Structures Lab: Vicksburg, MS, USA, 2009.

47. Herbin, H. Cloud Spectral Detection from IASI Using Principal Component Analysis. 2022; *unpublished work*.

48. Formenti, P.; Schütz, L.; Balkanski, Y.; Desboeufs, K.; Ebert, M.; Kandler, K.; Petzold, A.; Scheuvens, D.; Weinbruch, S.; Zhang, D. Recent progress in understanding physical and chemical properties of African and Asian mineral dust. *Atmos. Chem. Phys.* **2011**, *11*, 8231–8256. [CrossRef]

49. Journet, E.; Balkanski, Y.; Harrison, S.P. A new data set of soil mineralogy for dust-cycle modeling. *Atmos. Chem. Phys.* **2014**, *14*, 3801–3816. [CrossRef]

50. Herbin, H.; Pujol, O.; Hubert, P.; Petitprez, D. New approach for the determination of aerosol refractive indices—Part I: Theoretical bases and numerical methodology. *J. Quant. Spectrosc. Radiat. Transf.* **2017**, *200*, 311–319. [CrossRef]

51. Hubert, P.; Herbin, H.; Visez, N.; Pujol, O.; Petitprez, D. New approach for the determination of aerosol refractive indices—Part II: Experimental set-up and application to amorphous silica particles. *J. Quant. Spectrosc. Radiat. Transf.* **2017**, *9*, 37. [CrossRef]

52. Deschutter, L.; Herbin, H.; Petitprez, D. Optical properties of Gobi dust and its pure compounds: Experimental extinction spectra and complex refractive indices determination. In Proceedings of the 23rd EGU General Assembly, Online, 19–30 April 2021; p. EGU21-2115.

53. Romanias, M.N.; Zeineddine, M.N.; Gaudion, V.; Lun, X.; Thevenet, F.; Riffault, V. Heterogeneous Interaction of Isopropanol with Natural Gobi Dust. *Environ. Sci. Technol.* **2016**, *50*, 11714–11722. [CrossRef]

54. Spitzer, W.G.; Kleinman, D.A. Infrared Lattice Bands of Quartz. *Phys. Rev.* **1961**, *121*, 1324. [CrossRef]

55. Reig, F.B.; Adelantado, J.V.G.; Moya Moreno, M.C.M. FTIR quantitative analysis of calcium carbonate (calcite) and silica (quartz) mixtures using the constant ratio method. Application to geological samples. *Talanta* **2002**, *58*, 811–821. [CrossRef]

56. Madejova, J.; Komadel, P. Baseline Studies of the Clay Minerals Society Source Clays: Infrared Methods. *Clays Clay Miner.* **2001**, *49*, 410–432. [CrossRef]

57. Madejová, J.; Gates, W.P.; Petit, S. IR Spectra of Clay Minerals. In *Developments in Clay Science*; Elsevier: Amsterdam, The Netherlands, 2017; Volume 8, pp. 107–149.

58. Green, D.; Schodlok, M. Characterisation of carbonate minerals from hyperspectral TIR scanning using features at 14 000 and 11 300 nm. *Aust. J. Earth Sci.* **2016**, *63*, 951–957. [CrossRef]

59. Bishop, J.L.; King, S.J.; Lane, M.D.; Brown, A.J.; Lafuente, B.; Hiroi, T.; Roberts, R.; Swayze, G.A.; Lin, J.F.; Sánchez Román, M. Spectral Properties of Anhydrous Carbonates and Nitrates. *Earth Sp. Sci.* **2021**, *8*, e2021EA001844. [CrossRef]
60. He, M.; Yan, W.; Chang, Y.; Liu, K.; Liu, X. Fundamental infrared absorption features of α-quartz: An unpolarized single-crystal absorption infrared spectroscopic study. *Vib. Spectrosc.* **2019**, *101*, 52–63. [CrossRef]
61. Sokolik, I.N.; Toon, O.B. Incorporation of mineralogical composition into models of the radiative properties of mineral aerosol from UV to IR wavelengths. *J. Geophys. Res. Atmos.* **1999**, *104*, 9423–9444. [CrossRef]
62. Bichon, J.; Lavancier, M.; Petitprez, D.; Deguine, A.; Hourlier, D.; Deboudt, K.; Herbin, H.; Ducournau, G.; Peretti, R.; Eliet, S. Complex refractive indices in the TeraHertz domain of samples from atmospheric aerosol sources. In Proceedings of the International Conference on Infrared, Millimeter, and Terahertz Waves, IRMMW-THz, Chengdu, China, 29 August–3 September 2021.
63. Minamoto, Y.; Nakamura, K.; Wang, M.; Kawai, K.; Ohara, K.; Noda, J.; Davaanyam, E.; Sugimoto, N.; Kai, K. Large-scale dust event in East Asia in May 2017: Dust emission and transport from multiple source regions. *Sci. Online Lett. Atmos.* **2018**, *14*, 33–38. [CrossRef]
64. Xuan, J.; Sokolik, I.N. Characterization of sources and emission rates of mineral dust in Northern China. *Atmos. Environ.* **2002**, *36*, 4863–4876. [CrossRef]
65. Ginoux, P.; Prospero, J.M.; Gill, T.E.; Hsu, N.C.; Zhao, M. Global-scale attribution of anthropogenic and natural dust sources and their emission rates based on MODIS Deep Blue aerosol products. *Rev. Geophys.* **2012**, *50*, 388. [CrossRef]
66. Plans for Metop-A End of Life | EUMETSAT. Available online: https://www.eumetsat.int/plans-metop-end-life (accessed on 16 December 2021).
67. Wang, F.; Yang, T.; Wang, Z.; Cao, J.; Liu, B.; Liu, J.; Chen, S.; Liu, S.; Jia, B.; Chan, L.; et al. A Comparison of the Different Stages of Dust Events over Beijing in March 2021: The Effects of the Vertical Structure on Near-Surface Particle Concentration. *Remote Sens.* **2021**, *13*, 3580. [CrossRef]
68. She, L.; Xue, Y.; Guang, J.; Che, Y.; Fan, C.; Li, Y.; Xie, Y. Towards a comprehensive view of dust events from multiple satellite and ground measurements: Exemplified by the May 2017 East Asian dust storm. *Nat. Hazards Earth Syst. Sci.* **2018**, *18*, 3187–3201. [CrossRef]

Appendix B

Invited Guest Speaker (Virtual), "Aerosol Chemical and Microphysical Properties from IASI and In-situ Laboratory Measurements", UMBC Colloquium, Baltimore, MA, 16 November 2022.

Oral Presentation, "Aerosol Mineralogical and Microphysical Study using Laboratory and IASI Measurements: Application to East Asian Deserts.", International Radiation Symposium - IRS 2022 Conference, Thessaloniki, Greece, 4-8 July 2022.

Oral Presentation, "Aerosol Mineralogical and Microphysical Study from Laboratory to Satellite Remote Sensing IASI Measurements: Application to East Asian Deserts.", European Geosciences Union - EGU 2022 Conference, Vienna, Austria, 23–27 May 2022.

Oral Presentation, "Aerosol Chemical and µ-Physical Study from Laboratory to IASI Measurements: Application to Gobi Desert.", Infrared Atmospheric Sounding Interferometer - IASI 2021 Conference, Evian-les-Bains, France, 6-10 December 2021.

Virtual Oral Presentation, "Tropospheric Mineral Dust Study by High Spectral Resolution Infrared Satellite Remote Sensing.", European Geosciences Union - EGU 2021 Conference, 19–30 April 2021.

REFERENCES

Abtahi, A.: Soil Genesis as Affected by Topography and Time in Highly Calcareous Parent Materials Under Semiarid Conditions in Iran, Soil Sci. Soc. Am. J., 44(2), 329–336, doi:10.2136/SSSAJ1980.03615995004400020025X, 1980.

Ackerman, S. A.: Remote sensing aerosols using satellite infrared observations, J. Geophys. Res. Atmos., 102(D14), 17069–17079, doi:10.1029/96JD03066, 1997.

An, L., Che, H., Xue, M., Zhang, T., Wang, H., Wang, Y., Zhou, C., Zhao, H., Gui, K., Zheng, Y., Sun, T., Liang, Y., Sun, E., Zhang, H. and Zhang, X.: Temporal and spatial variations in sand and dust storm events in East Asia from 2007 to 2016: Relationships with surface conditions and climate change, Sci. Total Environ., 633, 452–462, doi:10.1016/J.SCITOTENV.2018.03.068, 2018.

Anon: MATLAB (2019a), n.d.

Baisantry, M. and Khare, A.: Pan Sharpening for Hyper Spectral Imagery Using Spectral Mixing-Based Color Preservation Model, J. Indian Soc. Remote Sens. 2016 455, 45(5), 743–748, doi:10.1007/S12524-016-0643-9, 2016.

Bauduin, S., Clarisse, L., Theunissen, M., George, M., Hurtmans, D., Clerbaux, C. and Coheur, P. F.: IASI's sensitivity to near-surface carbon monoxide (CO): Theoretical analyses and retrievals on test cases, J. Quant. Spectrosc. Radiat. Transf., 189, 428–440, doi:10.1016/J.JQSRT.2016.12.022, 2017.

Bi, J., Huang, J., Shi, J., Hu, Z., Zhou, T., Zhang, G., Huang, Z., Wang, X. and Jin, H.: Measurement of scattering and absorption properties of dust aerosol in a Gobi farmland region of northwestern China - A potential anthropogenic influence, Atmos. Chem. Phys., 17(12), 7775–7792, doi:10.5194/ACP-17-7775-2017, 2017.

Di Biagio, C., Formenti, P., Styler, S. A., Pangui, E. and Doussin, J. F.: Laboratory chamber measurements of the longwave extinction spectra and complex refractive indices of African and Asian mineral dusts, Geophys. Res. Lett., 41(17), 6289–6297, doi:10.1002/2014GL060213, 2014a.

Di Biagio, C., Boucher, H., Caquineau, S., Chevaillier, S., Cuesta, J. and Formenti, P.: Variability of the infrared complex refractive index of African mineral dust: Experimental estimation and implications for radiative transfer and satellite remote sensing, Atmos. Chem. Phys., 14(20), 11093–11116, doi:10.5194/ACP-14-11093-2014, 2014b.

Di Biagio, C., Formenti, P., Balkanski, Y., Caponi, L., Cazaunau, M., Pangui, E., Journet, E., Nowak, S., Caquineau, S., Andreae O, M., Kandler, K., Saeed, T., Piketh, S., Seibert, D., Williams, E. and Doussin, J. F. C.: Global scale variability of the mineral dust long-wave refractive index: A new dataset of in situ measurements for climate modeling and remote sensing, Atmos. Chem. Phys., 17(3), 1901–1929, doi:10.5194/ACP-17-1901-2017, 2017.

Bichon, J., Lavancier, M., Petitprez, D., Deguine, A., Hourlier, D., Deboudt, K., Herbin, H., Ducournau, G., Peretti, R. and Eliet, S.: Complex refractive indices in the TeraHertz domain of samples from atmospheric aerosol sources, in International Conference on Infrared,

Millimeter, and Terahertz Waves, IRMMW-THz, IEEE Computer Society, Chengdu, China., 2021.

Bishop, J. L., King, S. J., Lane, M. D., Brown, A. J., Lafuente, B., Hiroi, T., Roberts, R., Swayze, G. A., Lin, J. F. and Sánchez Román, M.: Spectral Properties of Anhydrous Carbonates and Nitrates, Earth Sp. Sci., 8(10), doi:10.1029/2021EA001844, 2021.

Blumstein, D., Chalon, G., Carlier, T., Buil, C., Hebert, P., Maciaszek, T., Ponce, G., Phulpin, T., Tournier, B., Simeoni, D., Astruc, P., Clauss, A., Kayal, G. and Jegou, R.: IASI instrument: technical overview and measured performances, Infrared Spaceborne Remote Sens. XII, 5543, 196, doi:10.1117/12.560907, 2004.

Born, M. and Wolf, E.: Principles of Optics., 1980.

Borstad, G., Brown, L., Truong, Q. S. B., Kelly, R., Healy, G., Paquette, J. P., Staenz, K. and Neville, R.: Hyperspectral Imagery for Safeguards Applications, in Proceedings of the 45th Annual Meeting of the Institute of Nuclear Materials Management, Orlando,Florida. [online] Available from: https://www.researchgate.net/publication/265755845_HYPERSPECTRAL_IMAGERY_FO R_SAFEGUARDS_APPLICATIONS (Accessed 19 November 2022), 2004.

Boucher, O.: Atmospheric Aerosols, 1st ed., Springer Netherlands, Dordrecht., 2015.

Caldwell, J. D., Lindsay, L., Giannini, V., Vurgaftman, I., Reinecke, T. L., Maier, S. A. and Glembocki, O. J.: Low-loss, infrared and terahertz nanophotonics using surface phonon polaritons, Nanophotonics, 4(1), 44–68, doi:10.1515/NANOPH-2014-0003, 2015.

Campbell, J. and Randolph, H. W.: Introduction to Remote Sensing, Fifth Edit., The Guilford Press, New York., 2011.

Capelle, V., Chédin, A., Siméon, M., Tsamalis, C., Pierangelo, C., Pondrom, M., Crevoisier, C., Crepeau, L. and Scott, N. A.: Evaluation of IASI-derived dust aerosol characteristics over the tropical belt, Atmos. Chem. Phys., 14(17), 9343–9362, doi:10.5194/ACP-14-9343-2014, 2014.

Cayla, F. and Javelle, P.: IASI: instrument overview, https://doi.org/10.1117/12.221368, 2553, 316–328, doi:10.1117/12.221368, 1995.

Chédin, A., Capelle, V., Scott, N. A. and Todd, M. C.: Contribution of IASI to the Observation of Dust Aerosol Emissions (Morning and Nighttime) Over the Sahara Desert, J. Geophys. Res. Atmos., 125(15), e2019JD032014, doi:10.1029/2019JD032014, 2020.

Chen, J. and Li, G. J.: Geochemical studies on the source region of Asian dust, Sci. China Earth Sci. 2011 549, 54(9), 1279–1301, doi:10.1007/S11430-011-4269-Z, 2011.

Chen, S. Y., Huang, J. P., Li, J. X., Jia, R., Jiang, N. X., Kang, L. T., Ma, X. J. and Xie, T. T.: Comparison of dust emissions, transport, and deposition between the Taklimakan Desert and Gobi Desert from 2007 to 2011, Sci. China Earth Sci. 2017 607, 60(7), 1338–1355, doi:10.1007/S11430-016-9051-0, 2017.

Chen, Y., Luo, B. and Xie, S. dong: Characteristics of the long-range transport dust events in

Chengdu, Southwest China, Atmos. Environ., 122, 713–722, doi:10.1016/J.ATMOSENV.2015.10.045, 2015.

Clarisse, L., Coheur, P. F., Prata, A. J., Hurtmans, D., Razavi, A., Phulpin, T., Hadji-Lazaro, J. and Clerbaux, C.: Tracking and quantifying volcanic SO2 with IASI, the September 2007 eruption at Jebel at Tair, Atmos. Chem. Phys., 8(24), 7723–7734, doi:10.5194/ACP-8-7723-2008, 2008.

Clarisse, L., Hurtmans, D., Prata, A. J., Karagulian, F., Clerbaux, C., De Mazière, M. and Coheur, P. F.: Retrieving radius, concentration, optical depth, and mass of different types of aerosols from high-resolution infrared nadir spectra, Appl. Opt., 49(19), 3713–3722, doi:10.1364/AO.49.003713, 2010.

Clarisse, L., Clerbaux, C., Franco, B., Hadji-Lazaro, J., Whitburn, S., Kopp, A. K., Hurtmans, D. and Coheur, P.-F.: A Decadal Data Set of Global Atmospheric Dust Retrieved From IASI Satellite Measurements, , doi:10.1029/2018JD029701, 2019.

Clerbaux, C., Boynard, A., Clarisse, L., George, M., Hadji-Lazaro, J., Herbin, H., Hurtmans, D., Pommier, M., Razavi, A., Turquety, S., Wespes, C. and Coheur, P.-F.: Atmospheric Chemistry and Physics Monitoring of atmospheric composition using the thermal infrared IASI/MetOp sounder, Atmos. Chem. Phys, 9, 6041–6054 [online] Available from: www.atmos-chem-phys.net/9/6041/2009/ (Accessed 24 May 2022), 2009.

Crevoisier, C., Clerbaux, C., Guidard, V., Phulpin, T., Armante, R., Barret, B., Camy-Peyret, C., Chaboureau, J. P., Coheur, P. F., Crépeau, L., Dufour, G., Labonnote, L., Lavanant, L., Hadji-Lazaro, J., Herbin, H., Jacquinet-Husson, N., Payan, S., Péquignot, E., Pierangelo, C., Sellitto, P. and Stubenrauch, C.: Towards IASI-New Generation (IASI-NG): Impact of improved spectral resolution and radiometric noise on the retrieval of thermodynamic, chemistry and climate variables, Atmos. Meas. Tech., 7(12), 4367–4385, doi:10.5194/AMT-7-4367-2014, 2014.

Cuesta, J., Eremenko, M., Flamant, C., Dufour, G., Laurent, B., Bergametti, G., Höpfner, M., Orphal, J. and Zhou, D.: Three-dimensional distribution of a major desert dust outbreak over East Asia in March 2008 derived from IASI satellite observations, J. Geophys. Res. Atmos., 120(14), 7099–7127, doi:10.1002/2014JD022406, 2015.

Van Damme, M., Wichink Kruit, R. J., Schaap, M., Clarisse, L., Clerbaux, C., Coheur, P. F., Dammers, E., Dolman, A. J. and Erisman, J. W.: Evaluating 4 years of atmospheric ammonia (NH3) over Europe using IASI satellite observations and LOTOS-EUROS model results, J. Geophys. Res. Atmos., 119(15), 9549–9566, doi:10.1002/2014JD021911, 2014.

Deboudt, K., Flament, P., Choël, M., Gloter, A., Sobanska, S. and Colliex, C.: Mixing state of aerosols and direct observation of carbonaceous and marine coatings on African dust by individual particle analysis, J. Geophys. Res. Atmos., 115(D24), 24207, doi:10.1029/2010JD013921, 2010.

Deguine, A.: Propriétés Optiques et Chimiques des cendres volcaniques: Mesures de Laboratoire et Applications à la télédétection Spatiale, Université de Lille., 2018.

Deschutter, L.: Propriétés optiques des poussières désertiques de Gobi et de ses composés

purs : spectres d'extinction expérimentaux et détermination des indices complexes de réfraction., Université de Lille, 9 March. [online] Available from: https://www.theses.fr/s326809 (Accessed 13 June 2022), 2022.

Desouza-Machado, S. G., Strow, L. L., Imbiriba, B., McCann, K., Hoff, R. M., Hannon, S. E., Martins, J. V., Tanré, D., Deuzé, J. L., Ducos, F. and Torres, O.: Infrared retrievals of dust using AIRS: Comparisons of optical depths and heights derived for a North African dust storm to other collocated EOS A-Train and surface observations, J. Geophys. Res. Atmos., 115(15), doi:10.1029/2009JD012842, 2010.

Duniway, M. C., Pfennigwerth, A. A., Fick, S. E., Nauman, T. W., Belnap, J. and Barger, N. N.: Wind erosion and dust from US drylands: a review of causes, consequences, and solutions in a changing world, Ecosphere, 10(3), e02650, doi:10.1002/ECS2.2650, 2019.

Egan, W. G. and Hilgeman, T. W.: Optical properties of inhomogeneous materials : applications to geology, astronomy, chemistry, and engineering, , 235, 1979.

Falkovich, A. H., Ganor, E., Levin, Z., Formenti, P. and Rudich, Y.: Chemical and mineralogical analysis of individual mineral dust particles, J. Geophys. Res. Atmos., 106(D16), 18029–18036, doi:10.1029/2000JD900430, 2001.

Fan, S. M., Horowitz, L. W., Levy, H. and Moxim, W. J.: Impact of air pollution on wet deposition of mineral dust aerosols, Geophys. Res. Lett., 31(2), 2104, doi:10.1029/2003GL018501, 2004.

Fang, Y., Elsworth, D., Wang, C. and Jia, Y.: Mineralogical Controls on Frictional Strength, Stability, and Shear Permeability Evolution of Fractures, J. Geophys. Res. Solid Earth, 123(5), 3549–3563, doi:10.1029/2017JB015338, 2018.

Felske, J. D., Charalampopoulos, T. T. and Hura, H. S.: Determination of the Refractive Indices of Soot Particles from the Reflectivities of Compressed Soot Pellets, http://dx.doi.org/10.1080/00102208408923757, 37(5–6), 263–283, doi:10.1080/00102208408923757, 2007.

Fischer, W. A., Hemphill, W. R. and Kover, A.: Progress in remote sensing (1972–1976), Photogrammetria, 32(2), 33–72, doi:10.1016/0031-8663(76)90013-2, 1976.

Formenti, P., Schütz, L., Balkanski, Y., Desboeufs, K., Ebert, M., Kandler, K., Petzold, A., Scheuvens, D., Weinbruch, S. and Zhang, D.: Recent progress in understanding physical and chemical properties of African and Asian mineral dust, Atmos. Chem. Phys., 11(16), 8231–8256, doi:10.5194/ACP-11-8231-2011, 2011.

Ginoux, P., Garbuzov, D. and Hsu, N. C.: Identification of anthropogenic and natural dust sources using Moderate Resolution Imaging Spectroradiometer (MODIS) Deep Blue level 2 data, J. Geophys. Res. Atmos., 115(D5), 5204, doi:10.1029/2009JD012398, 2010.

Ginoux, P., Prospero, J. M., Gill, T. E., Hsu, N. C. and Zhao, M.: Global-scale attribution of anthropogenic and natural dust sources and their emission rates based on MODIS Deep Blue aerosol products, Rev. Geophys., 50(3), doi:10.1029/2012RG000388, 2012.

Goody, R. M. and Yung, Y. L.: Atmospheric Radiation Theoretical Basis, 2nd ed., Oxford

University Press, USA., 1995.

Green, D. and Schodlok, M.: Characterisation of carbonate minerals from hyperspectral TIR scanning using features at 14 000 and 11 300 nm, http://dx.doi.org/10.1080/08120099.2016.1225601, 63(8), 951–957, doi:10.1080/08120099.2016.1225601, 2016.

Grieco, G., Masiello, G. and Serio, C.: Interferometric vs Spectral IASI Radiances: Effective Data-Reduction Approaches for the Satellite Sounding of Atmospheric Thermodynamical Parameters, Remote Sens. 2010, Vol. 2, Pages 2323-2346, 2(10), 2323–2346, doi:10.3390/RS2102323, 2010.

Griffin, J. J., Windom, H. and Goldberg, E. D.: The distribution of clay minerals in the World Ocean, Deep Sea Res. Oceanogr. Abstr., 15(4), 433–459, doi:10.1016/0011-7471(68)90051-X, 1968.

Griffiths, P. R. and De Haseth, J. A.: Fourier Transform Infrared Spectrometry, Second Edi., Wiley., 2007.

Grousset, F. E., Ginoux, P., Bory, A. and Biscaye, P. E.: Case study of a Chinese dust plume reaching the French Alps, Geophys. Res. Lett., 30(6), 1277, doi:10.1029/2002GL016833, 2003.

Guermazi, H., Sellitto, P., Cuesta, J., Eremenko, M., Lachatre, M., Mailler, S., Carboni, E., Salerno, G., Caltabiano, T., Menut, L., Serbaji, M. M., Rekhiss, F. and Legras, B.: Quantitative Retrieval of Volcanic Sulphate Aerosols from IASI Observations, Remote Sens. 2021, Vol. 13, Page 1808, 13(9), 1808, doi:10.3390/RS13091808, 2021.

Guo, J., Lou, M., Miao, Y., Wang, Y., Zeng, Z., Liu, H., He, J., Xu, H., Wang, F., Min, M. and Zhai, P.: Trans-Pacific transport of dust aerosols from East Asia: Insights gained from multiple observations and modeling, Environ. Pollut., 230, 1030–1039, doi:10.1016/J.ENVPOL.2017.07.062, 2017.

He, M., Yan, W., Chang, Y., Liu, K. and Liu, X.: Fundamental infrared absorption features of α-quartz: An unpolarized single-crystal absorption infrared spectroscopic study, Vib. Spectrosc., 101, 52–63, doi:10.1016/j.vibspec.2019.02.003, 2019.

Herbin, H.: Spectral Detection from IASI using Principal Component Analysis, , doi:herve.herbin@univ-lille.fr, 2017.

Herbin, H. and Dubuisson, P.: Infrared Observation of Earth's Atmosphere, ISTE., 2015.

Herbin, H., Hurtmans, D., Clerbaux, C., Clarisse, L. and Coheur, P. F.: H216O and HDO measurements with IASI/MetOp, Atmos. Chem. Phys., 9(24), 9433–9447, doi:10.5194/ACP-9-9433-2009, 2009.

Herbin, H., Pujol, O., Hubert, P. and Petitprez, D.: New approach for the determination of aerosol refractive indices – Part I: Theoretical bases and numerical methodology, J. Quant. Spectrosc. Radiat. Transf., 200, 311–319, doi:10.1016/J.JQSRT.2017.03.005, 2017.

Hilton, F., Armante, R., August, T., Barnet, C., Bouchard, A., Camy-Peyret, C., Capelle, V.,

Clarisse, L., Clerbaux, C., Coheur, P. F., Collard, A., Crevoisier, C., Dufour, G., Edwards, D., Faijan, F., Fourrié, N., Gambacorta, A., Goldberg, M., Guidard, V., Hurtmans, D., Illingworth, S., Jacquinet-Husson, N., Kerzenmacher, T., Klaes, D., Lavanant, L., Masiello, G., Matricardi, M., McNally, A., Newman, S., Pavelin, E., Payan, S., Péquignot, E., Peyridieu, S., Phulpin, T., Remedios, J., Schlüssel, P., Serio, C., Strow, L., Stubenrauch, C., Taylor, J., Tobin, D., Wolf, W. and Zhou, D.: Hyperspectral Earth Observation from IASI: Five Years of Accomplishments, Bull. Am. Meteorol. Soc., 93(3), 347–370, doi:10.1175/BAMS-D-11-00027.1, 2012.

Huang, X., Chen, X., Zhou, D. K. and Liu, X.: An Observationally Based Global Band-by-Band Surface Emissivity Dataset for Climate and Weather Simulations, J. Atmos. Sci., 73(9), 3541–3555, doi:10.1175/JAS-D-15-0355.1, 2016.

Huang, X., Chen, X., Flanner, M., Yang, P., Feldman, D. and Kuo, C.: Improved Representation of Surface Spectral Emissivity in a Global Climate Model and Its Impact on Simulated Climate, J. Clim., 31(9), 3711–3727, doi:10.1175/JCLI-D-17-0125.1, 2018.

Hubert, P., Herbin, H., Visez, N., Pujol, O. and Petitprez, D.: New approach for the determination of aerosol refractive indices - Part II: Experimental set-up and application to amorphous silica particles, J. Quant. Spectrosc. Radiat. Transf., 9(5), 1–8, doi:10.1016/j.jqsrt.2017.03.037, 2017.

Hyll, C.: Infrared Emittance of Paper - Method Development, Measurements and Applications, The Royal Institute of Technology, Stockholm., 2012.

Jaenicke, R.: Atmospheric aerosols and global climate, J. Aerosol Sci., 11(5–6), 577–588, doi:10.1016/0021-8502(80)90131-7, 1980.

Jickells, T. D., An, Z. S., Andersen, K. K., Baker, A. R., Bergametti, C., Brooks, N., Cao, J. J., Boyd, P. W., Duce, R. A., Hunter, K. A., Kawahata, H., Kubilay, N., LaRoche, J., Liss, P. S., Mahowald, N., Prospero, J. M., Ridgwell, A. J., Tegen, I. and Torres, R.: Global iron connections between desert dust, ocean biogeochemistry, and climate, Science (80-.)., 308(5718), 67–71, doi:10.1126/SCIENCE.1105959/ASSET/A588B3CE-F565-4B58-ADE0-CB039CDA7573/ASSETS/GRAPHIC/308_67_F2.JPEG, 2005.

Journet, E., Balkanski, Y. and Harrison, S. P.: A new data set of soil mineralogy for dust-cycle modeling, Atmos. Chem. Phys., 14(8), 3801–3816, doi:10.5194/ACP-14-3801-2014, 2014.

Kalashnikova, O. V. and Sokolik, I. N.: Modeling the radiative properties of nonspherical soil-derived mineral aerosols, J. Quant. Spectrosc. Radiat. Transf., 87(2), 137–166, doi:10.1016/J.JQSRT.2003.12.026, 2004.

Kanji, Z. A., Sullivan, R. C., Niemand, M., DeMott, P. J., Prenni, A. J., Chou, C., Saathoff, H. and Möhler, O.: Heterogeneous ice nucleation properties of natural desert dust particles coated with a surrogate of secondary organic aerosol, Atmos. Chem. Phys., 19(7), 5091–5110, doi:10.5194/ACP-19-5091-2019, 2019.

Kitamura, R., Pilon, L. and Jonasz, M.: Optical constants of silica glass from extreme ultraviolet to far infrared at nearroom temperature, Appl. Opt. Vol. 46, Issue 33, pp. 8118-

8133, 46(33), 8118–8133, doi:10.1364/AO.46.008118, 2007.

Klüser, L., Banks, J. R., Martynenko, D., Bergemann, C., Brindley, H. E. and Holzer-Popp, T.: Information content of space-borne hyperspectral infrared observations with respect to mineral dust properties, Remote Sens. Environ., 156, 294–309, doi:10.1016/J.RSE.2014.09.036, 2015.

Knippertz, P. and Stuut, J. B. W.: Mineral dust: A key player in the earth system, Springer Netherlands., 2014.

Legrand, M., Dubovik, O., Lapyonok, T. and Derimian, Y.: Accounting for particle non-sphericity in modeling of mineral dust radiative properties in the thermal infrared, J. Quant. Spectrosc. Radiat. Transf., 149, 219–240, doi:10.1016/J.JQSRT.2014.07.014, 2014.

Limpert, E., A. Stahel, W. and Abbt, M.: As the need grows for conceptualization, Bioscience, 51(5), 341–352, doi:10.1641/0006-3568(2001)051[0341:LNDATS]2.0.CO;2 Published: 01 May 2001, 2001.

Liu, C., Panetta, R. L. and Yang, P.: Inhomogeneity structure and the applicability of effective medium approximations in calculating light scattering by inhomogeneous particles, J. Quant. Spectrosc. Radiat. Transf., 146, 331–348, doi:10.1016/J.JQSRT.2014.03.018, 2014.

Madejova, J. and Komadel, P.: Baseline Studies of the Clay Minerals Society Source Clays: Infrared Methods, Clays Clay Miner., 49(5), 410–432, doi:10.1346/CCMN.2001.0490508, 2001.

Madejová, J., Gates, W. P. and Petit, S.: IR Spectra of Clay Minerals, in Developments in Clay Science, vol. 8, pp. 107–149, Elsevier, Amsterdam, The Netherlands., 2017.

Masiello, G., Serio, C., Venafra, S., DeFeis, I. and Borbas, E. E.: Diurnal variation in Sahara desert sand emissivity during the dry season from IASI observations, J. Geophys. Res. Atmos., 119(3), 1626–1638, doi:10.1002/JGRD.50863, 2014.

McPheat, R. A., Bass, S. F., Newnham, D. A., Ballard, J. and Remedios, J. J.: Comparison of aerosol and thin film spectra of supercooled ternary solution aerosol, J. Geophys. Res. Atmos., 107(D19), AAC 5-1, doi:10.1029/2001JD000641, 2002.

Michel, A. E., Usher, C. R. and Grassian, V. H.: Reactive uptake of ozone on mineral oxides and mineral dusts, Atmos. Environ., 37(23), 3201–3211, doi:10.1016/S1352-2310(03)00319-4, 2003.

Mikami, M., Shi, G. Y., Uno, I., Yabuki, S., Iwasaka, Y., Yasui, M., Aoki, T., Tanaka, T. Y., Kurosaki, Y., Masuda, K., Uchiyama, A., Matsuki, A., Sakai, T., Takemi, T., Nakawo, M., Seino, N., Ishizuka, M., Satake, S., Fujita, K., Hara, Y., Kai, K., Kanayama, S., Hayashi, M., Du, M., Kanai, Y., Yamada, Y., Zhang, X. Y., Shen, Z., Zhou, H., Abe, O., Nagai, T., Tsutsumi, Y., Chiba, M. and Suzuki, J.: Aeolian dust experiment on climate impact: An overview of Japan–China joint project ADEC, Glob. Planet. Change, 52(1–4), 142–172, doi:10.1016/J.GLOPLACHA.2006.03.001, 2006.

Minamoto, Y., Nakamura, K., Wang, M., Kawai, K., Ohara, K., Noda, J., Davaanyam, E., Sugimoto, N. and Kai, K.: Large-scale dust event in East Asia in May 2017: Dust emission

and transport from multiple source regions, Sci. Online Lett. Atmos., 14(May 2017), 33–38, doi:10.2151/sola.2018-006, 2018.

Möhler, O., Benz, S., Saathoff, H., Schnaiter, M., Wagner, R., Schneider, J., Walter, S., Ebert, V. and Wagner, S.: The effect of organic coating on the heterogeneous ice nucleation efficiency of mineral dustaerosols, Environ. Res. Lett., 3(2), 025007, doi:10.1088/1748-9326/3/2/025007, 2008.

Nousiainen, T.: Optical modeling of mineral dust particles: A review, J. Quant. Spectrosc. Radiat. Transf., 110(14–16), 1261–1279, doi:10.1016/J.JQSRT.2009.03.002, 2009.

Peterson, J. T., Weinman, J. A., Peterson, J. T. and Weinman, J. A.: Optical properties of quartz dust particles at infrared wavelengths, JGR, 74(28), 6947–6952, doi:10.1029/JC074I028P06947, 1969.

Pierangelo, C., Chédin, A., Heilliette, S., Jacquinet-Husson, N. and Armante, R.: Dust altitude and infrared optical depth from AIRS, Atmos. Chem. Phys., 4(7), 1813–1822, doi:10.5194/ACP-4-1813-2004, 2004.

Pierangelo, C., Mishchenko, M., Balkanski, Y. and Chédin, A.: Retrieving the effective radius of Saharan dust coarse mode from AIRS, Geophys. Res. Lett., 32(20), 1–4, doi:10.1029/2005GL023425, 2005.

Piontek, D., Bugliaro, L., Kar, J., Schumann, U., Marenco, F., Plu, M. and Voigt, C.: The New Volcanic Ash Satellite Retrieval VACOS Using MSG/SEVIRI and Artificial Neural Networks: 2. Validation, Remote Sens. 2021, Vol. 13, Page 3128, 13(16), 3128, doi:10.3390/RS13163128, 2021.

Press, W. H., Teukolsky, S. A., Vetterling, W. T. and Flannery, B. P.: Numerical Recipes in C ++ The Art of Scientific Computing Second Edition, Second Edi., CAMBRIDGE UNIVERSITY PRESS. [online] Available from: http://www.cambridge.org (Accessed 7 October 2022), 2007.

Putaud, J. P., Van Dingenen, R., Alastuey, A., Bauer, H., Birmili, W., Cyrys, J., Flentje, H., Fuzzi, S., Gehrig, R., Hansson, H. C., Harrison, R. M., Herrmann, H., Hitzenberger, R., Hüglin, C., Jones, A. M., Kasper-Giebl, A., Kiss, G., Kousa, A., Kuhlbusch, T. A. J., Löschau, G., Maenhaut, W., Molnar, A., Moreno, T., Pekkanen, J., Perrino, C., Pitz, M., Puxbaum, H., Querol, X., Rodriguez, S., Salma, I., Schwarz, J., Smolik, J., Schneider, J., Spindler, G., ten Brink, H., Tursic, J., Viana, M., Wiedensohler, A. and Raes, F.: A European aerosol phenomenology – 3: Physical and chemical characteristics of particulate matter from 60 rural, urban, and kerbside sites across Europe, Atmos. Environ., 44(10), 1308–1320, doi:10.1016/J.ATMOSENV.2009.12.011, 2010.

Querol, X., Tobías, A., Pérez, N., Karanasiou, A., Amato, F., Stafoggia, M., Pérez García-Pando, C., Ginoux, P., Forastiere, F., Gumy, S., Mudu, P. and Alastuey, A.: Monitoring the impact of desert dust outbreaks for air quality for health studies, Environ. Int., 130, 104867, doi:10.1016/J.ENVINT.2019.05.061, 2019a.

Querol, X., Tobías, A., Pérez, N., Karanasiou, A., Amato, F., Stafoggia, M., Pérez García-Pando, C., Ginoux, P., Forastiere, F., Gumy, S., Mudu, P. and Alastuey, A.: Monitoring the

impact of desert dust outbreaks for air quality for health studies, Environ. Int., 130, 104867, doi:10.1016/J.ENVINT.2019.05.061, 2019b.

Querry, M. R., Osborne, G., Lies, K., Jordon, R. and Coveney, R. M.: Complex refractive index of limestone in the visible and infrared, Appl. Opt. Vol. 17, Issue 3, pp. 353-356, 17(3), 353–356, doi:10.1364/AO.17.000353, 1978.

Rajendran, S. and Nasir, S.: ASTER capability in mapping of mineral resources of arid region: A review on mapping of mineral resources of the Sultanate of Oman, Ore Geol. Rev., 108, 33–53, doi:10.1016/J.OREGEOREV.2018.04.014, 2019.

Reed, B. E., Peters, D. M., McPheat, R., Smith, A. J. A. and Grainger, R. G.: Mass extinction spectra and size distribution measurements of quartz and amorphous silica aerosol at 0.33–19 μm compared to modelled extinction using Mie, CDE, and T-matrix theories, J. Quant. Spectrosc. Radiat. Transf., 199, 52–65, doi:10.1016/J.JQSRT.2017.05.011, 2017.

Reig, F. B., Adelantado, J. V. G. and Moya Moreno, M. C. M.: FTIR quantitative analysis of calcium carbonate (calcite) and silica (quartz) mixtures using the constant ratio method. Application to geological samples, Talanta, 58(4), 811–821, doi:10.1016/S0039-9140(02)00372-7, 2002.

Romanias, M. N., Zeineddine, M. N., Gaudion, V., Lun, X., Thevenet, F. and Riffault, V.: Heterogeneous Interaction of Isopropanol with Natural Gobi Dust, Environ. Sci. Technol., 50(21), 11714–11722, doi:10.1021/ACS.EST.6B03708, 2016.

Ryder, C. L., Highwood, E. J., Walser, A., Seibert, P., Philipp, A. and Weinzierl, B.: Coarse and giant particles are ubiquitous in Saharan dust export regions and are radiatively significant over the Sahara, Atmos. Chem. Phys., 19(24), 15353–15376, doi:10.5194/ACP-19-15353-2019, 2019.

Safriel, U. N.: The assessment of global trends in land degradation, in Climate and Land Degradation, edited by M. V. K. Sivakumar and N. Ndiang'ui, pp. 1–38, Springer, Berlin, Heidelberg., 2007.

Sasaki, S.: Determination of complex refractive index using prism composed of absorbing medium, Results Opt., 8, 100260, doi:10.1016/J.RIO.2022.100260, 2022.

Schlatter, T. W.: Vertical Structure of the Atmosphere, Encycl. Aerosp. Eng., doi:10.1002/9780470686652.EAE582, 2010.

Seinfeld, J. H. and Pandis, S. N.: Atmospheric chemistry and physics: from air pollution to climate change., Atmos. Chem. Phys. from air Pollut. to Clim. Chang., 2169–2176, 2006.

Serio, C., Masiello, G., Mastro, P. and Tobin, D. C.: Characterization of the observational covariance matrix of hyper-spectral infrared satellite sensors directly from measured earth views, Sensors (Switzerland), 20(5), doi:10.3390/S20051492, 2020.

Shao, L. Y., Li, W. J., Yang, S. S., Shi, Z. B. and Lü, S. L.: Mineralogical characteristics of airborne particles collected in Beijing during a severe Asian dust storm period in spring 2002, Sci. China Ser. D Earth Sci. 2007 506, 50(6), 953–959, doi:10.1007/S11430-007-0035-7, 2007.

Shao, Y., Ishizuka, M., Mikami, M. and Leys, J. F.: Parameterization of size-resolved dust emission and validation with measurements, J. Geophys. Res, 116, 8203, doi:10.1029/2010JD014527, 2011.

She, L., Xue, Y., Guang, J., Che, Y., Fan, C., Li, Y. and Xie, Y.: Towards a comprehensive view of dust events from multiple satellite and ground measurements: Exemplified by the May 2017 East Asian dust storm, Nat. Hazards Earth Syst. Sci., 18(12), 3187–3201, doi:10.5194/nhess-18-3187-2018, 2018.

Shen, Z., Caquineau, S., Cao, J., Zhang, X., Han, Y., Gaudichet, A. and Gomes, L.: Mineralogical characteristics of soil dust from source regions in northern China, Particuology, 7(6), 507–512, doi:10.1016/J.PARTIC.2009.10.001, 2009.

Silvester, P. P. and Ferrari, R. L.: Finite Elements for Electrical Engineers, Finite Elem. Electr. Eng., doi:10.1017/CBO9781139170611, 1996.

Simms, J. E., Berney, I. E. S., Harrelson, D. W., Corcoran, M. K. and Castellane, R. M.: Analysis of Long Wave Infrared (LWIR) Soil Data to Predict Reflectance Response. [online] Available from: https://apps.dtic.mil/sti/citations/ADA508400 (Accessed 16 December 2021), 2009.

Sokolik, I. N. and Toon, O. B.: Incorporation of mineralogical composition into models of the radiative properties of mineral aerosol from UV to IR wavelengths, J. Geophys. Res. Atmos., 104, 9423–9444, 1999.

Spitzer, W. G. and Kleinman, D. A.: Infrared Lattice Bands of Quartz, Phys. Rev., 121(5), 1324, doi:10.1103/PhysRev.121.1324, 1961.

Torres, O., Tanskanen, A., Veihelmann, B., Ahn, C., Braak, R., Bhartia, P. K., Veefkind, P. and Levelt, P.: Aerosols and surface UV products from Ozone Monitoring Instrument observations: An overview, J. Geophys. Res. Atmos., 112(D24), 24–47, doi:10.1029/2007JD008809, 2007.

Usher, C. R., Michel, A. E. and Grassian, V. H.: Reactions on Mineral Dust, , doi:10.1021/cr020657y, 2003.

Vandenbussche, S., Kochenova, S., Vandaele, A. C., Kumps, N. and De Mazière, M.: Retrieval of desert dust aerosol vertical profiles from IASI measurements in the TIR atmospheric window, Atmos. Meas. Tech., 6(10), 2577–2591, doi:10.5194/AMT-6-2577-2013, 2013.

Wainker, D. M., Tackett, J. L., Getzewich, B. J., Liu, Z., Vaughan, M. A. and Rogers, R. R.: The global 3-D distribution of tropospheric aerosols as characterized by CALIOP, Atmos. Chem. Phys., 13(6), 3345–3361, doi:10.5194/ACP-13-3345-2013, 2013.

Wallace, J. M. and Hobbs, P. V.: Atmospheric Science: An Introductory Survey: Second Edition, Elsevier Inc., 2006.

Wang, F., Yang, T., Wang, Z., Cao, J., Liu, B., Liu, J., Chen, S., Liu, S., Jia, B., Chan, L. and Zhang, F.: A Comparison of the Different Stages of Dust Events over Beijing in March 2021: The Effects of the Vertical Structure on Near-Surface Particle Concentration, , 13, 3580,

doi:10.3390/rs13183580, 2021.

Wang, X.: Interactions of ozone and acetic acid with natural Gobi dust, Sorbonne Université, 10 September. [online] Available from: https://tel.archives-ouvertes.fr/tel-03004801 (Accessed 16 December 2021), 2019.

Wang, Z., Uno, I., Yumimoto, K., Pan, X., Chen, X., Li, J., Wang, Z., Shimizu, A. and Sugimoto, N.: Dust Heterogeneous Reactions during Long-Range Transport of a Severe Dust Storm in May 2017 over East Asia, Atmosphere (Basel)., 10(11), doi:10.3390/atmos10110680, 2019.

Washington, R. and Todd, M. C.: Atmospheric controls on mineral dust emission from the Bodélé Depression, Chad: The role of the low level jet, Geophys. Res. Lett., 32(17), 1–5, doi:10.1029/2005GL023597, 2005.

Winta, C. J., Gewinner, S., Schöllkopf, W., Wolf, M. and Paarmann, A.: Second-harmonic phonon spectroscopy of α -quartz, Phys. Rev. B, 97(9), 094108, doi:10.1103/PhysRevB.97.094108, 2018.

Wu, J., Kurosaki, Y., Shinoda, M. and Kai, K.: Regional Characteristics of Recent Dust Occurrence and Its Controlling Factors in East Asia, SOLA, 12, 187–191, doi:10.2151/SOLA.2016-038, 2016.

Xie, Y., Liu, Z., Wen, T., Huang, X., Liu, J., Tang, G., Yang, Y., Li, X., Shen, R., Hu, B. and Wang, Y.: Characteristics of chemical composition and seasonal variations of PM2.5 in Shijiazhuang, China: Impact of primary emissions and secondary formation, Sci. Total Environ., 677, 215–229, doi:10.1016/J.SCITOTENV.2019.04.300, 2019.

Xuan, J. and Sokolik, I. N.: Characterization of sources and emission rates of mineral dust in Northern China, Atmos. Environ., 36(31), 4863–4876, doi:10.1016/S1352-2310(02)00585-X, 2002.

Young Jeong, G.: Mineralogy and geochemistry of Asian dust: Dependence on migration path, fractionation, and reactions with polluted air, Atmos. Chem. Phys., 20(12), 7411–7428, doi:10.5194/acp-20-7411-2020, 2020.

Zhou, D., Larar, A. and Liu, X.: Update on IASI Emissivity Atlas, in 19th International TOVS Study Conference (ITSC-19) Jeju Island, South Korea., 2014a.

Zhou, D. K., Smith, W. L., Larar, A. M., Liu, X., Taylor, J. P., Schlüssel, P., Strow, L. L. and Mango, S. A.: All weather IASI single field-of-view retrievals: Case study - Validation with JAIVEx data, Atmos. Chem. Phys., 9(6), 2241–2255, doi:10.5194/ACP-9-2241-2009, 2009.

Zhou, D. K., Larar, A. M., Liu, X., Smith, W. L., Strow, L. L., Yang, P., Schlüssel, P. and Calbet, X.: Global land surface emissivity retrieved from satellite ultraspectral IR measurements, IEEE Trans. Geosci. Remote Sens., 49(4), 1277–1290, doi:10.1109/TGRS.2010.2051036, 2011.

Zhou, D. K., Larar, A. M. and Liu, X.: Monitoring surface climate with its emissivity derived from satellite measurements, https://doi-org.ressources-electroniques.univ-lille.fr/10.1117/12.974215, 8524, 55–61, doi:10.1117/12.974215, 2012.

Zhou, D. K., Larar, A. M. and Liu, X.: UPDATE ON IASI EMISSIVITY ATLAS, in 19th International TOVS Study Conference (ITSC-19) Jeju Island, South Korea., 2014b.

ABSTRACT

East Asia is the second largest source of mineral-type aerosols in the world after the Sahara. These can modify the Earth's radiative balance due to their properties of absorption and diffusion of atmospheric radiation. Therefore, precise information on the physico-chemical properties of desert dust is essential to understand and better quantify their impact on the atmosphere. In this context, we aim to test the potential of a new methodological approach combining laboratory measurements and satellite remote sensing for better characterization of aerosols from the desert and semi-arid surfaces. The application concerns studying desert storm events in East Asia from the IASI spaceborn instrument.

One of the major difficulties of this work comes from the fact that mineral dust in East Asia is emitted above the continental surface in the lower troposphere, which poses constraints linked first to a low detection sensitivity due to a lack of thermal contrast and second due to the high influence and variability of the Land Surface Emissivity (LSE). Thus, the first part focused on improving the consideration of LSE by developing a new methodology from a set of average monthly emissivity dataset. Then, experimental extinction coefficients of pure minerals were linearly combined to reproduce a spectrum of Gobi dust, which made it possible to obtain the mineralogical mass fractions. In addition, from the IASI radiances, an optical thickness of Gobi dust was calculated, displaying characteristics identical to those measured in the laboratory. The linear combination of pure mineral spectra was then applied to IASI optical thickness, providing mineralogical mass fractions. Finally, the entire methodology was applied to two dust events during two different seasons and years: May 2017 and March 2021. The method made it possible to obtain the first spatial and temporal distributions of the chemical composition of desert aerosols. The average mass fractions obtained for particles from the Gobi Desert, Taklamakan Desert, and Horqin Sandy Land are close to mass fractions from the literature. In addition, these results on the chemical composition made it possible to link aerosols' spatial variability to dust emission sources, confirmed using a backward trajectory model. In addition, comparing two IASI instruments on MetOp A and B showed good consistency, allowing us to consider the method's applicability to different MetOp platforms having the same instrument type. The results present an important advance in improving the characterization of desert aerosols by space remote sensing, in particular concerning the analysis of the chemical composition.

Abstract

L'Asie de l'Est est la deuxième source d'aérosols de type minérale au monde après le Sahara. Celles-ci peuvent modifier le bilan radiatif de la Terre de par leurs propriétés d'absorption et de diffusion du rayonnement atmosphérique. Par conséquent, une information précise des propriétés physico-chimiques des poussières désertiques est essentielle pour comprendre et mieux quantifier leur impact sur l'atmosphère.

Dans ce contexte, l'objectif de cette thèse est de tester le potentiel d'une nouvelle approche méthodologique combinant mesures de laboratoire et de télédétection satellitaire pour une meilleure caractérisation des aérosols issus des surfaces désertiques et semi-arides. L'application de celle-ci porte sur l'étude d'évènements de tempêtes désertiques dans l'Est Asiatique à partir de l'instrument spatial IASI.

Une des difficultés majeures de ce travail vient du fait que la poussière minérale émise dans cette région réside majoritairement au-dessus de la surface continentale et dans la basse troposphère, ce qui pose des contraintes liées d'une part à une faible sensibilité par manque de contraste thermique et d'autre part dues à la grande influence et l'importante variabilité de l'émissivité de la surface terrestre (EST). Ainsi, la première partie de ce travail s'est attachée à améliorer la prise en compte de l'EST en développant une nouvelle méthodologie à partir d'un ensemble de données d'émissivité mensuelle moyenne.

Ensuite, des coefficients d'extinction expérimentaux des minéraux purs ont été combinés linéairement pour reproduire un spectre de poussières de Gobi, ce qui a permis d'obtenir les fractions massiques minéralogique. De plus, à partir des luminances IASI, une épaisseur optique de poussières de Gobi a été calculée, affichant des caractéristiques identiques à celle mesurée en laboratoire. La combinaison linéaire des spectres de minéraux purs a ensuite été appliquée à l'épaisseur optique IASI, fournissant des fractions massiques minéralogiques.

Enfin, l'ensemble de la méthode a été appliqué à deux événements de poussières au cours de deux saisons et années différentes : Mai 2017 et Mars 2021. Ce qui a permis d'obtenir les premières distributions spatiales et temporelles de la composition chimique d'aérosols désertiques. Les fractions massiques moyennes obtenues pour les particules provenant du désert de Gobi, du désert de Taklamakan et de Horqin Sandy Land sont proches des fractions massiques de la littérature. De plus, ces résultats sur la composition chimique ont permis de lier la variabilité spatiale des aérosols aux sources d'émission de poussières, confortée à l'aide d'un modèle de rétro-trajectoires. De plus, une comparaison entre deux instruments IASI sur Metop A et B a montré une bonne cohérence, permettant d'envisager l'applicabilité de la méthode à différentes plates-formes Metop, voir à d'autres instruments du même type. Les résultats exposés dans ce manuscrit représentent une avancée importante quant à l'amélioration de la caractérisation des aérosols désertiques par télédétection spatiale, notamment concernant l'analyse de la composition chimique.